Viral proteins as targets for antibody therapeutics and molecular detection agents

Ha Van Dang

A dissertation

submitted in partial fulfillment of the

requirements for the degree of

Doctor of Philosophy

University of Washington

2021

Reading Committee:

David Veesler, Chair

Alexey Merz

Andrew McGuire

Program Authorized to Offer Degree:

Biochemistry

University of Washington

Abstract

Viral glycoproteins as targets for antibody therapeutics and molecular detection agents

Ha Van Dang

Chair of the Supervisory Committee:
David Veesler, PhD
Biochemistry

The most recent viral pandemic, COVID-19 caused by Severe Acute Respiratory Syndrome Coronavirus 2 (SARS-CoV-2), which has so far resulted in the deaths of 5 million people, is a solemn reminder of the immense burden and challenge viruses can place on the economy and healthcare system and emphasizes the importance of preparedness and surveillance for viral outbreaks. Many human viruses are enveloped with a lipid bilayer and enter host cells by fusing the viral envelope to host membranes. Viral glycoproteins are main components of a virus and play a critical role in the membrane fusion process. They are also in many cases the major antigenic determinants of a virus. Understanding the structures and functions of fusogenic viral glycoproteins enables strategies for countermeasures and surveillance. In this dissertation, I studied

the glycoproteins of two highly pathogenic human viruses, Henipaviruses (HNVs) and SARS-CoV-2 and showed that we can use structural information about the glycoproteins of these viruses in two different but related applications. One application is to understand how monoclonal antibodies and antibody cocktails can inhibit a virus from entering and infecting cells (Chapter 2 & 3). The other application is to design molecules, in this case a DNA aptamer, that specifically recognize a viral glycoprotein and use them for detection of the virus (Chapter 4).

TABLE OF CONTENTS

LIST OF FIGURES

Chapter 1

Chapter 2

Chapter 3

Chapter 4

LIST OF TABLES

Chapter 2

Chapter 3

Chapter 4

LIST OF ABBREVIATIONS

Ab	antibody
BLI	biolayer interferometry
BSL-4	biosafety level 4
CedV	Cedar virus
CoV	coronavirus
CDR	complementary determining region(s)
CH	heavy chain
CL	light chain
cryo-EM	cryoelectron microscopy
DAR-V	Daeryong virus
ELISA	enzyme-linked immunoassay
F protein	fusion protein
Fab	fragment antigen-binding
G protein	glycoprotein
GAK-V	Gamak virus
GhV	Ghanaian virus (also known as Kumasi Virus or KV)
HeV	Hendra virus
HeVv	Hendra virus variant
HNV	Henipavirus
LFA	lateral flow assay
mAb	monoclonal antibody
MojV	Mojiang virus
NiV	Nipah virus
NiV-M	Nipah virus Malaysia strain
NiV-B	Nipah virus Bangladesh strain
nt	nucleotide(s)
NTD	N-terminal domain
PIV	parainfluenza virus
RBD	receptor binding domain
S protein	Spike protein
SA	streptavidin
SARS	severe acute respiratory syndrome
SNAP	SARS-CoV-2 Spike N-terminal domain binding aptamer

ACKNOWLEDGEMENTS

My PhD journey could not have been this enjoyable without mentors, friends and family who provided me with so much support in all possible ways. I am extremely happy to dedicate this section of my thesis to express my gratitude to these individuals.

First and foremost, I have to thank my PhD advisor, David Veesler. Your scientific rigor and discipline are a huge inspiration for me every day. Thank you for the countless hours you patiently taught me Linux command lines. Thank you for your prompt presence whenever I had trouble with the microscope, even if it was midnight on a weekend. Thank you for having my back through various problems, whether it is about science or visa/ immigration or career moves. Thank you for teaching me science and letting me do science, David. I am incredibly honored and proud to have been a member of The Veesler lab!

Next, I would like to thank all my collaborators on various projects throughout my PhD at UW. You all are amazing team players! The Henipavirus project is a long-term and highly collaborative project with scientists from four research institutions and companies. I would like to thank our longest-standing collaborator Christopher Broder and his lab members, including Yee-peng Chan, Linda Yan, Sofia Cheliout Da Silva, and Moushimi Amaya at Uniformed Services University. I would also like to thank Bob Cross, Viktoriya Borisevich, Chad Mire and Thomas Geisbert from UTMB and Galveston National Lab in Texas, Chanakha Navaratnarajah from Mayo Clinic in NYC, and Zachary Bornholdt, Brandyn West and Larry Zeitlin from Mapp Biopharmaceutical. Shoutout to Zhaoqian, a Veesler labmate who is courageous enough to take on some really challenging parts of the Henipavirus project. We have come a long way and I very much enjoyed working and discussing science with you! Besides the Henipavirus project, I have also had the pleasure to work with Robby Divine and the Baker lab on the Antibody Nanocages, and Suzie Pun and her lab members including Lucy Yang, Nataly Kacherovsky and Ian Cardle on the Spike-Aptamer project.

I want to thank past and present Veesler lab members who are part of the reason why I am so excited to get up and go to work every day. Dear Lexi, Andrew, Young, Ale, Zhaoqian, Sam, Max, John, Matt, Amin, Joel, Mary Jane, Anshu, Amin, Kaiti, Ollie, Joost, Cameron, and Alex Xiong, you all are not only my colleagues but also my friends. I love you all for being smart and hardworking scientists and extremely fun and supportive friends. I will miss our lunch get-togethers, late nights and early mornings in labs, random meme sharing, the spontaneous badminton tournament, Howe Street stairs runs, hikes and climbing sessions and many many other things we did together!

I would like to thank all my science mentors. Lexi, thank you for mentoring me during my rotation and throughout my PhD in the Veesler Lab and possibly for another long while! Our paths seem to always cross and I am very grateful for that! Dear Karan and Lila, thanks for having taken me under your wings when I was an undergrad at Mount Holyoke. Claire and Jay, thanks for teaching me cool biochemistry tricks and letting me experience the industry life and fiddle around with the microscopes during my 5-month co-op at Biogen. You two and the whole Biogen BTMS Department made my co-op such an amazing experience despite the extreme Boston weather on top of the COVID-19 pandemic.

I am lucky to have friends anywhere I go, who do many fun things with me, come with me on various adventures and keep me sane through the ups and downs of lab life. Special shoutouts to Celia and Adam. Celia, I am so happy we have been good buddies during our PhD and "baby alpinism" journeys. Adam, it would be impossible for me to list out all the details of how you have been a sturdy pillar of support to me in the past years. Cheers to many more years of friendship and adventures!

Lastly, I would like to thank my family. They have given me with so much support throughout my years in the US. Even though I have been living in a foreign country half the earth away from them, I feel like they are always next to me. I am incredibly grateful to mẹ Thuỷ, ba Long, ông bà ngoại and ông bà nội, cô Cẩm and cậu Huy, for your unfazed belief in me. I am so lucky to have been raised by you all - the people who ingrained in my brain the values of integrity and hard-work and who formed the basis for whom I have become today.

Chapter 1. INTRODUCTION

1.1 WHAT ARE VIRUSES?

Although the question of whether viruses are living things or not is debatable, they comprise the simplest, yet the most diverse domain of organisms on Earth. Ranging somewhere between 20 nm - 400 nm in diameter, 1/200 of a human hair's breadth, viruses are tiny particles that can only be observed with powerful electron microscopes. Each viral particle, or "virion", contains a virus' genetic information in the form of nucleic acid, DNA or RNA, single- or double-stranded, encased by a protective layer of viral proteins called "capsid" and/or a lipid membrane called "envelope". Viruses are usually depicted as spherical, but in reality, they adopt other different shapes such as polygons, rods and filaments.

Viruses are obligate parasites, meaning that they cannot replicate on their own. They depend on host cells to propagate by "hijacking" the host resources such as replication machineries. It is worth pointing out that using words like "parasites" and "hijack" to describe viruses may inadvertently give them a negative connotation. Some viruses benefit their hosts, such in the case of Herpesviruses that provide host mice with protection against bacterial infections (Barton et al., 2007). For a comprehensive review of such "good viruses", refer to (Roossinck, 2011). It is also worth noting that viruses do not only infect humans, or even only just mammals, for that matter! They also infect bacteria - another class of tiny organisms that humans sometimes confuse with viruses.

It appears the sole purpose in life of viruses is to make more of themselves and unfortunately, in most cases, they do so at the cost of causing burdens to their hosts. In humans, symptoms of viral infections can range from mild ones such as sneezing and headaches like those caused by the flu or common cold viruses, to dire ones like vomiting, diarrhea, severe internal bleeding and even death such as in the case of Ebola virus diseases. Human history has witnessed hundreds of viral outbreaks with unimaginable tolls. The most recent global pandemic of SARS-CoV-2, which has caused 5 million deaths so far, is a reminder of how powerful these tiny but mighty creatures are and why it is critical to continuously study them while keeping close surveillance.

1.2 WHY SHOULD WE STUDY THE STRUCTURES AND FUNCTIONS OF VIRAL GLYCOPROTEINS?

As aforementioned, some viruses harbor envelopes made up of lipids. This layer of fatty molecules that encapsulates and protects the viral genetic materials are “studded” with proteins. These proteins are most often time glycosylated, i.e: have sugar molecules attached on the surface and are therefore called “glycoproteins”. Due to their critical functions in the virus life cycle as well as the fact that they are exposed on the virus surface, these glycoproteins are the basis for various applications including viral detection and diagnostics, as well as therapeutics and vaccines.

1.2.1 *Viral glycoproteins are attractive vaccine and therapeutics targets*

In enveloped viruses, viral entry and infection initiation require the fusion of the virus' membrane to the host cell membrane. The viral glycoproteins play a critical role in host cell recognition and catalyze the membrane fusion event. Blocking the activities of these glycoproteins are likely to inhibit viral infection. Viral glycoproteins are thus attractive targets for antiviral therapeutics and form the basis for vaccine design and development. For example, on the vaccine side, the Spike (S) protein of SARS-CoV-2 is the basis for the mRNA vaccines developed by Moderna and Pfizer/BioNTech and the viral-vector-based vaccines by J&J and AstraZeneca. These vaccines produce immune responses, including antibodies that will recognize and block the function of the viral S protein, preventing SARS-CoV-2 from entering and replicating in the body upon exposure to infectious SARS-CoV-2 (Baden et al., 2021; Jackson et al., 2020). On the therapeutics side, recombinant monoclonal antibodies (mAbs) and mAb cocktails that block the function of the SARS-CoV-2 S protein are used as treatments in CoVID-19 patients such as bamlanivimab/ etesevimab combination marketed by Eli Lilly (Dougan et al., 2021), asirivimab/ imdevimab by Regeneron (Weinreich et al., 2021), and single mAb sotrovimab by Vir Biotechnology and GlaxoSmithKline (Cathcart et al., 2021) .

1.2.2 *Viral glycoproteins are used in viral detection*

Decorating the virus surface, viral glycoproteins are functionally useful to the viruses during host cell recognition and entry, but they also provide a blueprint for diagnostics and detection. When a person is infected with a certain virus, their immune system will most likely produce antibodies that recognize specific components of the virus, including the viral glycoproteins. Many serology tests use a recombinantly produced version of the viral glycoproteins to test for the presence of such antibodies in a human patient's serum. For example, the LabCorp COVID-19 Serology test detects antibodies against the S protein of SARS-CoV-2 (Alfego et al., 2021).

1.3 NIPAH VIRUS AND SARS-COV-2 FUSION GLYCOPROTEINS

The bulk of my thesis work focuses on studying the Fusion (F) glycoprotein of Nipah virus (NiV) and the Spike (S) glycoprotein of SARS-CoV-2, albeit from different perspectives. In **Chapter 2** and **Chapter 3** of this dissertation, I presented my works on monoclonal antibodies and antibody cocktails that inhibit the function of the NiV F protein. These antibodies are promising therapeutic molecules for Henipavirus infections. In **Chapter 4**, I discussed my work on DNA molecules (i.e: aptamers) that specifically recognize the SARS-CoV-2 S protein and how we used these molecules as a detection agent for SARS-CoV-2.

Although NiV and SARS-CoV-2 are genetically distal, both viruses have glycoproteins that catalyze the membrane fusion event: F(usion) in NiV and S(pike) in SARS-CoV-2. The NiV F and SARS-CoV-2 S are both classified as Class I viral fusion proteins as they have similar structural elements. Here, I will discuss the available structural data on NiV F and SARS-CoV-2 S proteins, which are critical to my thesis works presented in later chapters.

1.3.1 *Class I viral fusion glycoproteins*

Fusion proteins play a critical role in infection by enveloped viruses. These proteins induce the fusion of the viral envelope with the host cell membrane, allowing for viral entry. There are three classes of viral fusion proteins classified based on structures: class I (notable example: influenza hemagglutinin (HA) protein), class II (notable example: flavivirus E protein) and class III (notable example: vesicular stomatitis virus G protein). I am going to discuss class I fusion proteins only, which are the most relevant to the proteins I studied and presented in this dissertation. For comprehensive reviews on all three viral fusion protein classes, refer to (Harrison, 2015; Felix A. Rey & Lok, 2018).

For all three classes of viral fusion proteins, the currently accepted model in the field postulates that a viral fusion protein exists in a metastable prefusion conformation on the viral surface and some triggering factors (low pH, interaction with host cell factors, etc.) induces a conformational transition into the more stable postfusion conformation. This conformational change is coupled with a release of energy to overcome the repulsive force of bringing two membranes together, thereby catalyzing the membrane fusion process.

Class I fusion proteins are homotrimeric transmembrane proteins in both the prefusion and postfusion conformations. The amino acid sequence of each protomer of the trimer contains two signature heptad repeat (HR) regions termed HRA (or HR1) and HRB (or HR2). The latter is towards the C-terminus of the protein. In the prefusion conformation, the HRA region has a compact fold. A hydrophobic sequence, termed “fusion peptide”, is at or near the N-terminal end of the HRA helix. A proteolytic maturation step carried out by a specific host protease results in two subunits, N-terminal subunit called F2 and C-terminal subunit F1, exposing the fusion peptide at the N-terminus of F1. F1 and F2 are in many cases linked by disulfide bonds. The postfusion conformation of class I viral fusion protein is characterized by a six-helix bundle (6HB) formed by the three HRAs and three HRBs running antiparallel. Many of the early pioneering works on the structures of class I fusion proteins were based on the influenza HA protein. The crystal structures of the influenza HA protein in the prefusion and postfusion conformation shed light on the aforementioned core structural elements of class I fusion proteins (Wilson et al. 1981; Bullough et al. 1994). Some other representative class I fusion proteins include the HIV gp120/gp41 protein complex, respiratory syncytial virus F protein, and the Spike proteins of coronaviruses.

For respiratory syncytial virus (RSV), parainfluenza viruses (PIVs) and Henipaviruses (HNVs), the prefusion F proteins elicit a stronger neutralizing antibody response than their postfusion counterparts (Chan et al., 2012; Marcandalli et al., 2019; McLellan, Chen, Joyce, et al., 2013; Stewart-Jones et al., 2018). Therefore, there is a great interest in strategies to stabilize the F proteins in the prefusion conformation to be used as immunogens. These strategies include introducing trimerization domains such as GCNt or foldon, engineered disulfide bonds, cavity filling mutations, and a combination of these mutations (reviewed by (Felix A. Rey & Lok, 2018)).

1.3.2 *Henipavirus Fusion protein*

Nipah virus (NiV), together with Hendra virus (HeV) and Cedar virus (CedV), comprise the Henipavirus (HNV) genus in the Paramyxovirus family of viruses. NiV and HeV infect mammals from at least six different species and cause fatal diseases in most hosts (Drexler et al., 2012; Eaton et al., 2006; Luby & Broder, 2014; Luby & Gurley, 2012). The devastating health consequences and zoonotic potential of NiV and HeV highlight the need to develop more vaccines and therapeutics against these pathogens.

NiV and HeV are enveloped viruses requiring membrane fusion for infection. This process in NiV and HeV, as well as in the Paramyxovirus family in general, is mediated by the concerted actions of two distinct glycoproteins called G and F. G (glycoprotein) recognizes host cell's proteins EphrinB2 and EphrinB3 and F (fusion) catalyzes the membrane fusion reactions (Aguilar & Iorio, 2012; Bossart et al., 2013; B. Lee & Ataman, 2011). Both G and F are critical components to the initiation of viral entry and infection and are targets for vaccine and therapeutics development.

The G protein is a homotetrameric glycoprotein with an N-terminal transmembrane domain that forms a helical stalk bundle, followed by a C-terminal globular head domain.

The head domain of HNV G adopts a classic beta-propeller fold, similarly to other paramyxoviruses hemagglutinin (H)/ neuraminidase (N) proteins such as Measles H protein and hPIV3 HN protein (Lawrence et al. 2004; Bowden et al. 2008; Hashiguchi et al. 2007).

The NiV and HeV F proteins are homotrimeric class I viral fusion proteins. NiV F and HeV F are synthesized as a single amino acid chain precursor F0 and undergo cleavage by the host endosomal cathepsin L into F1 and F2 subunits linked by disulfide bonds. The N-terminus of the F1 subunit harbors the hydrophobic fusion peptide and two heptad repeat regions, one termed HRA that is adjacent to the fusion peptide and the other one, termed HRB, that is proximal to the transmembrane domain (**Figure 1.1 a**).

Structures of NiV F and HeV F in the prefusion conformation have been solved by crystallography, showing a compact “tree-like” overall shape (Wong et al., 2016; Xu et al., 2015). HNV F structure closely resembles the F proteins from parainfluenza virus 5 (PIV5) (Yin et al., 2006), hPIV3 (Stewart-Jones et al., 2018), Measles virus (Hashiguchi et al., 2018) and canine distemper virus (Kalbermatter et al., 2020). The globular head folded into three non-continuous domains (DI - DIII) followed by a trimeric coiled-coil stalk formed by the C-terminal HRB region (**Figure 1.1**). Although there is no structure of NiV or HeV F in the postfusion conformation, we can extrapolate using the postfusion F structures from the related hPIV3 (Yin et al., 2005). Comparison of the prefusion and postfusion structures indicates that DI and DII are rigid bodies while DIII experiences the most extensive conformational changes during the prefusion to postfusion refolding event. In the prefusion conformation, the HRA, which is part of DIII, is a compact mixture of beta sheets and alpha helices (**Figure 1.1 b, d**) while in the postfusion conformation, it completely refolds into a continuous helix, forming the 6-helix bundle with the three HRB's (**Figure 1.1 c, e**).

1.3.3 *SARS-CoV-2 Spike protein*

Decorating the viral surface, the coronavirus (CoV) Spike (S) plays a critical role in promoting viral entry into host cells. This prominent crown-shaped protein is the major target of neutralizing Abs elicited by infection or vaccination.

As a class I viral fusion protein, S exists in prefusion or postfusion conformations. The prefusion conformation S forms the basis for FDA-approved mRNA vaccines from Pfizer/BioNTech and Moderna. In its prefusion state, S harbors two subunits: an N-terminal S1 subunit that is responsible for attachment and receptor recognition and a C-terminal S2 subunit that functions as the fusion machinery. The S1 subunit contains an N-terminal domain (NTD or so-called Domain A), followed by a receptor binding domain (RBD or so-called Domain B). The RBD recognizes its receptor, the angiotensin-converting enzyme 2 (ACE2), on host cell membranes and is the major target of neutralizing Abs. Several mAbs binding to the NTD have also been shown to have neutralizing activities. For a detailed review on anti-CoV-S neutralizing mAbs, refer to (Corti et al., 2021). The S2 subunit drives membrane fusion and harbors characteristic elements of class I fusion proteins including a fusion peptide followed by two heptad repeat regions HR1 and HR2. For a detailed review on CoV S structures, refer to (Tortorici & Veesler, 2019).

1.4 FIGURES & TABLES

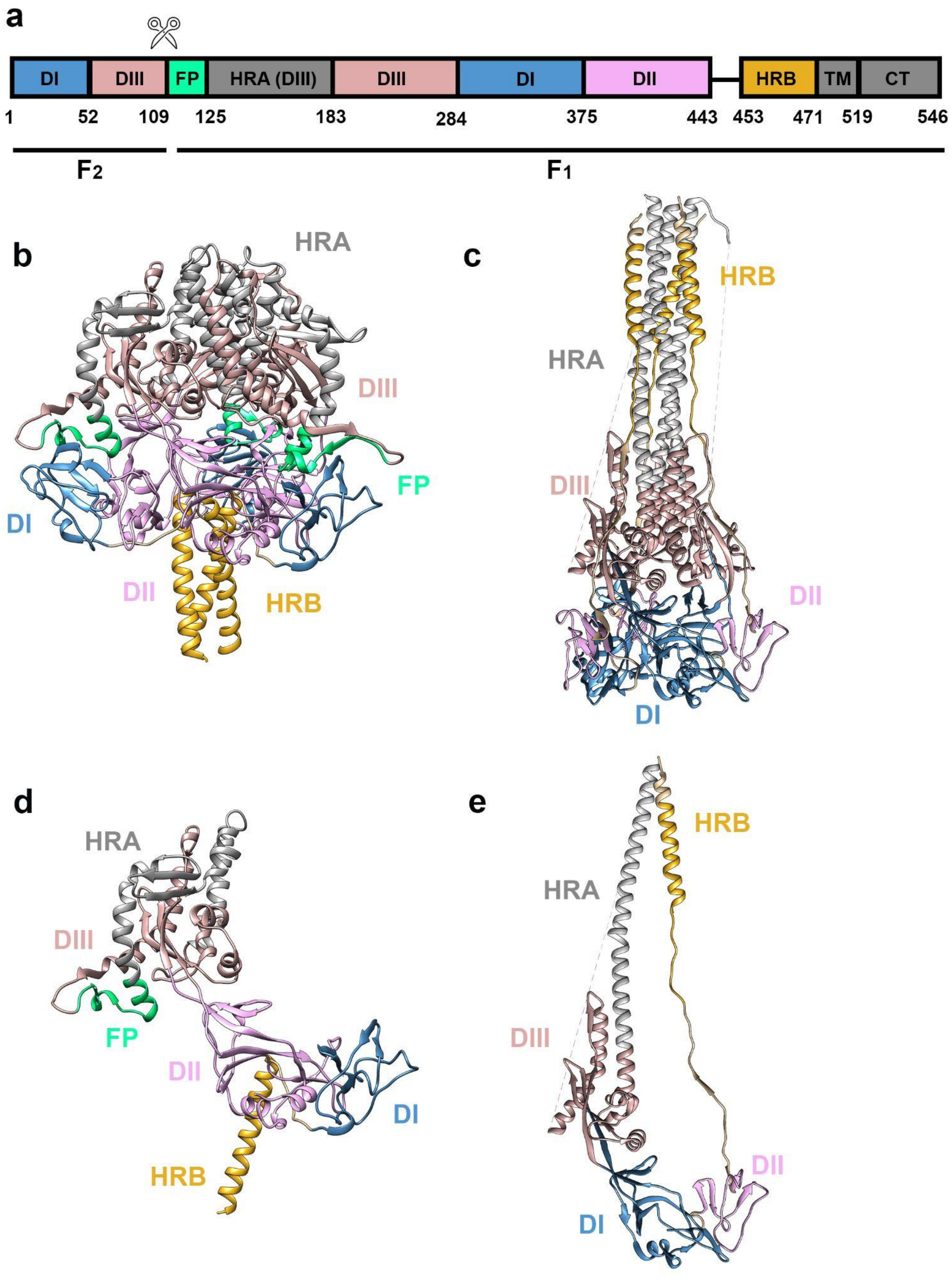
a
DI
DIII
FP
HRA (DIII)
DIII
DI
DII
HRB
TM
CT
1
52
109
125
183
284
375
443
453
471
519
546
F_2
F_1
b
HRA
DIII
FP
DI
DII
HRB
c
HRB
HRA
DIII
DII
DI
d
HRA
DIII
FP
DII
DI
HRB
e
HRB
HRA
DIII
DII
DI

Figure 1.1. Domain organization of NiV and HeV F protein in the prefusion and postfusion conformations. a) Schematic representation of NiV F organization. Domains and notable regions are colored and labeled with corresponding amino acid residues. The scissors symbol denotes the cathepsin-L cleavage site. **b)** Ribbon diagrams of prefusion NiV F trimer (PDB: 5EVM), **c)** postfusion F trimer, **c)** prefusion F protomer and **d)** postfusion F protomer with domains and important regions colored the same as in **a)**. The model for postfusion NiV F is obtained by threading the NiV F sequence on the postfusion human PIV3 F structure (PDB: 1ZTM). FP: fusion peptide, HRA: heptad repeat A, HRB: heptad repeat B, DI-III: Domain I-III, TM: transmembrane domain, CT: C-terminal domain.

Chapter 2. MONOCLONAL ANTIBODIES TARGETING THE HENIPAVIRUS FUSION GLYCOPROTEIN

Adapted from

Dang, Ha V., *et al*. "(Dang et al., 2019)." *Nature structural & molecular biology* 26.10 (2019): 980-987.

Dang, Ha V., *et al*. "(Dang et al., 2021)." *Nature Structural & Molecular Biology* 28.5 (2021): 426-434.

Nipah virus (NiV) and Hendra virus (HeV) are related zoonotic paramyxoviruses, belonging to the Henipavirus (HNV) genus. HNVs have a broad species tropism and can infect animals from at least six mammalian orders (Eaton et al., 2006). Since the first outbreaks of HeV in Australia in 1994 and of NiV in Malaysia in 1998, HeV repeatedly infected horses in Australia with resultant human exposures (Christopher C. Broder et al., 2016) whereas food-borne mediated NiV spillovers have occurred nearly every year in Bangladesh (Luby & Gurley, 2012). Furthermore, NiV outbreaks occurred in the Philippines and in India (Arunkumar et al., 2019). Besides Asia and Oceania, the detection of anti-HNV antibodies in humans and *Pteropus* bats in Africa, a continent for which no documented NiV or HeV outbreaks occurred, further suggested that future HNV zoonotic emergence is likely to happen (Pernet et al., 2014). Although more than two billion people live in regions threatened by potential HNV outbreaks, there are no clinically approved vaccines or specific therapeutics against these pathogens.

As for many other enveloped viruses, the HNV glycoproteins are the only viral antigens displayed on the surface of the virion and are therefore the main targets of virus-neutralizing Abs. Moreover, the presence of neutralizing Abs is a correlate of protection against NiV and HeV in experimentally infected animals (Bossart et al., 2009, 2012; Geisbert et al., 2014). An Ab targeting the G glycoprotein and preventing receptor engagement (Xu et al., 2013; Z. Zhu et al., 2006, 2008), m102.4, was previously used on a compassionate basis to treat individuals with significant HeV or NiV exposure risk in Australia and the USA and successfully completed a Phase I safety trial in Australia which will guide its future use under emergency settings (Playford et al., 2020). Prior to the works presented in this dissertation, there were no well-characterized mAbs targeting HNV F protein. Here we identified, isolated, and characterized three mAbs, designated as 5B3, 1F5 and 12B2, that recognize HNV F protein. We showed that all three mAbs and their humanized counterparts potently neutralize all three known strains of HNVs by stabilizing the F protein in the prefusion conformation, thereby preventing it from performing membrane fusion. High-resolution cryo-EM structures of F in complex with each of these mAbs further support the “molecular stapling” mechanism of neutralization while revealing the atomic details of vulnerable epitopes on the HNV F protein, paving the way for effective vaccine design.

2.1 5B3, 1F5 AND 12B2 BIND THE HNV F PROTEIN AND POTENTLY NEUTRALIZE AUTHENTIC HENDRA AND NIPAH VIRIONS

To explore the humoral immune response against the HNV F glycoprotein, we sequenced the variable regions of the 5B3, 1F5 and 12B2 Abs from hybridomas isolated from mice immunized with a prefusion stabilized NiV F ectodomain trimer (Chan et al., 2012). We used biolayer interferometry (BLI) to characterize binding of the 5B3, 12B2 and 1F5 Fab fragments to prefusion NiV F or HeV F ectodomain trimers immobilized on the surface of biosensors (**Fig. 2.1**). We determined equilibrium dissociation constants (KD) of 27.7 nM and 5.35 nM for attachment of 12B2 to NiV F or HeV F, respectively. The 5B3 Fab recognizes the HeV F and NiV F proteins with KDs of 4.6nM and 10nM, respectively. For 1F5 recognition of NiV F and HeV F, we obtained respective equilibrium dissociation constants of 1.47 nM and 1.24 nM, indicating this Fab bound more tightly than 12B2 or 5B3 to the two tested HNV F glycoproteins. These data establish that each of the three mAbs cross-react with NiV F and HeV F in their prefusion conformation (**Table S2.1**).

We next humanized 5B3 (h5B3.1), 1F5 (h1F5) and 12B2 (h12B2) and evaluated the neutralization potency and breadth of these mAbs and their humanized versions against authentic NiV-Malaysia (NiV-M), NiV-Bangladesh (NiV-B) and HeV. Mean half-maximal inhibitory concentrations (IC_{50}) were determined using plaque reduction assays to monitor viral neutralization in the presence of increasing Ab concentrations **(Fig. 2.2, Table S2.2).** We found that our Abs broadly inhibited NiV-M, NiV-B and HeV with IC_{50} ranging between 0.2-1.3 μg/mL for 1F5/h1F5 and 0.4-3.6 μg/mL for 12B2/h12B2. Furthermore, the humanized versions of 12B2 and 1F5 retained the neutralization potency and breadth of the parental Abs.

2.2 5B3, 1F5 AND 12B2 NEUTRALIZE NIV AND HEV BY PREVENTING MEMBRANE FUSION

To evaluate the effect of 5B3, 12B2 or 1F5 mAbs on membrane fusion, we used a split luciferase-reporter cell-cell fusion assay with effector and target cells expressing HNV G/F or ephrin B2, respectively (Kondo et al., 2010; Laing et al., 2019). We observed that all 3 mAbs inhibited NiV and HeV F/G-mediated membrane fusion in a concentration-dependent manner and that 1F5 outperformed the other two Abs in this assay (**Fig. 2.3**).

2.3 CRYO-EM STRUCTURES OF HNV F IN COMPLEX WITH 5B3, 1F5 AND 12B2 ANTIBODIES REVEAL VULNERABLE EPITOPES ON HNV F

To elucidate the mechanism of mAb-mediated neutralization of NiV and HeV, we determined a cryo-EM structures of a stabilized NiV F or HeV F ectodomain trimer in complex with the Fab fragment from each of the mAbs.

2.3.1 *Cryo-EM structure of 5B3 Fab in complex with HeV F glycoprotein*

We determined a cryo-EM structure of a FLAG-tagged NiV F ectodomain trimer stabilized by a disulfide mutant (N100C-A119C) and a C-terminal GCNt trimerization domain in complex with the 5B3 antibody Fab fragment at 3.5 Å resolution (**Figure 2.4, Figure S2.1, Table 2.1**). To assist model building, we also crystallized the isolated 5B3 Fab fragment and determined its structure at 1.5 Å resolution using X-ray crystallography **(Table 2.2**). In agreement with the features observed in the cryo-EM map, the local resolution is highest for most of NiV F and the 5B3 variable domains, including the interface between NiV F and 5B3, whereas the Fab constant domains are poorly resolved, due to elbow flexibility between constant and variable domains, and were not modeled. The final model includes NiV F residues 27 to 480 with a chain break between residues 105 and 112. 5B3 binds to a quaternary epitope on domain III of the NiV F globular head, with a stoichiometry of 3 Fabs bound to a F trimer (**Figure 2.4, Figure S2.1 and S2.2**).

The cryo-EM map resolves the four N-linked oligosaccharides present on each NiV F protomer (at positions Asn67, Asn99, Asn414 and Asn464) and reveals 5B3 recognizes a glycan-free epitope on the F surface. We could not detect an oligosaccharide at position Asn64 in the cryo-EM reconstruction **(Figure 2.4)**, in agreement with previous biochemical studies (Aguilar et al., 2006; Carter et al., 2005; Moll Markus et al., 2004). All six CDR loops (and the light chain framework region 2) contribute to the paratope and bury 980Å^2 at the interface with the NiV F epitope, which mostly resides within one protomer **(Figure 2.5 a-b)**. CDRL1 contacts the NiV F heptad-repeat A (HRA) β-hairpin via electrostatic interactions between Gln27$_{5B3}$ and Lys160$_F$, Gln162$_F$ and Thr168$_F$ **(Figure 2.5 a-c, Figure S2.2)**. CDRL1, CDRL3 and CDRH3 bind to the core β-sheet in domain III via contacts with both F2 (residues 53-55) and F1 (residues 282-285) subunits **(Figure 2.5 a-cc).** CDRH2 protrudes at the interface between two NiV F protomers and interacts with a segment C-terminal to the central helix and with the upstream helix of a neighboring protomer **(Figure 2.5 a-c, Figure S2.2).** Comparison with the unliganded NiV F structure reveals 5B3 binding induces a local reorganization (or stabilizes a different conformation) of the HRA β-hairpin (residues 160-170) and of residues 248-252 (**Figure S2.3**).

5B3 relies on an atypical binding mode to NiV F with nearly equal contributions of the heavy (48%) and light (52%) chains to the antibody buried surface area. This in part results from the fact CDRL1 is making a greater contribution to the paratope than the nine residue-long CDRH3 (268 $Å^2$ versus $190Å^2$ of buried surface area, respectively), in contrast with the canonical CDRH3-dominated antibody/antigen interfaces. To confirm these findings, we probed the NiV F binding ability of single-chain (scFv) chimeric constructs in which either the variable heavy or variable light h5B3 chains were replaced with an unrelated chain from a human scFv library. Although h5B3 scFv immunoprecipitated full-length NiV F, none of the scFv chimeras did, in agreement with the equivalent contributions to binding of the heavy and light chains observed in our structure **(Figure 2.5a-b and Figure S2.4a**). The structural data were further validated using site-directed mutagenesis of selected residues participating to the NiV F epitope followed by 5B3-mediated immunoprecipitation to assess residual binding (**Figure S2.4b**). We also used the prefusion F specific 12B2 antibody as well as a cell-cell fusion assay to probe the conformational integrity of the F mutants analyzed (**Figure S2.4b-c**). The NiV F K55A substitution inhibited 5B3 recognition, which is likely explained by the loss of interactions with CDRL1 $\text{Trp32}_{\text{5B3}}$ and CDRL3 $\text{Tyr92}_{\text{5B3}}$ residues, as visualized in our structure. Furthermore, abrogation of 5B3 binding to NiV F L53D or L53S likely resulted from reduction of favorable interactions with CDRL1 $\text{Trp32}_{\text{5B3}}$, CDRL3 $\text{Phe91}_{\text{5B3}}$ and CRH3 $\text{Tyr102}_{\text{5B3}}$. Since the tested mutants bound to the12B2 antibody and retained 40-100% of the wild-type F fusion activity (**Figure S2.4b-c**), we concluded the observed loss of binding largely resulted from specific disruption of interactions with 5B3 without major effects on the overall F structure.

Analysis of the structure rationalizes the observed cross-neutralization of NiV and HeV since 35 out of the 39 NiV F residues buried upon 5B3 binding are strictly conserved. Variable positions are Thr81$_{\text{NiV}}$, Asn84$_{\text{NiV}}$, Thr88$_{\text{NiV}}$ and Arg336$_{\text{NiV}}$ which are conservatively or semi-conservatively substituted to Ser81$_{\text{HeV}}$, Thr84$_{\text{HeV}}$, Ser88$_{\text{HeV}}$ and Lys336$_{\text{HeV}}$, respectively **(Figure 2.5c)**.

Our structural data suggest 5B3 prevents fusogenic conformational changes leading to membrane fusion by locking NiV F in the prefusion state. The antibody recognizes a discontinuous epitope, spanning two neighboring protomers, present only in prefusion F, based on the conformational changes observed in the related parainfluenza virus 3 postfusion F and respiratory syncytial virus post-fusion F structures (McLellan et al., 2011; Swanson et al., 2011; Yin et al., 2005) **(Figure 2.5a-c and Figure 2.6 a-b)**. Furthermore, CDRL1 interactions with the HRA β-hairpin hinders refolding of the latter motif to contribute to the formation of an elongated central helix, observed in the postfusion F state. This antibody-mediated molecular stapling strategy, involving simultaneous interactions with protein segments that are close to each other in prefusion F but far apart in postfusion F **(Figure 2.6 a-b)**, is conceptually equivalent to the disulfide stapling approach implemented for stabilizing the prefusion conformation of measles virus F (J. K. Lee et al., 2007), RSV F (McLellan, Chen, Joyce, et al., 2013), HeV F (Wong et al., 2016) and PIV F (Stewart-Jones et al., 2018) glycoproteins. Lastly, we predict unfavorable steric clashes would occur with a 5B3 antibody bound to a neighboring protomer upon F refolding.

To validate the hypothesis that 5B3 locks NiV F in the prefusion conformation, we used an *in vitro* F triggering assay entailing (i) cleavage of the wild-type NiV F_0 ectodomain trimer with trypsin, under limited-proteolysis conditions, to recapitulate the *in vivo* cathepsin L-mediated production of F_1 and F_2 (Pager et al., 2006; Pager & Dutch, 2005)and (ii) incubation at 50˚C to promote refolding of the trypsin-cleaved prefusion F trimer to the postfusion conformation (Chan et al., 2012; Connolly et al., 2006). We previously showed peptides derived from the heptad-repeat B (HRB) sequence of NiV F or HeV F prevent completion of F refolding and are potent inhibitors of fusion and live virus infection (Bossart et al., 2002, 2005). Furthermore, when the triggering assay was carried out in the presence of a biotinylated HRB-peptide, a conformational intermediate of the fusion reaction was captured and could be used as a reporter of F activation. Using this approach, we demonstrate here that addition of 5B3 or h5B3.1 during the triggering assay blocked fusogenic conformational changes in a concentration-dependent manner, whereas a non-neutralizing control antibody (13G5), specific for postfusion F, did not (**Figure 2.6 c-d**). Subsequent antibody affinity purification (protein G) of the material not captured by the HRB-peptide showed 5B3 (or h5B3.1) remained bound to F (**Figure 2.6 d**), supporting the hypothesis that 5B3/h5B3.1 trap NiV F in the prefusion conformation. Finally, capture of an F intermediate could be partially rescued by raising the temperature to ≥ 60˚C, indicating that binding of 5B3/h5B3.1 stabilizes NiV F by raising the energy barrier for transitioning to the postfusion state (**Figure 2.6 e**). In summary, the structural and biochemical data presented here show 5B3 /h5B3.1 inhibited fusogenic conformational changes by locking F in the prefusion state and raising the free energy of activation for fusion triggering.

2.3.2 *Cryo-EM structure of 1F5 Fab in complex with HeV F glycoprotein*

We determined a cryo-EM structure of an S-tagged GCNt-stabilized HeV F ectodomain trimer in complex with the 1F5 Fab fragment at 2.8 Å resolution **(Fig. 2.7 a-c, Fig. S2.5 and Table 2.1)**. The map is best resolved for most of HeV F and the Fab variable domains whereas the peripheral Fab constant domains are weakly resolved and were not modeled. The final model includes HeV F residues 26-471 with a chain break at the boundary between the F_2 and F_1 subunits (residues 104-112 were not resolved).

1F5 binds to a glycan-free quaternary epitope on the side of domain III of the HeV F globular head with three Fabs recognizing an F trimer. The six Fab CDRs and FRL3 contribute to burying ~1,000 Å^2 at the interface with F with equal contributions of the 1F5 heavy and light chains (**Fig. 2.7 d**). The 1F5 paratope is dominated by aromatic amino acid residues, which contact F through hydrogen bonding and shape complementarity, including heavy chain Tyr33$_{1F5}$, Tyr34$_{1F5}$, Tyr51$_{1F5}$, Tyr54$_{1F5}$, Phe99$_{1F5}$, Tyr103$_{1F5}$, Trp104$_{1F5}$ and light chain Tyr31$_{1F5}$, Tyr48$_{1F5}$, Trp90$_{1F5}$, Tyr91$_{1F5}$, Tyr93$_{1F5}$ (**Fig. 2.7 e**). CDRL2 and CDRH3 interact electrostatically with the HeV F HRA β-hairpin through contacts involving the Gln166$_{HeV}$ amide side chain and the CDRL2 Ser55$_{1F5}$ and CDRH3

Tyr108$_{1F5}$ side chain hydroxyl groups as well as through the Lys160$_{HeV}$ amine and CDRL2 Asn52$_{1F5}$ amide side chains. CDRH1-H3 and CDRL1-L3 recognize residues of both the F$_1$ and F$_2$ subunits in the core β-sheet and the region C-terminal of the central helix through electrostatic contacts such as (i) the CDRH2 Thr53$_{1F5}$ hydroxyl and Asn51$_{HeV}$ amide side chains, (iii) the CDRH3 Ser101$_{1F5}$ hydroxyl and the Thr54$_{HeV}$ backbone carbonyl, (iii) the CDRL1 Tyr31$_{1F5}$ hydroxyl and the Arg244$_{HeV}$ backbone carbonyl, and (iv) the CDRL3 Tyr91$_{1F5}$ backbone carbonyl and Tyr93$_{1F5}$ backbone amide with the Glu251$_{HeV}$ backbone amide and side chain carboxylate, respectively. Finally, CDRL1 and FRL3 bridge the interface between two protomers by contacting the upstream helix of a neighboring F protomer (**Fig. 2.7 e**).

Analysis of the 1F5 epitope conservation between NiV F and HeV F shows that 27 out of 29 residues buried upon 1F5 binding are strictly conserved (**Fig. 2.7 f**). Variable positions are Thr74$_{HeV}$ and Ser81$_{HeV}$ which are conservatively substituted to Ser74$_{NiV}$ and Thr81$_{NiV}$, respectively. These two amino acid residue differences are not expected to have a major impact on the epitope/paratope interface, in support of the observations that the 1F5 Fab recognizes both NiV F and HeV F trimers with near-identical affinities **(Fig. 2.7 f, Fig. 2.1 c-d, Table S2.1)**.

Comparisons of the structures of HeV F in complex with 1F5 and of NiV F bound to 5B3 shows that the two neutralizing Abs recognize a very similar region on the F trimer through equal contributions of the heavy and light chains to their paratopes. The two Fabs, however, are rotated ~130˚ relative to each other which results in almost complete inversion of the roles of the heavy and light chains for F recognition (**Fig. 2.7 g**). Due to the different angles of approach between the two Fabs, the HeV/1F5 HRA β-hairpin adopts a conformation more similar to the apo HeV F (Wong et al., 2016) and NiV F (Xu et al., 2015) structures than to the NiV F/5B3 structure (Dang et al., 2019).

2.3.3 *Cryo-EM structure of 12B2 Fab in complex with NiV F glycoprotein*

We determined a cryo-EM structure of an S-tagged GCNt-stabilized NiV F ectodomain trimer in complex with the 12B2 Fab fragment at 2.9 Å resolution **(Fig. 2.8 a-c, Fig. S2.6, Table 2.1)**. The local resolution is highest for most of NiV F and the Fab variable domains whereas the (peripheral) constant domains are less well-resolved and were not modeled in density. The final model includes NiV F residues 27-481 with a chain break at the boundary between the F_2 and F_1 subunits (residues 105-111 were not resolved).

12B2 binds to a previously undescribed quaternary epitope in domain III near the F apex (i.e. distal to the viral membrane) with three Fabs bound to an F trimer. The Fab complementary-determining regions (CDRs) CDRH1-H3, CDRL1-L3, and framework regions (FR) FRL1, FRH1 and FRH3 contribute to burying ~1,400 Å^2 at the F interface via electrostatic interactions and shape complementarity (**Fig. 2.8 d-e**). The paratope is dominated by the 12B2 heavy chain (**Fig. 2.8 d**) that engages two adjacent F protomers whereas the Fab light chain contacts a single protomer. 12B2 simultaneously sits atop the HRA β-hairpin of one F protomer and the HRA/central helix region of the neighboring protomer, contacting both the F_2 and F_1 subunits via involvement of the upstream helix-preceding region of both protomers.

CDRH1-H3 and FRH3 recognize HRA through a constellation of interactions between (i) the CDRH1 $Ser28_{12B2}$ and $Ser153_{NiV}$ side chains, (ii) the CDRH1 $Ser31_{12B2}$ main chain carbonyl and side chain hydroxyl with the $Asn155_{NiV}$ amide side chain and the $Ser153_{NiV}$ backbone carbonyl, respectively (iii) the CDRH2 $Thr53_{12B2}$ and the $Glu156_{NiV}$ side chains, (iv) the backbone carbonyl of CDRH2 $Gly54_{12B2}$ and the backbone amide group of $Lys160_{NiV}$, (iv) the FRH3 $Asn70_{12B2}$ and $Gln162_{NiV}$ side chains, (v) the $Arg71_{12B2}$ backbone carbonyl and side chain guanidinium with the $Gln162_{NiV}$ side chain and $Lys160_{NiV}$ backbone carbonyl, respectively; (vi) the FRH3 $Asn73_{12B2}$ backbone and side chain amides as well as backbone carbonyl with the $Gln162_{NiV}$ backbone carbonyl and amide and $Ser150_{NiV}$ hydroxyl, respectively; and the (vii) CDRH3 $Tyr101_{12B2}$ and $Asn67_{NiV}$ side chains. The HRA β-hairpin adopts a conformation similar to the apo HeV F[16] and NiV F[1738] structures. 12B2 engagement of the neighboring protomer involves hydrogen bonding between the CDRH2 $Ser56_{12B2}$ hydroxyl and $Lys193_{NiV}$ amine side chains as well as the CDRH3 $Tyr101_{12B2}$ backbone carbonyl and $Ser191_{NiV}$ side chain hydroxyl in addition to the CRDL1 $Tyr32_{12B2}$ side chain hydroxyl-mediated contacts with the $Ile187_{NiV}$ and $Ile190_{NiV}$ backbone carbonyl in the HRA/central helix region. Strikingly, 12B2 binding induces a 90° rotation of the $Asn67_{NiV}$ N-linked glycan which is moved out of the way to grant the Fab access to the proteinaceous part of the NiV F epitope (**Fig. 2.8 g**). This structural change is stabilized via multiple electrostatic contacts between the oligosaccharide and the heavy chain Gln1$_{12B2}$, CDRH1, CDRH3 and CDRL2 which contribute 18% of the surface buried by the paratope at the interface with NiV F.

To evaluate the impact of the oligosaccharide at position Asn67 on 12B2 recognition, we generated the S69A NiV F point mutant in which the N-glycosylation sequon at residue 67th is abolished. BLI analysis of 12B2 Fab fragment binding to NiV F S69A glycan mutant revealed a markedly higher affinity compared to wildtype NiV F which was virtually exclusively achieved through a ten-fold on-rate enhancement **(Fig. S2.7, Table S2.1)**. These results therefore indicate that although the N67 glycan dampens antibody recognition, 12B2 overcomes this steric barrier by making favorable interactions with the N67 glycan to bind to the NiV and HeV F trimers.

Analysis of the 12B2 epitope conservation between NiV F and HeV F shows that 32 out of 35 residues buried upon 12B2 binding are strictly conserved, including the oligosaccharide at position Asn67 that directly participates in binding (**Fig. 2.8 f**). The M$_{NiV}$68V$_{HeV}$ substitution is not expected to affect Ab recognition, as both side chains point toward the F core. The Q$_{NiV}$70K$_{HeV}$ substitution might enhance interaction with HeV (putatively through contacts with CDRL1 E27) whereas the K$_{NiV}$189Q$_{HeV}$ substitution would not have a major impact on binding as this side chain is not involved in specific interactions with 12B2. The structural data therefore rationalize the roughly comparable affinities measured for binding of the 12B2 Fab fragment to NiV F and HeV F **(Fig. 2.1 a-d, Table S 2.1)**. These results demonstrate that the epitopes recognized by potent HNV F-targeting Abs can involve oligosaccharides, as has been described for some SARS-

CoV-2 (Pinto et al., 2020; Tortorici et al., 2020), MERS-CoV (Walls, Xiong, et al., 2020), HIV-1 (Borst et al., 2018; Stewart-Jones et al., 2016) and EBOV (West et al., 2018) Abs.

2.4 CHAPTER DISCUSSION

The paramyxovirus and pneumovirus F glycoproteins are key mediators of viral entry promoting fusion of the viral and host membranes through large-scale structural rearrangements (McLellan, Chen, Leung, et al., 2013; McLellan et al., 2011; Swanson et al., 2011; Xu et al., 2015; Yin et al., 2005, 2006). The F conformation presented to the immune system can be a major determinant of the antibody response elicited by these glycoproteins. Previous work showed most of the RSV-neutralizing activity in human serum is conferred by antibodies specifically recognizing prefusion F (Sastre et al., 2005). Structure-based physical stabilization of the RSV F prefusion state via mutations and fusion to another protein (domain) as well as multivalent display on a computationally designed nanoparticle platform correlated with increased elicitation of neutralizing mAbs (Krarup et al., 2015; Marcandalli et al., 2019; McLellan, Chen, Joyce, et al., 2013; McLellan, Chen, Leung, et al., 2013). Prefusion stabilized F also induced greater neutralizing humoral immune responses than postfusion F against parainfluenza viruses in mice and rhesus macaques (Stewart-Jones et al., 2018). However, antibodies present in the sera of mice immunized with human metapneumovirus prefusion or postfusion F ectodomain trimers bound similarly to either protein conformation and equally neutralized virus infectivity, demonstrating that prefusion and postfusion F share most neutralizing epitopes for this virus (Battles et al., 2017). We previously established that fusing a GCNt trimeric motif at the C-terminal end of the NiV F and HeV F ectodomains resulted in the production of prefusion stabilized trimers that could elicit a neutralizing antibody response in mice (Chan et al., 2012). Previous to this work, no HNV F mAb, however, had been characterized at the molecular level. Here we sequenced and humanized the three neutralizing mAbs (5B3, 1F5 and 12B2) and demonstrated their ability to bind both NiV F and HeV F, prevent G/F-mediated membrane fusion, as well as cross-neutralize authentic NiV and HeV. We showed 5B3 and h5B3.1 inhibited membrane fusion by locking F in the prefusion conformation upon binding to a conformational (quaternary) epitope which is reorganized during the fusion reaction. This mechanism of action rationalizes the potent 5B3/h5B3.1-mediated neutralization of NiV and HeV entry into target cells and is reminiscent of D25 inhibition of RSV via binding to and stabilization of prefusion F (McLellan, Chen, Leung, et al., 2013). These findings are also in line with the enhanced properties of RSV and parainfluenza viruses prefusion-stabilized F glycoproteins as candidate vaccine immunogens compared to the corresponding postfusion F (Marcandalli et al., 2019; McLellan, Chen, Joyce, et al., 2013; Stewart-Jones et al., 2018). Accordingly, the previously developed disulfide-stabilized prefusion HeV F (Wong et al., 2016), and the corresponding prefusion NiV F construct engineered here, bear the promise of eliciting stronger neutralizing antibody titers than GCNt-only stabilized F glycoprotein ectodomains, by preventing refolding to the postfusion conformation. Using high-resolution cryo-EM, we show that these neutralizing Abs recognize distinct, yet highly conserved, epitopes on the surface of the NiV F and HeV F glycoproteins, adding to the collection of Abs to be used against these dangerous viruses. 5B3 and 1F5 engage the side of the F trimer whereas 12B2 binds to a novel epitope near the F apex distal to the viral membrane. All three Abs recognize quaternary epitopes (involving interactions with the HRA region) and possibly staple F in the prefusion state (**Fig. 2.6 a-b**, **Fig. S2.8 a-d**) to block viral entry by preventing membrane fusion. However, 5B3, 1F5 and 12B2 are unlikely to cross-react with F proteins from Henipa-related viruses such as CedV, GhV and MojV due to the low level of similarity in the amino acids constituting the epitopes of these mAbs on these F proteins compared to HNV F (**Fig. S 2.8 e**).

To date, m102.4 is the only human mAb that has been used for HNV protection studies in ferrets and African green monkeys (Bossart et al., 2009, 2012; Geisbert et al., 2014). Murine antibodies have limited clinical use due to their short serum half-life, inability to trigger human effector functions and the risk of mounting an anti-mouse antibody response. We successfully engineered a humanized version of 5B3 (termed h5B3.1) which retained comparable breadth and potency to the parental mouse mAb and inhibited F-mediated membrane fusion. Therefore, similarly to the anti-HNV G m102.4 neutralizing mAb, the three anti-HNV-F mAbs we described here could potentially be used for prophylaxis or for post-exposure therapy with individuals exposed to NiV or HeV. Between 2010 and 2017, m102.4 was used on a compassionate basis to treat individuals with significant HeV or NiV exposure risk in Australia, the USA and India (https://www.who.int/blueprint/priority-diseases/key-action/nipah/en/). These individuals have no evidence of infection or known health complications since administration of the mAb. The fact m102.4 was used in humans despite the lack of clinical trials or approval by the FDA (or equivalent agencies) emphasizes the urgent need for developing therapeutics and other counter-measures against highly pathogenic HNVs which have fatality rates of 50-100%. The use of antibody cocktails has been proposed for Ebola virus (Bornholdt et al., 2019; Qiu et al., 2014; Wec et al., 2019) or SARS-CoV (Rockx et al., 2010) and implemented as a commercially available therapeutic for Hepatitis-C virus (XTL-6865, XTL Biopharmaceuticals) to prevent and/or limit the emergence of such mutants as well as enhance neutralization breadth. We suggest a similar strategy, combining h5B3.1, h1f5, h12b2 and m102.4 or other anti-HNV mAbs such as mAb66 (Avanzato et al., 2019), targeting multiple antigenic sites on G and F, could be implemented for treating future NiV and HeV infections in humans.

2.5 MATERIAL & METHODS

2.5.1 *Cell lines*

HEK293F cells (Life Technologies) were grown in 293FreeStyle expression medium (Life Technologies), cultured at 37°C with 8% CO_2 and 150 rpm.

HEK293T/17 is a female human embryonic kidney cell line (ATCC). HEK293T/17 cells (kind gift from Dr. Gerald Quinnan) were cultured at 37˚C with 5% CO2 in flasks with DMEM + 10% FBS + penicillin-streptomycin + 10mM HEPES.

VeroE6 cells (ATCC) were grown in serum-free medium (VP-SFM; ThermoFisher) at 37˚C and 5% CO_2. HeLa-USU and HeLa-ATCC (ATCC) cells (Bonaparte et al., 2005) were maintained in DMEM (Quality Biologicals, Gaithersburg, MD) supplemented with 10% cosmic calf serum (HyClone, Logan, UT), and 2 mM L-glutamine.

HeLa-USU cells, ephrin-B2 and ephrin-B3 negative, (kind gift from Anthony Maurelli, Uniformed Services University and HeLa-CCL2, ephrin-B2 positive (ATCC) have previously undergone cytogenetic analysis.

PgsA-745 (ATCC CRL-2242) cells, a derivative deficient in xylosyltransferase (UDP-D-xylose/serine-1,3-D-xylosyltransferase), referred to as CHO745 in this study, was maintained at 37°C with 5% CO2 in Gibco F-12 Nutrient K (Kaighn's Modification of Ham's F-12) Medium (Thermo Fisher Scientific) supplemented with 10% Fetal Bovine Serum (Thermo Fisher Scientific).

CHO cells do not express B-class ephrins endogenously (Huynh-Do et al., 2002) and CHO745 cells were used to generate a stable cell line expressing ephrin-B2 (CHO745-ephrin-B2) by transfection of an expression plasmid encoding an S-tagged ephrin-B2 ORF (Laing et al., 2019) and selected by hygromycin B resistance. CHO745-ephrin-B2 cells were maintained in the same media as CHO745 supplemented with 800 µg/mL hygromycin B.

2.5.2 *Antibodies and peptides*

The rabbit anti-F polyclonal antibody was produced by Spring Valley Laboratories, Inc., Woodline, MD using the NiV F ectodomain trimer fused to GCNt (Chan et al., 2012) as an immunogen. The HRP-conjugated rabbit anti-S-peptide antibody was purchased from Bethyl Laboratories, Inc., Montgomery, TX. Anti-F murine monoclonal antibodies were produced as previously described (Chan et al., 2012).

The N-terminal biotinylated NiV F HRB peptide (residues 453-488) (Bossart et al., 2005) was synthesized by Global Peptide Services, LLC., CO.

2.5.3 *NiV F and HeV F soluble ectodomain constructs*

The FLAG-tagged NiV F ectodomain construct used for cryo-EM experiment of NiV F/5B3 complex includes a human codon-optimized NiV F ectodomain trimer (amino acid residues 1-494) with a FLAG tag (DYKDDDK) introduced between residues L104-V105 and a C-terminal GCNt motif (a kind gift from Dr. Hector Aguilar-Carreno). This construct was engineered by subcloning into a pBSSK(+) vector and introducing the previously described N100C/A119C substitutions (Wong et al., 2016) by site-directed mutagenesis using a QuikChange kit (Agilent) before subsequent subcloning into a pCAGGs vector for transient expression in FreeStyle 293F cells.

The S-tagged NiV F and HeV F ectodomain constructs include the codon optimized NiV F (isolate UMMC1; GenBank Sequence Accession: AY029767) or HeV F (isolate Horse/Australia/Hendra/1994) ectodomain (residues 1-487) fused to a C-terminal GCNt followed by a factor Xa sequence and an S-tag (KLKETAAAKFERQHMDS) cloned in a pcDNA Hygro (+)-CMV+ vector for transient expression in FreeStyle 293F cells. NiV F S69A ectodomain mutant was generated via site-directed mutagenesis. All mutation-containing constructs were sequence verified. These S-tagged ectodomain proteins were used in cryo-EM experiments of NiVF/12B2 and HeVF/1F5 complexes and in all biolayer interferometry experiments.

2.5.4 *NiV F and HeV F soluble ectodomain expression and purification*

All soluble NiV F and HeV F ectodomain constructs (FLAG-tagged and S-tagged) and the corresponding S69A mutants were produced by transient transfection of FreeStyle 293F cells at a density of 1 x 10^6 cells/mL with the corresponding plasmid using 293-Free transfection reagent (Millipore) and Opti-MEM (Thermo-Fisher) according to the manufacturer's protocol. After 5 days in a humidified shaking incubator and maintained at 37°C and 8% CO_2, the cell supernatant was harvested and clarified of cell debris by centrifugation.

The supernatant of FLAG-tagged NiV F protein was subsequently purified by affinity purification using an anti-FLAG resin (Genscript) and elution with 1 mg/mL FLAG peptide dissolved in 50mM Tris buffer pH 8.0, 150mM NaCl or with S-protein agarose (Millipore Sigma, Novagen). The eluted fraction was buffer-exchanged into 50 mM Tris buffer pH 8.0, 150 mM NaCl using a 30 kDa cutoff centrifugal concentrator (Millipore).

The supernatants containing S-tagged F proteins were subsequently subject to affinity purification using S-protein agarose (Millipore Sigma, Novagen) and elution with

0.2 M citric acid pH 2.0 followed by immediate neutralization with 1.0 M phosphate buffer pH 8.0. The eluted fraction was buffer-exchanged into 50 mM phosphate buffer saline (PBS) pH 7.4, 150 mM NaCl using a 30 kDa cutoff centrifugal concentrator (Millipore).

2.5.5 *mAb cloning and sequencing*

The 5B3 cDNA was amplified from hybridomas using SuperScript III Cells Direct cDNA Synthesis Kit (Invitrogen) with random hexamer and IgG2-specific primers (Debat et al., 2001). PCR amplification of the heavy (VH) and light (VL) chain variable domains was performed using the cDNA as a template and degenerate forward primers for the signal sequence or the conserved framework 1 (FR1) of the VH- and VL-encoding sequences and reverse primers for the FR4 or the 3' end of the CH1- and CL-encoding sequences (Debat et al., 2001; Z. Wang et al., 2000). The PCR products were cloned into pCR-Blunt II-TOPO Vector (Invitrogen) and transformed into One Shot TOP10 Chemically Competent *E. coli* (Invitrogen). Plasmids were extracted from colonies and the cloned PCR products were sequenced using M13 forward and reverse primers.

mAbs 1F5 and 12B2 were sequenced by mass spectrometry. The primary structures of the 12B2 and 1F5 heavy and light chains were determined by liquid chromatography mass spectrometry (LC-MS, Rapid Novor, Inc.). For each mAb, eight in-solution and in-gel digestions were prepared using five different enzymes (Pepsin, Trypsin, Chymotrypsin, Asp N, Lys C). The in-solution digestions for each sample were processed with disulfide reduction, alkylation, and then enzyme digestion. Each digestion contained peptides from both heavy and light immunoglobulin chains. The in-gel digestion reactions were prepared for immunoglobulin chains after gel separation. The sample was processed with disulfide reduction, gel separation, deglycosylation, disulfide reduction a second time, alkylation and then digestion. Digestions were analyzed by LC-MS/MS using Thermo-Fisher Q ExactiveTM, Orbitrap FusionTM mass spectrometers. Peptides were characterized from LC-MS/MS data using de novo peptide sequencing and then assembled into antibody sequences.

2.5.6 *mAb humanization*

To engineer a humanized version of 5B3, a human scFv library was first generated based on FR1 and FR4 sequence similarity with 5B3. We adapted previously described methods and PCR primers employed for generation of naive human scFv library constructed from peripheral blood B cells of several healthy donors (Z. Zhu & Dimitrov, 2009) by using only the VH subfamily III and κ VL subfamily I primers. VH and VL were first amplified separately from the IgM cDNA library. For VH, we used forward and reverse primers probing the FR1 and FR4 of VH III with restriction site *Sfi*I added to the 5' end of the forward primer and $(G_4S)_3$ linker sequence added to the 3' end of the reverse primer. For VL, we used forward and reverse primers probing the FR1 and FR4 of VLκ I with $(G_4S)_3$ linker sequence added to the 5' end of the forward primer and restriction site *Sfi*I added to the 3' end of the reverse primer. The scFv library was assembled by overlapping PCR combining the VH and VL PCR products as template and using the VH III FR1 *Sfi*I forward and VLκ I FR4 *Sfi*I reverse primers. The amplified scFv was then cloned into a pCom3X vector harboring a C-terminal hexa-histidine tag. Colonies from the scFv library were grown and expressed as previously described (Dimitrova et al., 2009). We selected the 12 best expressing clones for DNA sequencing based on Coomassie blue staining and Western blot analysis using an anti-histidine tag antibody. The translated human scFv FR sequences were then aligned against that of 5B3. For humanization of 5B3, conserved human residues from the alignment were identified and replaced into the homologous positions of 5B3 to generate h5B3. To further humanize h5B3, a version named h5B3.1 was generated from h5B3 where one residue on each of the CDR 1 and CDR2 and two residues on CDR3 were mutated into conserved human residues based on the sequences from the human scFv library mentioned above.

Humanization of mAbs 1F5 and 12B2 was performed using Mapp Biopharmaceutical's *in silico* humanization pipeline. For each mAb, mouse constant heavy and light chain domains were exchanged with human sequences. High-resolution homology models were constructed of each variable domain, and a structure-guided resurfacing approach was employed to maintain the murine CDR conformations and antigen binding while reducing deviations from the inferred human germline progenitor sequences. Initial humanization was followed by iterative rounds of structure-guided engineering to eliminate residues that contribute to chemical liability hotspots such as aggregation, glycosylation, enzymatic cleavage.

2.5.7 *mAb expression and purification*

The 5B3 scFv constructs were designed with VH and VL separated by a flexible linker $(G_4S)_3$, codon-optimized, synthesized by Genscript (Piscataway, NJ) and cloned into a promoter-modified pcDNA Hygro (+)-CMV+ vector (Chan et al., 2009) with a immunoglobulin κ chain leader sequence and a C terminal S-peptide tag followed by a hexa-histidine tag.

For 5B3 IgG constructs, the VH and VL were cloned into a pDR12 vector that harbors the κ CL and IgG1 CH fragments as separate ORF with independent promoters (Feng & Dimitrov, 2009).

Transient expression of h5B3.1 IgG1 was carried out by transfecting FreeStyle 293F suspension cells in serum free FreeStyle 293 expression medium (Invitrogen) in shaker flasks at a density of 1 $\times 10^6$ cells/mL using 293fectin transfection reagent (Invitrogen) following the manufacturer's protocol. Production of h5B3.1 IgG1 from stable cell line was carried out by culturing the FreeStyle 293F cells expressing h5B3.1 IgG1 in 70 mL of FreeStyle 293 Expression Medium in 500 mL shaker flasks at a density of 1 $\times 10^6$ cells /mL. The transfected cells or stable cells were allowed to grow for an additional 3-4 days with 50 mL of culture medium added for every subsequent day. Culture supernatants expressing IgG were collected and centrifuged at 4°C for 15 minutes at 5000xg. The supernatant was then filtered through a 0.2 μm low protein binding membrane (Corning, Inc., Lowell, MA) and passed through a HiTrap Protein G HP column (GE Healthcare Biosciences, Pittsburgh, PA) equilibrated in phosphate-buffered saline

(Quality Biologicals, Gaithersburg, MD). The column was washed with 5 column volumes of phosphate-buffered saline. The bound mAb was eluted with 0.1M glycine pH 2 followed by immediate neutralization with 1M Tris pH 8.0, concentrated and buffer-exchanged into phosphate-buffered saline using an Amicon Ultra centrifugal concentrator (Millipore).

Humanized 12B2 and 1F5 IgGs were produced by transient expression in ExpiCHO cells (ThermoFisher Scientific) and purified via Protein A chromatography. For each humanized mAb, cells were pelleted 8 days post transfection by centrifugation for 30 min at 3,000xg and supernatant was collected for purification of soluble IgG. Supernatant was flowed over a 5 mL Protein A agarose column using an Akta Pure (MabSelect SuRe, GE Healthcare Life Sciences). The column was washed with five column volumes of DPBS (Gibco) and then IgG was eluted with IgG Elution Buffer (Pierce). The elution fraction was then neutralized with Tris pH 9.0 to a final pH of 7.5. The neutralized elution fraction for each mAb was then concentrated to 5 mg/mL using a 30 kDa molecular weight cutoff Amicon Ultra spin concentrator (Millipore), then aliquoted and stored at -80°C.

2.5.8 *Generation of Fab fragments from IgGs*

The murine 1F5, 12B2 and 5B3 Fab fragments were obtained by fragmentation of the corresponding mouse IgGs using Pierce Mouse IgG1 Fab and F(ab')2 preparation kits according to the manufacturer’s protocol. The Fab-containing fraction was further purified using a Superdex 75 10/300 gel filtration column equilibrated in a buffer containing 50 mM Tris pH 8.0 and 150 mM NaCl and stored at 4°C.

The h5B3.1 Fab fragment was obtained by fragmentation of h5B3.1 IgG with Lys-C protease (EMD Millipore) and affinity purification using protein A agarose resin (Genscript). Briefly, 1.0 mg IgG was incubated with 0.5 µg Lys-C for 7 hours at 37°C. The reaction was quenched by addition of PMSF to 1 mM final concentration and the sample was purified using a protein A resin. The Fab-containing flow-through was concentrated and further purified using a Superdex 75 10/300 gel filtration column equilibrated in a buffer containing 50 mM Tris pH 8.0 and 150 mM NaCl.

2.5.9 *Biolayer interferometry*

Assays were performed with an Octet Red 96 instrument (ForteBio, Inc.) at 30°C while shaking at 1,000 rpm. All measurements were corrected by subtracting the background signal obtained from biosensors without immobilized HeV F or NiV F. S-peptide tagged HeV F WT, NiV F WT, and NiV F S69A in phosphate buffered saline at pH 7.4 were diluted to 20 µg/mL in 10mM acetate buffer pH 5.0 before immobilization on (NHS-EDC activated) Amine Reactive 2nd Generation (AR2G, ForteBio) biosensors for 300s. Sensors were then quenched in 1M ethanolamine (ForteBio) for 300s and incubated in kinetics buffer (KB: 1X PBS, 0.001% BSA, 0.02% Tween 20 and 0.005% NaN_3 (ForteBio)) for 300s to establish the baseline signal (nm shift).

For kinetics assays, HeV F- or NiV F- or NiV F S69A-loaded AR2G sensors were then immersed into solutions of purified Fab (5B3, 12B2 or 1F5) diluted in KB to desired concentrations. Curve fitting was performed using a 1:1 binding model to determine binding kinetics with the ForteBio data analysis software. Mean k_{on} and k_{off} values were determined with a global fit applied to all data. The experiments were performed twice with independent NiV F, NiV F S69A and HeV F protein preparations yielding identical results and kinetic parameters. The estimated kinetics parameters for each replicate are summarized in **Table S2.1**.

2.5.10 *Crystallization, data collection and processing of the 5B3 Fab*

Crystals were grown in hanging drops set up with a mosquito at 20˚C using 150 nL protein solution and 150 nL mother liquor containing 0.2 M Magnesium chloride, 0.1 M Tris-HCl pH 8.5 and 20% PEG 8000. The diffraction dataset was collected at the ALS beamline 5.0.1 and processed to 1.5 Å resolution using XDS (Kabsch, 2010) and Aimless (Evans & Murshudov, 2013) in space group $C222_1$, with cell dimensions a = 78.1 Å b = 94.9 Å and c = 137.2 Å The structure was solved by molecular replacement using Phaser (McCoy et al., 2007) and the S230 SARS-CoV Fab (Walls, Xiong, et al., 2020) as search model. The coordinates were subsequently improved and completed using Buccaneer (Kevin Cowtan, 2006) and COOT (K. Cowtan et al., 2010) and refined with BUSTER-TNT (Blanc et al., 2004) and REFMAC5 (Vagin et al., 2004). The quality of the final model was analyzed using MolProbity (V. B. Chen et al., 2010). Crystallographic data collection and refinement statistics are summarized in **Table 2**.

2.5.11 *Cryo-EM specimen preparation and data collection*

NiV F/5B3 sample was purified by size-exclusion chromatography prior to vitrification. Purified FLAG-tagged NiV F N100C/A119C ectodomain was combined with an excess molar ratio of 5B3 Fab and incubated on ice for 1 hour before injection on a Superose 6 Increase 10/300 column (GE Healthcare) equilibrated in a buffer containing 50 mM Tris pH 8.0 and 150 mM NaCl. The fractions containing the complex were quality-controlled by negative staining EM, pooled, buffer-exchanged and concentrated.

S-peptide-tagged NiV F was incubated with 12B2 Fab at 1:4 molar excess Fab and S-peptide-tagged HeV F with 1F5 Fab at 1:2 molar excess Fab. Both complexes were incubated overnight at 4°C before vitrification.

3μL of each complex, FLAG-tagged NiV F/5B3 Fab, S-tagged NiV F/12B2 Fab or S-tagged HeV F/1F5, at a concentration of 0.1 mg/mL F was applied onto glow-discharged C-flat, Cu 200 mesh, CF-1.2/1.3 or CF-2/2 (Protochips Inc., U.S.) holey carbon grids covered with a thin layer of continuous home-made carbon and incubated for 20s on grids. Grids were then plunge-frozen in liquid ethane, cooled with liquid nitrogen, using an FEI MK4 Vitrobot with a 2.5s blot time. The chamber was kept at 20°C and 100% humidity during the blotting process.

Data acquisition was carried out with the Leginon data collection software (Suloway et al., 2005) on an FEI Titan Krios electron microscope operated at 300kV and equipped with a Gatan BioQuantum energy filter (slit width of 20 eV) and a Gatan K2 Summit camera. For the NiV F/5B3 dataset, the nominal magnification was 105,000x and the pixel size was 1.37Å.

For the NiV F/12B2 and HeV F/ 1F5 datasets, the nominal magnification was 130,000x and the pixel size was 1.05Å. The dose rate was adjusted to 8 counts/pixel/s and each movie was acquired in counting mode fractionated in 50 frames of 200ms each. A summary of data collection is provided in **Table 2.1**.

2.5.12 *Cryo-EM data processing*

For the NiV F/ 5B3 dataset, movie frame alignment was carried out with motioncor2 (Zheng et al., 2017). Particles were automatically selected using DoG Picker (N. R. Voss et al., 2009) within the Appion interface (Lander et al., 2009). Initial defocus parameters were estimated with GCTF (K. Zhang, 2016). 380,459 particles were picked, extracted and processed with a box size of 256 pixel^2 and preprocessed using Relion 3.0 (Zivanov et al., 2018). Reference-free 2D classification with CryoSPARC was used to select a subset of particles, which were used to generate an initial model using the *Ab-Initio* reconstruction function in CryoSPARC (Punjani et al., 2017). This 3D map was subsequently used as a reference for running 3D classification with C3 symmetry in Relion on the entire dataset. 262,879 particles were selected from the set of all picked particles for 3D refinement using Relion. CTF refinement in Relion 3.0 was used to refine per-particle defocus values and particle images were subjected to the Bayesian polishing procedure in Relion 3.0 (Zivanov et al., 2019) and 3D refinement before performing another round of CTF refinement and 3D refinement. The particles were subsequently subjected to another round of 3D classification in Relion 3.0 without refining angles and shifts. 38,756 particles from the best class (showing a resolved stem) were used for non-uniform refinement in CryoSPARC to obtain the final 3D reconstruction at 3.5 Å resolution. Reported resolutions are based on the gold-standard FSC = 0.143 criterion (Rosenthal & Henderson, 2003; Scheres & Chen, 2012) and Fourier shell correlation curves were corrected for the effects of soft masking by high-resolution noise substitution (S. Chen et al., 2013). Local resolution estimation and filtering was carried out using CryoSPARC.

For both NiV F/12B2 and HeV F/1F5 datasets, movie frame alignment was carried out with motioncor2 (Zheng et al., 2017). Particles were automatically selected using DoG Picker within the Appion interface (N. R. Voss et al., 2009). Initial defocus parameters were estimated with GCTF (K. Zhang, 2016). The picked particles were extracted and processed with a box size of 352 pixel^2 and preprocessed using Relion 3.0 (Zivanov et al., 2018). Reference-free 2D classification with CryoSPARC was used to select a subset of particles, which were used to generate an initial model using the *Ab-Initio* reconstruction with no symmetry function in CryoSPARC (Punjani et al., 2017). This 3D map was subsequently used as a reference for running 3D classification with C3 symmetry in Relion on the entire dataset. A subset of particles were selected from these 3D classes for 3D refinement using Relion. CTF refinement in Relion 3.0 was performed to refine per-particle defocus values and particle images were subjected to the Bayesian polishing procedure in Relion 3.0 (Zivanov et al., 2018) and 3D refinement before performing another round of CTF refinement and 3D refinement. The particles were subsequently subjected to another round of 3D classification in Relion 3.0 without refining angles and shifts. Particles from the best class were used for non-uniform refinement in CryoSPARC (Punjani et al., 2020) to obtain the final 3D reconstruction. Reported resolutions are based on the gold-standard FSC = 0.143 criterion (Rosenthal & Henderson, 2003; Scheres & Chen, 2012) and Fourier shell correlation (FSC) curves were corrected for the effects of soft masking by high-resolution noise substitution (S. Chen et al., 2013). Local resolution estimation and filtering was carried out using CryoSPARC.

2.5.13 *Model building and analysis*

For the NiV F/ 5B3 complex, UCSF Chimera (Goddard et al., 2007) was used to rigid-body fit the crystal structures of the NiV F ectodomain (Xu et al., 2013) and of the 5B3 Fab crystal structure into the cryo-EM density. The model was subsequently rebuilt manually using Coot (K. Cowtan et al., 2010) and refined using Rosetta (Brown et al., 2015; DiMaio et al., 2011, 2015). Glycan refinement relied on a dedicated Rosetta protocol, which uses physically realistic geometries based on prior knowledge of saccharide chemical properties (Frenz et al., 2019; R. Y.-R. Wang et al., 2016) and was aided by using both sharpened and unsharpened maps. Models were analyzed using

MolProbity (V. B. Chen et al., 2010), EMRinger (Barad et al., 2015) and Privateer (Agirre et al., 2015). Figures were generated using UCSF ChimeraX (Goddard et al., 2018).

For the HeV F/ 1F5 and NiV F/ 12B2 complexes, UCSF Chimera (Goddard et al., 2007) was used to rigid-body fit the cryo-EM structures of the NiV F ectodomain (from PDB:6TYS) into NiV F/12B2 cryo-EM density and the prefusion HeV F crystal structure (PDB:5EJB) (Wong et al., 2016) into the HeV F/1F5 cryo-EM density. The crystal structure of 5B3 Fab (PDB:6U1T) (Dang et al., 2019) was rigid-body fit into the density for Fabs in the cryo-EM maps of NiV F/12B2 or HeV F/1F5. The 1F5 and 12B2 Fab fragments were then rebuilt manually with the amino acid sequences obtained from mass spectrometry described above. Each model, NiV F/12B2 and HeV F/1F5, was subsequently rebuilt manually using Coot (K. Cowtan et al., 2010) and refined using Rosetta (DiMaio et al., 2011; Frenz et al., 2019; R. Y.-R. Wang et al., 2016). Glycan refinement relied on a dedicated Rosetta protocol, which uses physically realistic geometries based on prior knowledge of saccharide chemical properties (Frenz et al., 2019) and was aided by using both sharpened and unsharpened maps. Models were analyzed using MolProbity (V. B. Chen et al., 2010), EMRinger (Barad et al., 2015) and Privateer (Agirre et al., 2015). Figures were generated using UCSF ChimeraX (Goddard et al., 2018).

2.5.14 *Fusion inhibition assay with split-luciferase*

The quantitative fusion inhibition assay was based on a dual-split-reporter described previously (Kondo et al., 2010; Laing et al., 2018, 2019). Receptor negative CHO745 cells (7 × 10^5 in a 6-well plate) were transfected with 0.75 µg each of the indicated HNV F and G glycoprotein expression plasmids and 0.5 µg of an expression plasmid for one half of a split-luciferase reporter protein (DSP1–7, a kind gift of Z. Matsuda). GeneJuice reagent (Millipore Sigma) was used for transfections according to manufacturer's instructions. Concurrently, CHO745-ephrin-B2 cells (1 × 10^4 cells in a clear-bottom, black wall 96-well plate) were transfected with 100 ng of the expression plasmid for other half of the split-luciferase reporter protein (DSP8-11). 24 hours post-transfection, Versene (0.48 mM EDTA in PBS) (ThermoFisher Scientific) was used to gently detach the CHO745 cells from the 6-well plate and 2.5 × 10^4 cells were incubated for 15 minutes at room temperature with the indicated mAb dilutions prior to been over-laid on the receptor-expressing CHO745-ephrin-B2 cells in the 96-well plate. Single mAbs (1F5, 5B3, and 12B2) were used at 100, 10, 1 and 0.1 ng/mL. Cocktail mAbs (12B2/1F5 and 12B2/5B3) were used at 50, 5, 0.5, 0.25 and 0.125ng/mL of each mAb. Negative control mAb D40 (HIV-gp41-specific mAb) was tested at 100 and 1ng/uL. EnduRen (Promega; WI, USA) was added as the substrate to the culture medium (DMEM, 10%. FBS) according to the manufacturer's instructions. Reconstitution of luciferase function as a result of content mixing driven by cell-cell fusion between the glycoprotein expressing CHO745 cells and the receptor-bearing CHO745-ephrin-B2 cells was measured using an Infinite M200 Pro microplate reader (Tecan; Switzerland). Each data point is comprised of at least 2 technical repeats. The luciferase signal in the sample where there was no mAb added was used to define “100% fusion” and calculate membrane fusion percentage for each mAb treatment.

2.5.15 *BSL-4 neutralization assays*

For 5B3 and h5B3.1 IgGs, The virus infectivity neutralization concentrations of a control antibody D10 IgG2a anti-HIV gp41 (Bossart & Broder, 2004), 5B3 IgG anti-F and h5B3.1 IgG1 anti-F were determined for NiV and HeV using a plaque reduction assay. Briefly, antibodies were serially diluted fivefold from 150 µg/ml to 1.9 ng/ml and incubated with a target of ~ 100 PFU of NiV-M, NiV-B or HeV for 45 minutes at 37°C. Virus and antibody mixtures were then added to individual wells of 6-well plates of VeroE6 cells. Plates were stained with neutral red 2 days after infection and plaques were counted 24 h after staining. Neutralization potency was calculated based on PFU for each virus in the well without antibody. The experiments were performed in triplicate with independent virus preparations and duplicate readings for each replicate. Mean half-maximal inhibitory concentrations were calculated as previously described (C. C. Broder et al., 1994).

For 1F5, h1F5, 12B2, and h12B2, the virus infectivity neutralization concentrations of a control antibody c13G8 IgG specific to the GP38 protein of Crimean-Congo hemorrhagic fever virus (CCHFV) (Mishra et al., 2020), murine 1F5 IgG, humanized h1F5 IgG, murine 12B2 IgG, and humanized h12B2 IgG were determined for NiV-M, NiV-B and HeV using a plaque reduction assay. Briefly, antibodies were serially diluted fivefold from 100 µg/ml to 6.4 ng/ml and incubated with a target of ~ 100 PFU of NiV-M, NiV-B or HeV for 45 minutes at 37°C. The control mAb c13G8 was tested only at the highest concentration (100µg/mL). Virus and antibody mixtures were then added to individual wells of 6-well plates of VeroE6 cells. Plates were stained with neutral red 2 days after infection and plaques were counted 24 h after staining. Neutralization potency was calculated based on PFU for each virus in the well without antibody. The experiments were performed in duplicate with independent virus preparations and duplicate readings for each replicate. Mean half-maximal inhibitory concentrations (IC50) were calculated as previously described (Ferrara & Temperton, 2018).

2.5.16 *Immunoprecipitation*

To evaluate the binding of NiV F mutants with different antibodies, sub-confluent HEK 293T cells were transfected with untagged full-length wildtype or one of the mutant NiV F constructs using the Fugene transfection reagent, as described above. Cells were harvested at 48 hours post transfection and were lysed in 500 µL buffer containing 0.1 M Tris pH 8.0, 0.1 M NaCl supplemented with complete protease inhibitor (Roche) and clarified by centrifugation. Clarified lysates were added to 2 µg of IgG followed by 50 µL of 20% slurry Protein G Sepharose for samples incubated with IgGs or 30 µL of 50% slurry S-protein agarose for those that were not.

To evaluate h5B3 chain binding to F, 300 µL of clarified untagged full-length F-expressing HEK 293T cell lysate was added to the h5B3 scFv-expressing culture supernatants and precipitated with 30 µL of 50% slurry of S-protein agarose.

In all cases, immunoprecipitation/pull-down were performed overnight at 4°C. The samples were washed 3 times with a buffer containing 1% Triton X-100, 0.1 M Tris pH 8.0, 0.1 M NaCl and subsequently boiled in reducing SDS-PAGE sample buffer followed by SDS-PAGE and Western blot analyses.

2.5.17 *HRB peptide triggering assay*

The capture assay was performed as previously described (Chan et al., 2012) with the addition of a competition step in the presence of an increasing amount of IgGs. Briefly, 1 µg of purified S-peptide tagged NiV F ectodomain trimer was cleaved with 10 ng of trypsin (New England Biolabs) in a 10 µl reaction volume of buffer at 4°C overnight to generate the mature F1 and F2 subunits. The reaction was stopped with 1 µl of 10X complete protease inhibitor cocktail (Roche). Subsequently, 2 µg of biotinylated NiV F HRB peptide was added in the presence or absence of competing IgG. The sample was heated for 15 min at 50°C, 60°C, 65°C or 70°C and the NiV F/HRB complex was subsequently pulled-down using 30 µl of 50% avidin-agarose slurry for 1 hour at 4ºC (Thermo Fisher Scientific). When indicated, the unbound fraction was pulled-down with Protein G Sepharose. Samples were washed 3 times with a buffer containing 1% Triton X-100, 0.1 M Tris pH 8.0, 0.1 M NaCl and boiled in 50 µL of reducing SDS-PAGE sample buffer. To analyze the precipitated product, a 25 µL sample was applied to a 4-12% BT SDS-PAGE (Invitrogen) followed by Western-blotting and detection using a rabbit anti-NiV F polyclonal antibody.

2.6 FIGURES & TABLES

Figure 2.1. The 5B3, 1F5 and 12B2 mAbs bind with NiV F and HeV F at high affinity. (Adapted from Dang et al., 2019. and Dang et al., 2021.)

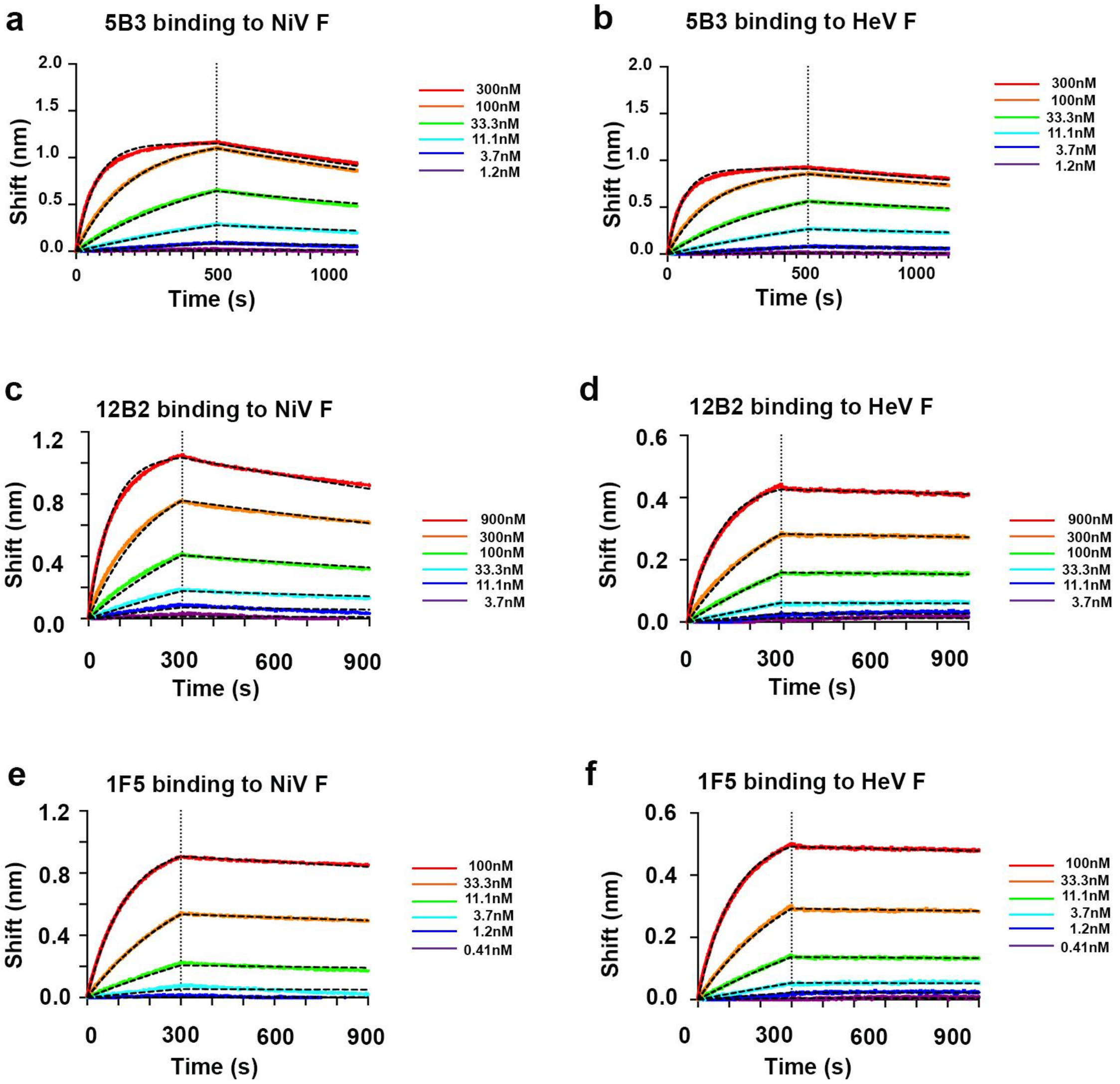

Binding of 5B3 (**a,b**), 1F5 (**c,d**), or 12B2 (**e,f**) Fab fragments to immobilized NiV F or HeV F ectodomains analyzed by biolayer interferometry. Raw data are colored according to the key and fitted curves are displayed as black dashed lines. The vertical dotted lines correspond to the transition between the association and dissociation phases. The experiments were performed in replicates with two different preparations of NiV F and of HeV F. One representative experiment is shown.

Figure 2.2. 5B3, 1F5 and 12B2 mAbs and their humanized versions neutralize three HNV strains. (Adapted from Dang et al., 2019. and Dang et al., 2021.)

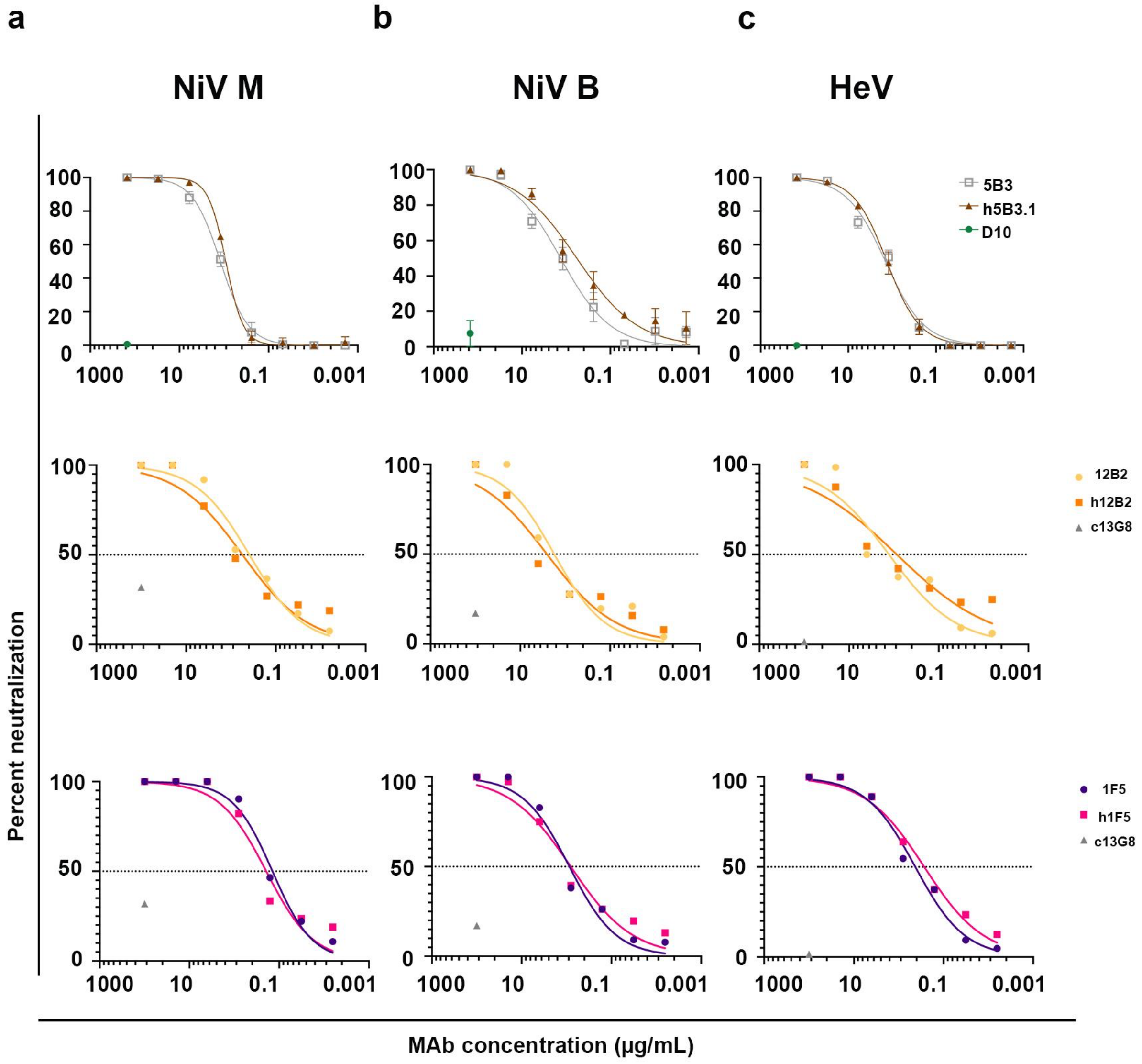

Neutralization of authentic NiV-M (**a**), NiV-B (**b**) and HeV (**c**) by 5B3, h5B3.1, 12B2, h12B2**,** 1F5 and h1F5 Abs. D10 and c13G8 (grey) are anti-HIV and anti-Crimean Congo hemorrhagic fever virus mAbs used as negative controls in each experiment. IC_{50} values for each replicate of the experiment are reported in **Table S2.2**.

Figure 2.3. 5B3, 1F5 and 12B2 inhibit membrane fusion mediated by NiV and HeV glycoproteins. (Adapted from Dang et al., 2021.)

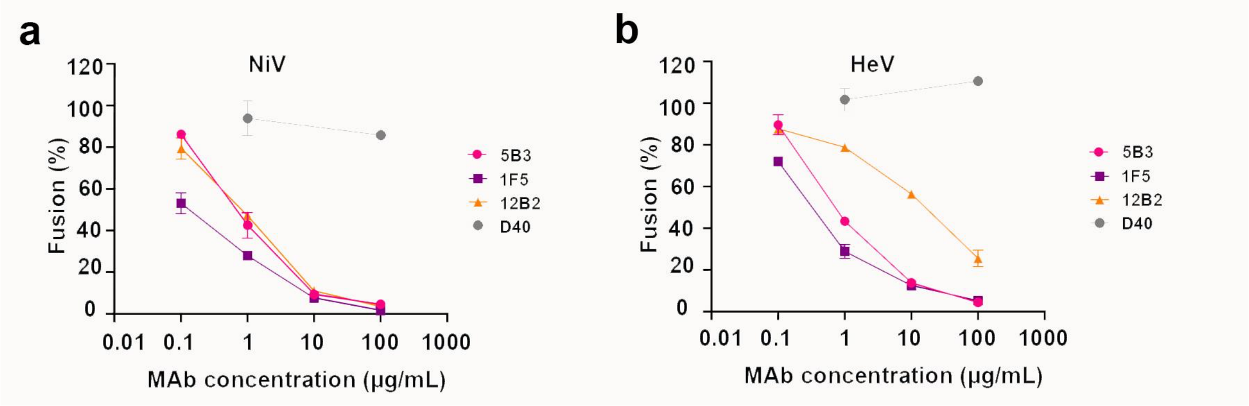

5B3 (**a**), 1F5 (**b**) and 12B2 (**c**) show membrane fusion inhibitory effects in a fusion inhibition assay with split luciferase. D40 is a mAb against HIV gp-41 used as a negative control.

Figure 2.4. Cryo-EM structure of NiV F in complex with the 5B3 neutralizing antibody. (Adapted from Dang et al., 2019.)

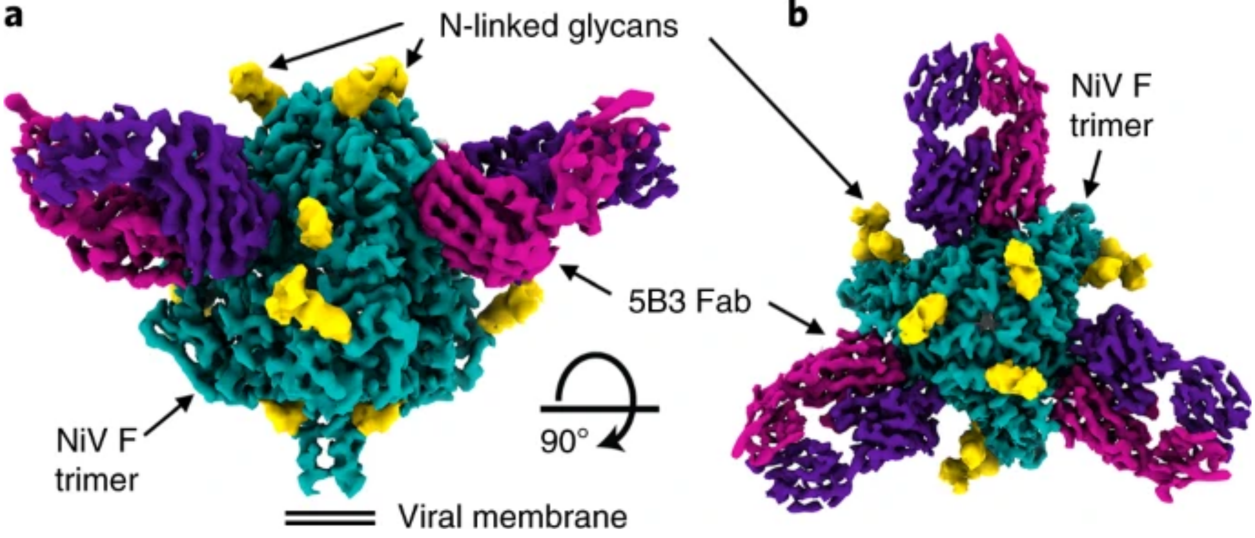

a-b, Two orthogonal views of the cryo-EM map at 3.5 Å resolution from the side (**a**) and from the top, facing toward the viral membrane (**b**). NiV F ectodomain trimer: teal, NiV F glycans: gold, 5B3 Fab heavy chain: purple, 5B3 Fab light chain: pink. The glycans are rendered using the unsharpened reconstruction.

Figure 2.5. The 5B3 neutralizing antibody recognizes a conserved quaternary epitope on the NiV F glycoprotein. (Adapted from Dang et al., 2019.)

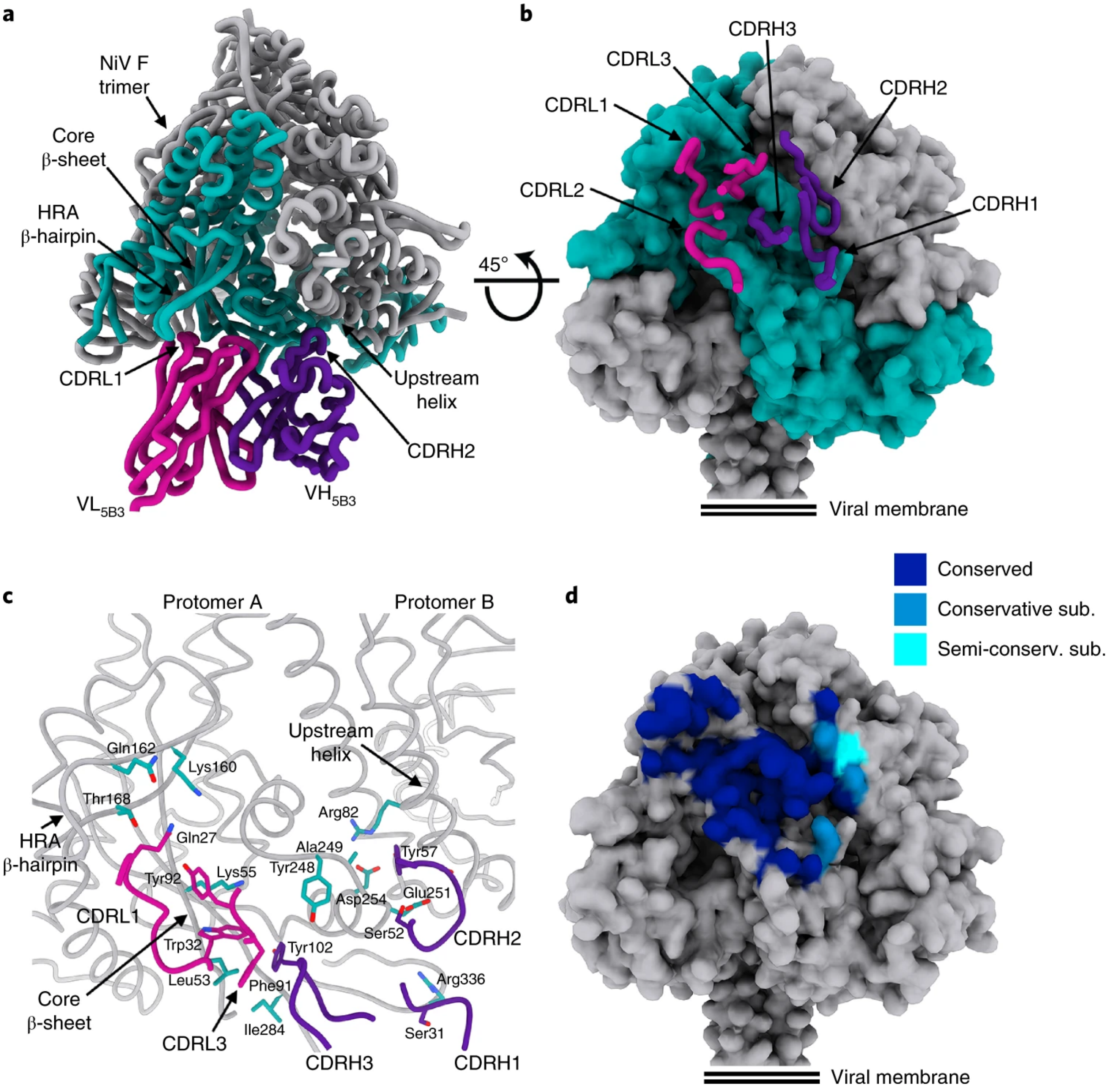

a, Ribbon diagram of the NiV F trimer in complex with the 5B3 Fab fragment. One F protomer is rendered in teal and the other two protomers in grey. Only one Fab fragment is shown for clarity. **b,** Molecular surface representation of the NiV F trimer with the 5B3 CDR loops shown as ribbons highlighting the quaternary nature of the epitope. **c,** Zoomed-in view of the interface between NiV F and 5B3 with selected residues rendered as sticks. NiV F residues are colored teal with oxygen and nitrogen atoms colored red and blue, respectively. In panels (a-c), the 5B3 variable heavy (VH_{5B3}) and light (VH_{5B3}) chains are colored purple and pink, respectively. **(D)** Molecular surface representation of the NiV F trimer showing the 5B3 footprint colored by residue conservation among NiV F and HeV F glycoproteins. Conservative sub: conservative substitution; semi-conservative sub: semi-conservative substitution.

Figure 2.6. The 5B3 and h5B3.1 neutralizing antibodies inhibit fusion by locking NiV F in the prefusion state. (Adapted from Dang et al., 2019.)

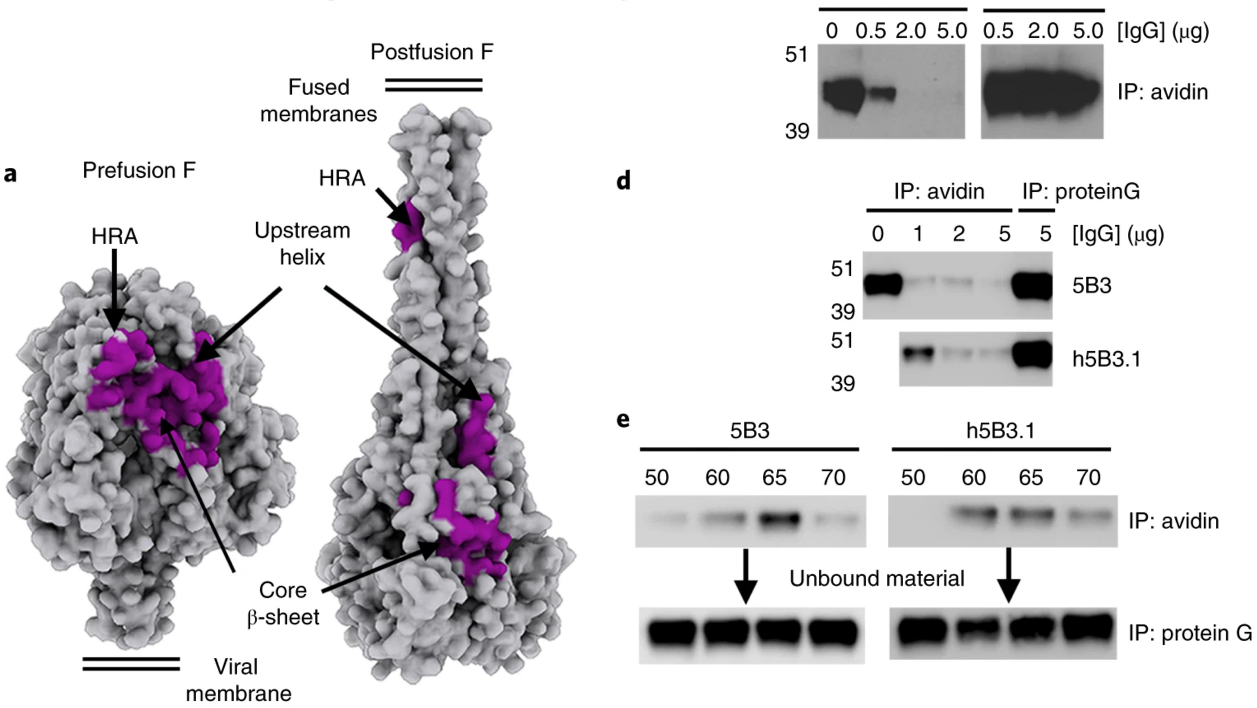

a, Molecular surface representation of the NiV F prefusion trimer showing the 5B3 footprint colored violet. **b,** Molecular surface representation of a homology model of the NiV F postfusion trimer showing the 5B3 footprint colored violet. Upon refolding, the 5B3 epitope is reorganized. The latter model was obtained by threading the NiV F sequence onto the human parainfluenza virus 3 postfusion F structure (Yin et al., 2005) (PDB ID 1ZTM) **c,** 5B3 concentration-dependent inhibition of streptavidin-mediated pulldown of a biotinylated HRB/NiV F conformational intermediate complex in a triggering assay. The non-neutralizing control antibody (13G5), which is specific for postfusion F, had no effect. **d,** NiV F triggering assay carried out in the presence of 5B3 or h5B3.1 IgGs showing both mAbs prevented F fusogenic conformational changes. Subsequent protein G immunoprecipitation of F/5B3 and F/h5B3.1 complexes that were not pulled-down by the biotinylated HRB-peptide indicated the antibodies remain bound to F. **e,** Capture of an F fusogenic conformational intermediate could be partially rescued by raising the temperature to ≥ 60˚C, as detected by comparing streptavidin-mediated pulldown and protein G immunoprecipitation of F/5B3 and F/h5B3.1 complexes. In panels **a-b**, a single 5B3 epitope is colored for clarity. In all panels, precipitated samples were analyzed by Western-blotting using a rabbit anti-F antibody. **f-g,** NiV F (**f**) or HeV F (**g**) mediated cell fusion could be inhibited by 5B3 or h5B3.1 in a concentration-dependent manner. D54 is an HIV envelope antibody used as negative control. Data shown are mean and s.d. for n= 2 experiments (technical replicates).

Figure 2.7. The 1F5 Ab recognizes a conserved quaternary epitope on the HeV glycoprotein. (Adapted from Dang et al., 2021.)

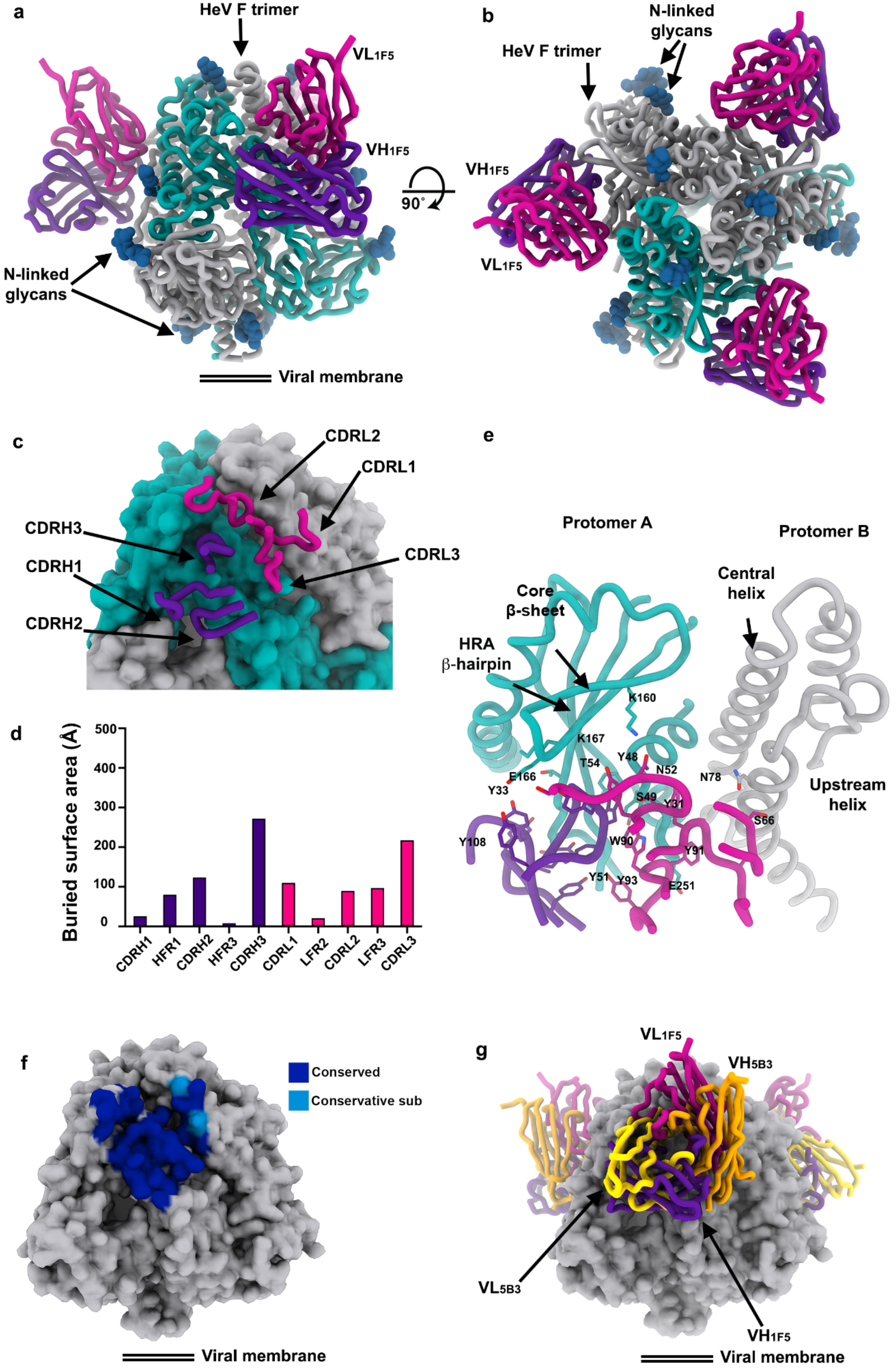

a-b, Ribbon diagrams showing two orthogonal views of the cryo-EM structure of the HeV F ectodomain trimer in complex with the 1F5 Fab fragment. One F protomer is rendered in teal and the other two protomers in grey. **c,** Molecular surface representation of the HeV F trimer with the CDR loops of a single 1F5 Fab shown as ribbons, highlighting the quaternary nature of the epitope. **d,** Contribution of distinct regions of 1F5 to epitope recognition at the surface of HeV F. CDRH: heavy chain complementary-determining region, CDRL: light chain complementary-determining region, HFR: heavy chain framework region, LFR: light chain framework region. **e**, Zoomed-in view of the interface between HeV F and 1F5 with selected residues rendered as sticks. One protomer of HeV F is colored in teal and an adjacent protomer in gray. In a-d, the 1F5 variable heavy (VH_{1F5}) and light (VL_{1F5}) chains are colored purple and pink, respectively. **f,** Molecular surface representation of the HeV F trimer showing the 1F5 footprint colored by residue conservation among HeV F and NiV F glycoproteins. Conservative sub: conservative substitution. **g,** Superimposition of the 1F5-bound and 5B3-bound HeV F and NiV F structures, respectively, showing the two Fabs adopt distinct orientations to recognize largely overlapping epitopes. The variable light chain (VL) and variable heavy chain (VH) of 5B3 are colored yellow and gold, respectively. The VL and VH of 1F5 are colored pink and purple, respectively.

Figure 2.8. The 12B2 Ab recognizes a conserved quaternary epitope on the NiV glycoprotein. (Adapted from Dang et al., 2021.)

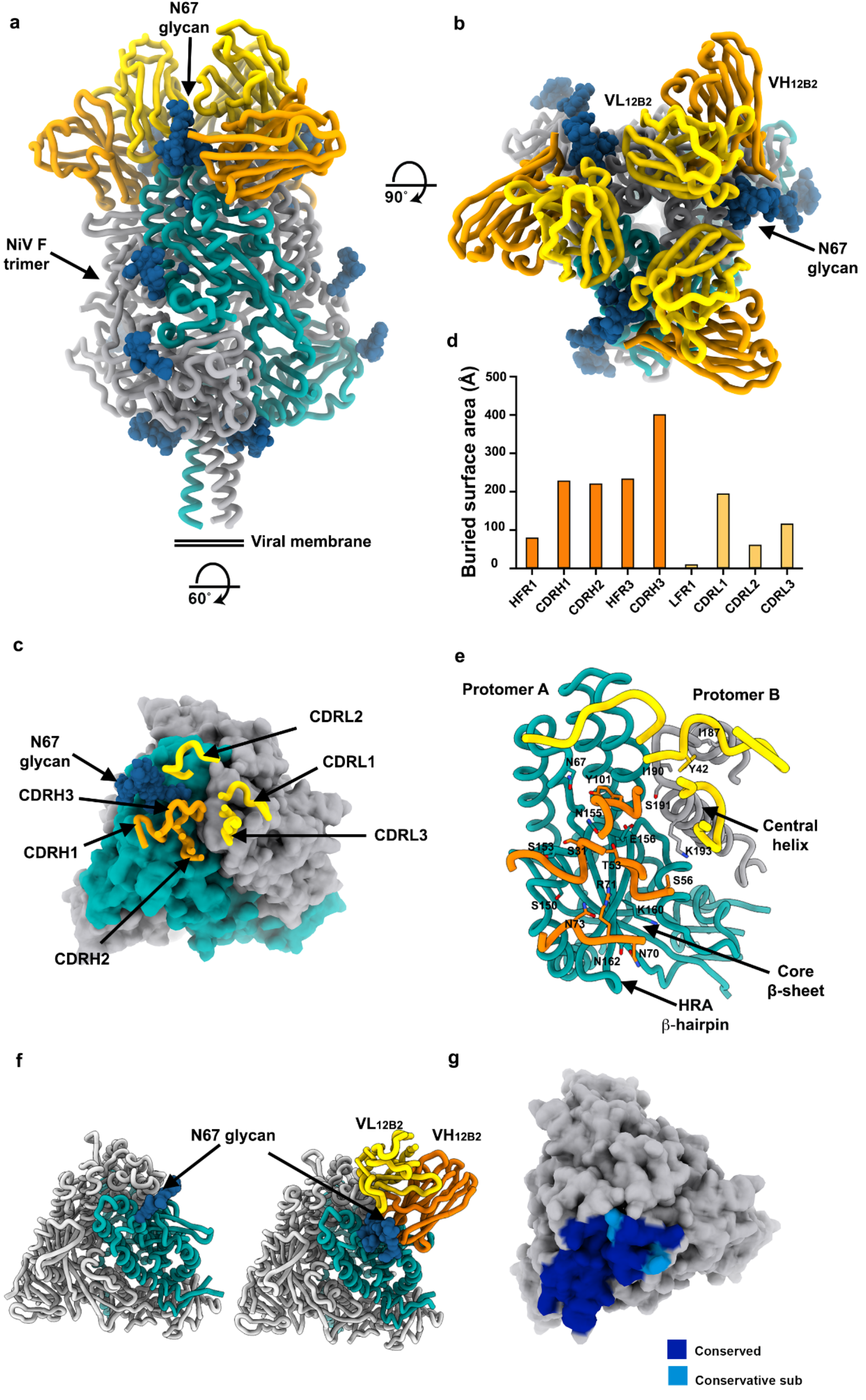

a-b, Ribbon diagrams showing two orthogonal views of the cryo-EM structure of the NiV F ectodomain trimer in complex with the 12B2 Fab fragment. One F protomer is rendered in teal and the other two protomers in grey. **c**, Molecular surface representation of the NiV F trimer with the CDR loops of a single 12B2 Fab shown as ribbons, highlighting the quaternary nature of the epitope. Only one Fab fragment is shown for clarity. **d**, Contribution of distinct regions of 12B2 to epitope recognition at the surface of NiV F. CDRH: heavy chain complementary-determining region, CDRL: light chain complementary-determining region, HFR: heavy chain framework region, LFR: light chain framework region. **e**, Zoomed-in view of the interface between NiV F and 12B2 with selected residues rendered as sticks. The NiV F glycan at position Asn67 is not shown. One protomer of NiV F is colored in teal and an adjacent protomer in gray. In **a-e**, the 12B2 variable heavy (VH12B2) and light (VL12B2) chains are colored orange and gold, respectively. **f**, Molecular surface representation of the NiV F trimer showing the 12B2 footprint colored by residue conservation among NiV F and HeV F glycoproteins. Conservative sub: conservative substitution. **g**, Comparison of NiV F without (left, PDB: 6TYS) and with bound 12B2 Fab (right) showing the rotation of NiV F glycan Asn67.

Figure 2.9. 5B3, 1F5 and 12B2 neutralize NiV and HeV by inhibiting membrane fusion. (Adapted from Dang et al., 2019. and Dang et al., 2021.)

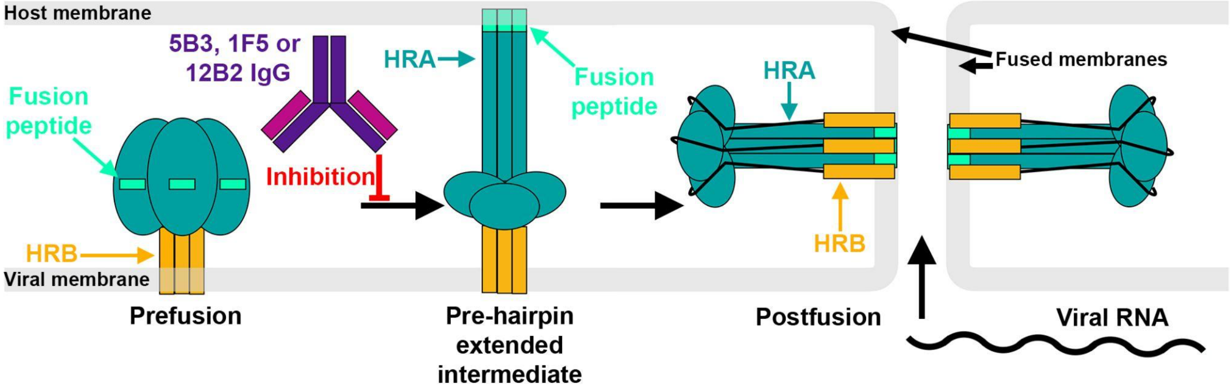

Model of F-mediated membrane fusion. NiV (or HeV) F forms metastable homotrimers at the viral surface. Upon interaction between NiV (or HeV) G and ephrinB2/B3, F undergoes large-scale conformational changes leading to insertion of the fusion peptide in the host cell membrane via forming a hypothetical pre-hairpin extended intermediate conformation (Harrison, 2015). Subsequent F refolding leads to the postfusion conformation and merger of the viral and host membranes. Addition of 5B3, 1F5 or 12B2 locks F in the prefusion conformation and inhibits membrane fusion.

Figure S2.1. Cryo-EM characterization of the NiV F glycoprotein in complex with the neutralizing antibody 5B3 Fab fragment. **(Adapted from Dang et al., 2019.)**

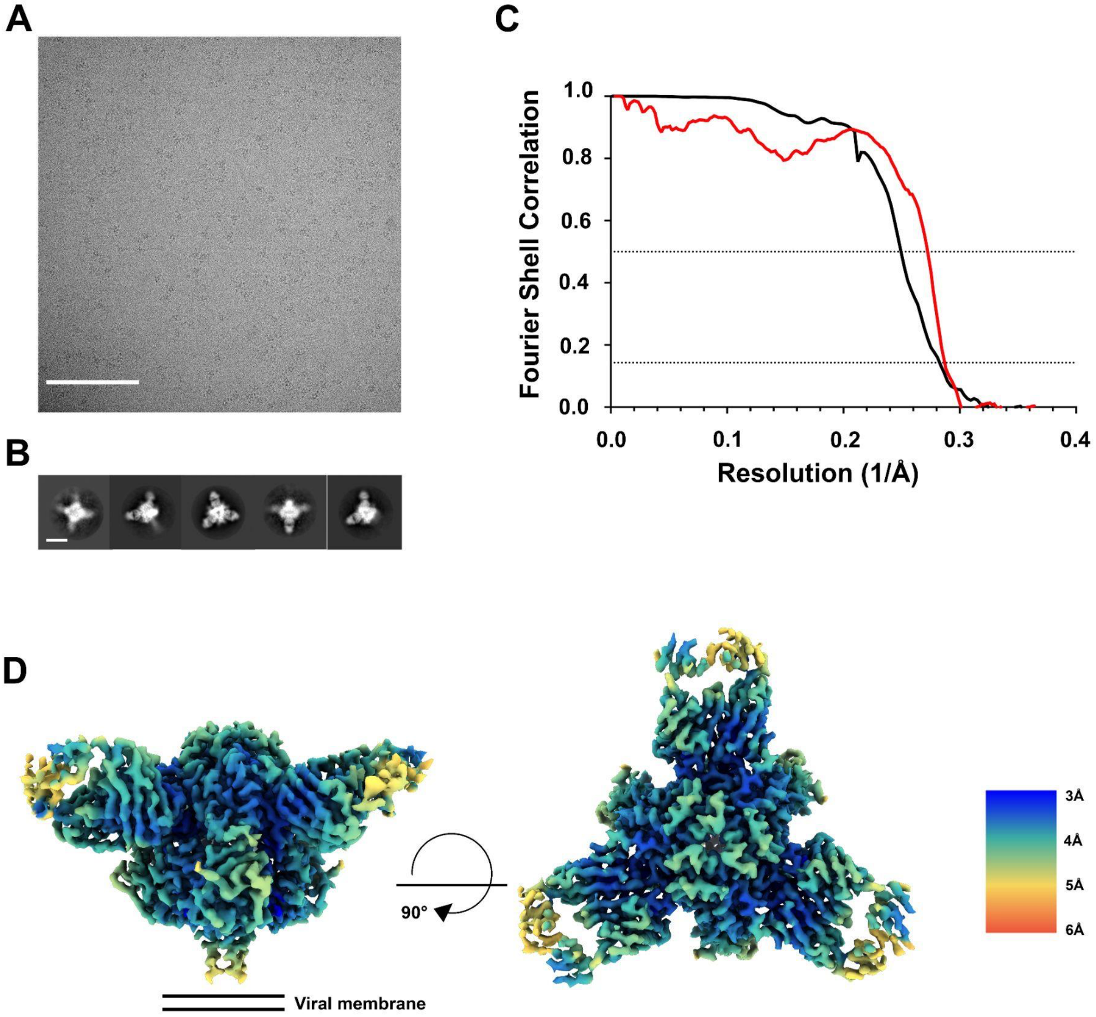

a, Representative micrograph. Scale bar, 100 nm. **b**, Reference-free 2D class averages. Scale bar, 100 Å. **c**, Gold-standard (black) and map/model (red) Fourier shell correlation curves. Dotted lines indicate 0.143 and 0.5 thresholds. **d**, Two orthogonal views of the cryo-EM reconstruction colored by local resolution computed using cryoSPARC. **e**, Enlarged view of the model with the cryo-EM reconstruction rendered as a blue mesh.

Figure S2.2. Architecture of the prefusion NiV F protein. (Adapted from Dang et al., 2019.)

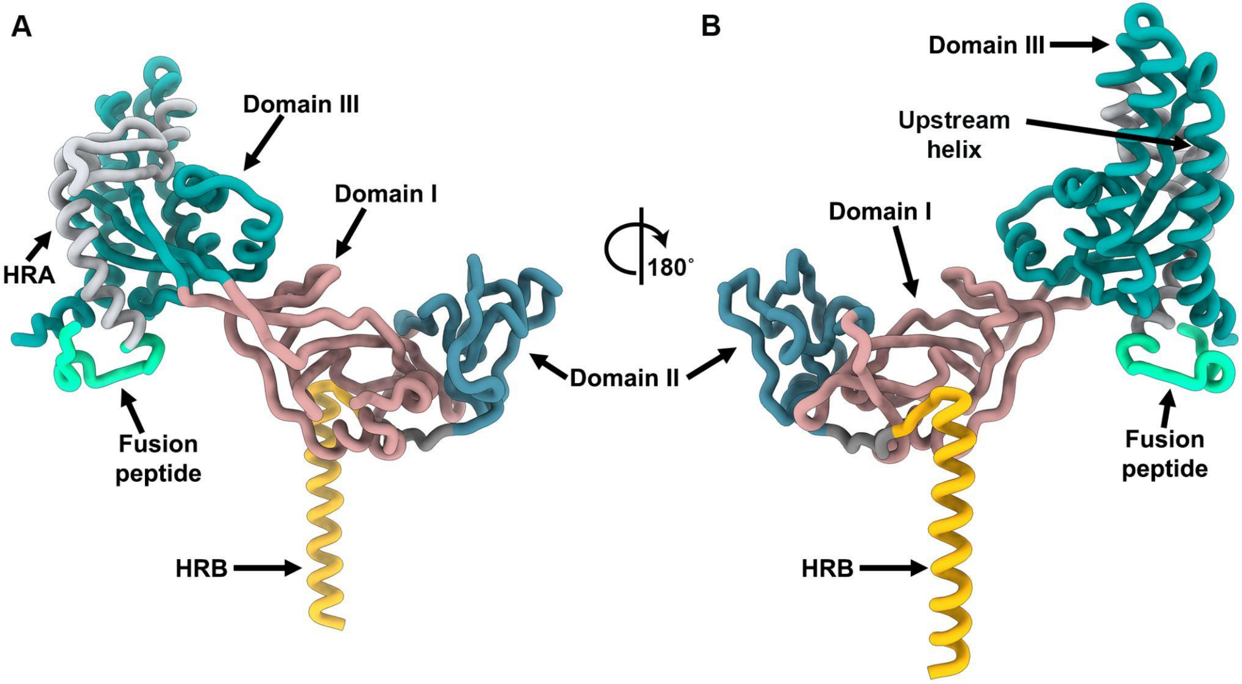

a,b, Ribbon diagrams of a NiV F ectodomain protomer from the cryo-EM structure of NiV F in complex with the 5B3 Fab fragment. HRA, heptad-repeat A; HRB, heptad-repeat B.

Figure S2.3. 5B3 binding is associated with a local structural reorganization of the HRA β-hairpin. (Adapted from Dang et al., 2019.)

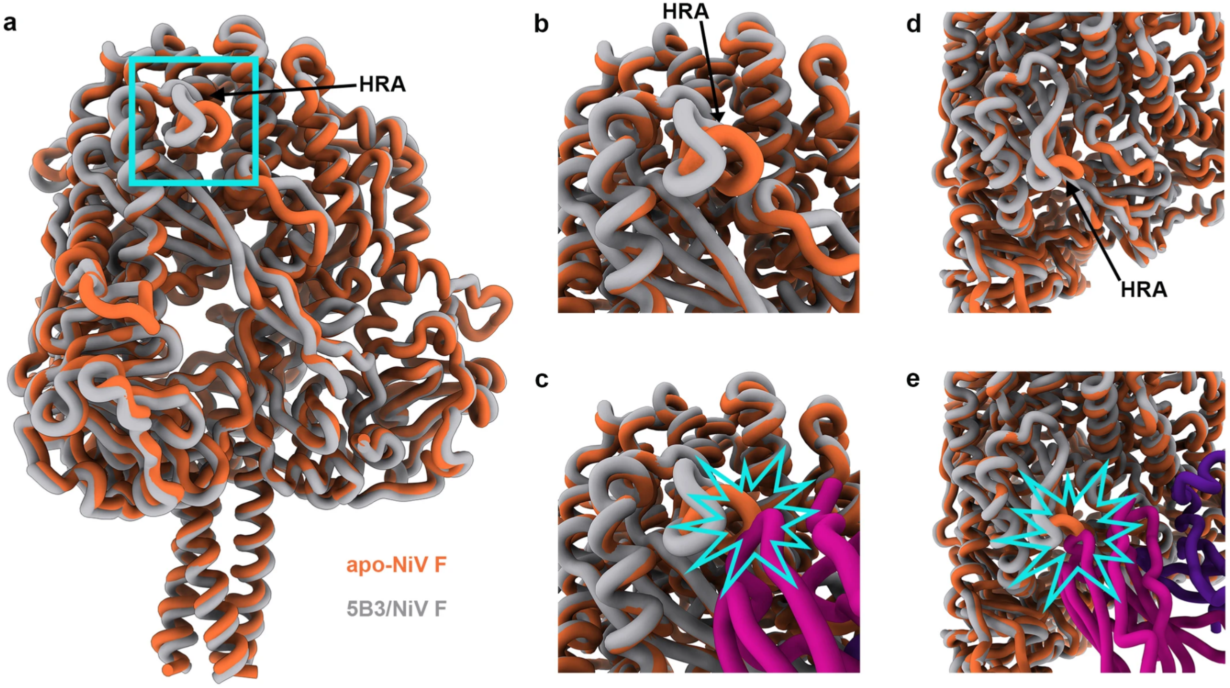

a, Ribbon diagrams of the superimposed 5B3-bound and apo NiV F trimers. The 5B3 Fab fragments are omitted for clarity. The cyan square highlights the region of the structure shown in **b**–**e**. **b**,**c**, Enlarged views showing the HRA conformational change. **d**,**e**, Enlarged views rotated 45° relative to **b** and **c**. In all panels, 5B3-bound and apo-NiV F trimers are rendered grey and orange, respectively. In **c**–**e**, one 5B3 Fab fragment is shown with its heavy and light chains colored purple and pink, respectively, whereas the cyan star indicates clashes that would occur between 5B3 and the HRA β-hairpin conformation observed in the apo-NiV structure (Xu et al., 2015) (PDB 5EVM).

Figure S2.4. Validation of the binding epitope of 5B3 on NiV F. (Adapted from Dang et al., 2019.)

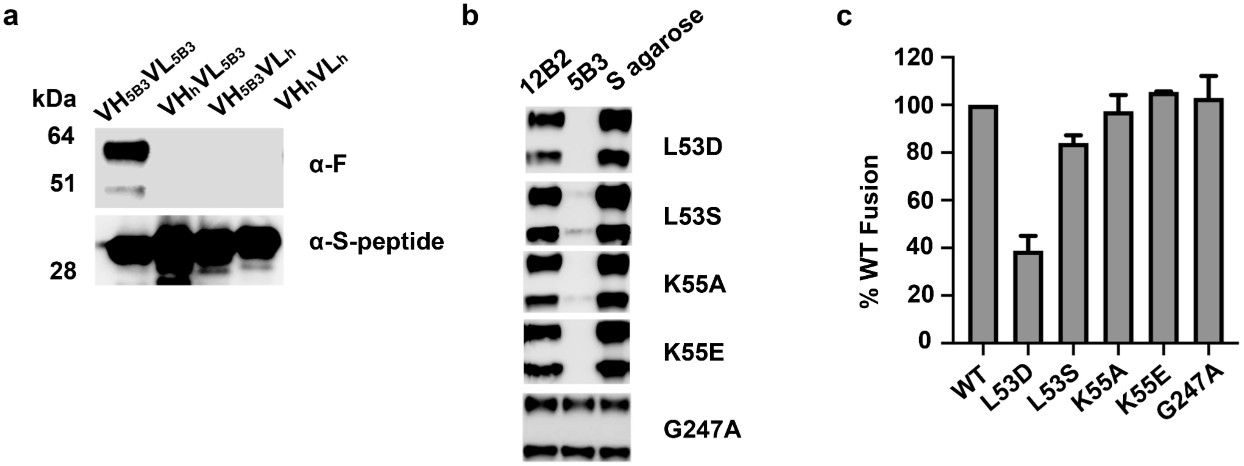

a, Analysis of h5B3 scFv binding to full-length NiV F. scFv chimeric constructs in which the variable heavy h5B3 chain (VH$_{5B3}$), the variable light h5B3 chain (VL$_{5B3}$) or both chains were replaced with unrelated chains (VH$_{h}$VL$_{h}$) from a human scFv library were assessed for binding to secreted wild-type NiV F. VH$_{5B3}$/VL$_{5B3}$ scFv was used as a positive control. Western blotting was carried out using an anti-F polyclonal antibody to detect NiV F or anti-S-peptide antibody to detect the scFv. **b**, Site-directed mutagenesis of the 5B3 epitope. A panel of S-peptide tagged NiV F ectdomain mutants were generated and expressed in HEK 293T cells. The F-expressing cell lysates were divided equally and incubated with 5B3, 12B2 or S-protein agarose before immunoprecipitation/pulldown. Samples in which mAb 5B3 or 12B2 were added were precipitated with protein G Sepharose. Western blotting detection of the precipitated products was carried out using an anti-S-peptide antibody. The Gly247Ala substitution was used as positive control. **c**, Cell–cell fusion mediated by the NiV F mutants shown in **b**. Data are the mean percentage of wild-type fusion levels for each mutant normalized relative to total F expression, as measured by densitometry of western blot bands. The bars represent the standard error from three separate experiments.

Figure S2.5. Cryo-EM characterization of HeV F in complex with the 1F5 Fab fragment. (Adapted from Dang et al., 2021.)

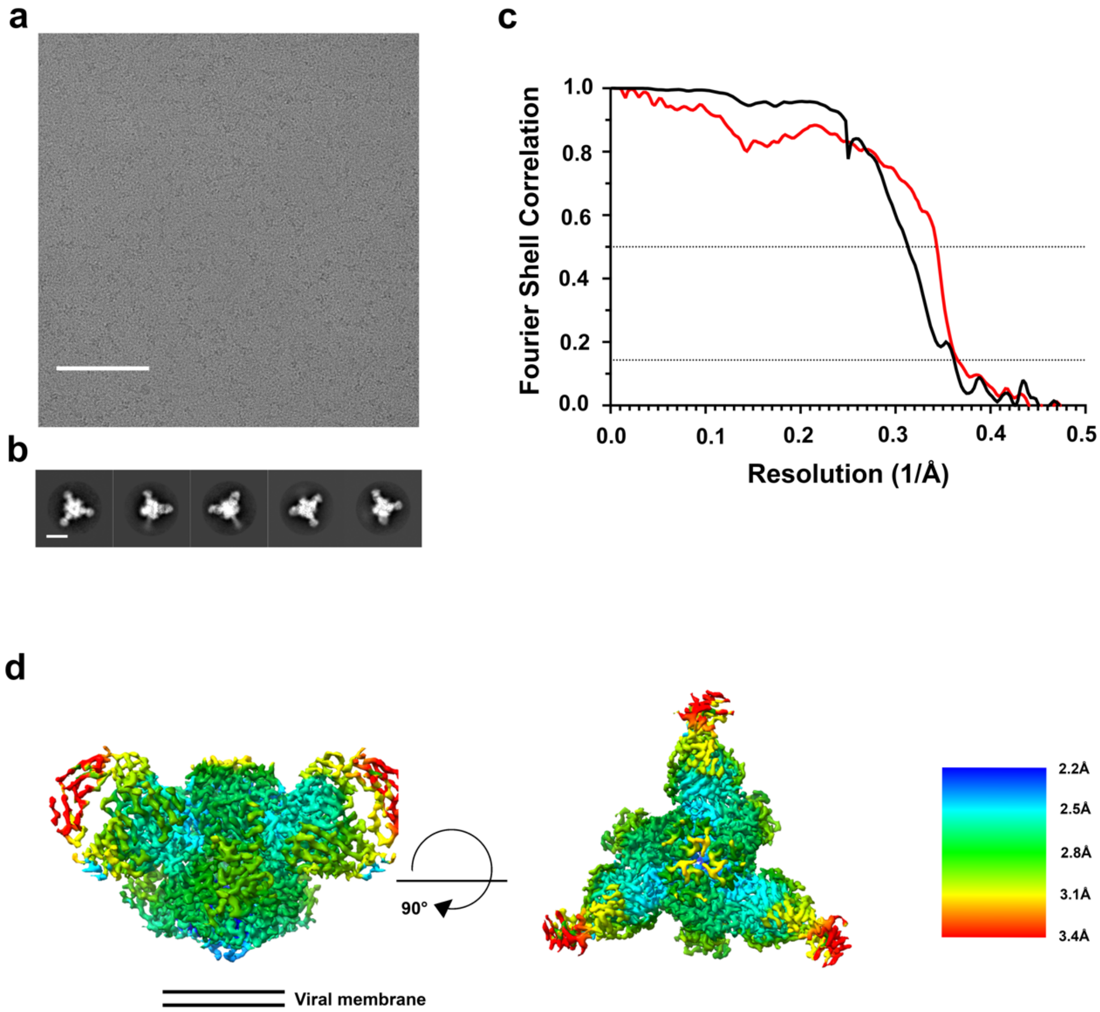

a, Representative micrograph. Scale bar, 100 nm. **b,** Reference-free 2D class averages. Scale bar, 100 Å. **c,** Gold-standard (black) and map-model (red) Fourier shell correlation curves. Dotted line indicates the 0.143 and 0.5 thresholds. **d,** Two orthogonal views of the cryo-EM map colored by local resolution in cryoSPARC.

Figure S2.6. Cryo-EM characterization of NiV F in complex with the 12B2 Fab fragment. (Adapted from Dang et al., 2021.)

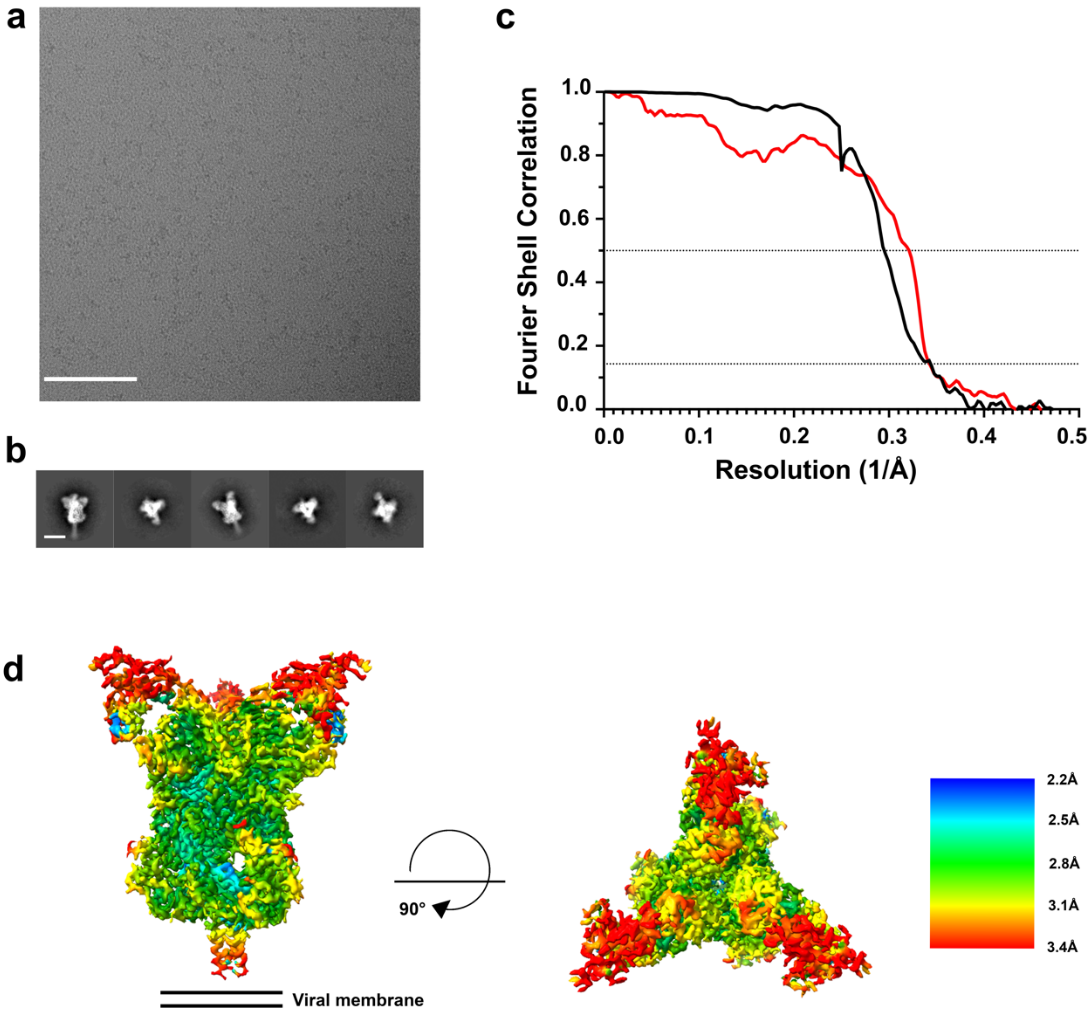

a, Representative micrograph. Scale bar, 100 nm. **b,** Reference-free 2D class averages. Scale bar, 100 Å. **c,** Gold-standard (black) and map-model (red) Fourier shell correlation curves. Dotted line indicates the 0.143 and 0.5 thresholds. **d,** Two orthogonal views of the cryo-EM map colored by local resolution in cryoSPARC.

Figure S2.7. Binding of the 12B2 Fab fragment to immobilized NiV F S69A ectodomain (N67 glycan mutant) analyzed by biolayer interferometry. (Adapted from Dang et al., 2021.)

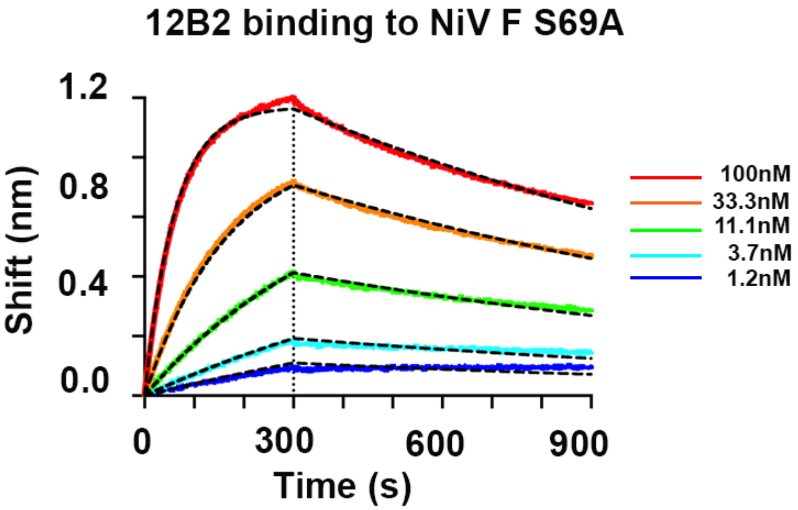

Raw data are colored according to the key and fitted curves are displayed as black dashed lines. The vertical dotted lines correspond to the transition between the association and dissociation phases.

Figure S2.8. Comparison of the footprints of the 12B2 and the 1F5 antibody on prefusion F and postfusion F and among F proteins from HNVs and Henipa-related viruses. (Adapted from Dang et al., 2021.)

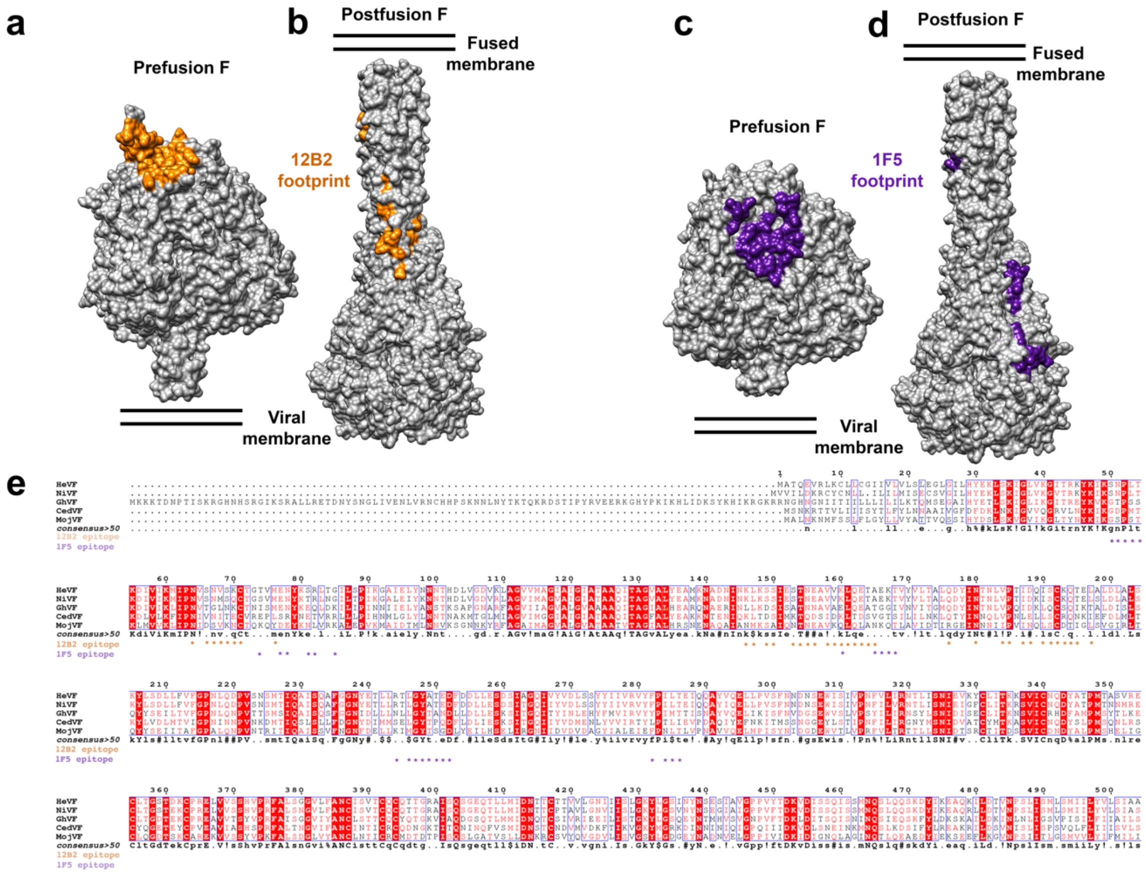

(a-b) Molecular surface representation of the NiV F prefusion trimer **(a)** and the homology model of NiV F postfusion **(b)** showing the 12B2 footprint in orange. **(c-d)** Molecular surface representation of the HeV F prefusion trimer **(c)** and the homology model of NiV F postfusion **(d)** showing the 1F5 footprint in purple. The homology model of NiV F postfusion in **(b)** and **(d)** was obtained by threading the NiV F sequence onto the human parainfluenza postfusion F structure (Yin et al., 2005) (PDB: 1ZTM). **e)** Sequence alignment of the fusion (F) proteins of HNVs and henipaviruses (GhV = Ghana bat virus; CedV = Cedar virus; MojVF = Mojiang virus). Residues on HNV F constituting the 12B2 or 1F5 epitope are denoted with an orange or purple asterisk, respectively.

Table 2.1. Cryo-EM data collection and refinement statistics (Adapted from Dang et al., 2019 and Dang et al., 2021.)

	NiV F/5B3 (EMD-20584, PDB 6TYS)	HeV F – 1F5 (EMD- 22885, PDB: 7KI6)	NiV F – 12B2 (EMD- 22884, PDB: 7KI4)
Data collection and processing			
Magnification	105000	130000	130000
Voltage (kV)	300	300	300
Electron exposure (e-/Å2)	40	70	70
Defocus range (μm)	1.0-3.2	0.6 - 3.2	0.9 - 3.5
Pixel size (Å)	1.37	1.05	1.05
Symmetry imposed	C3	C3	C3
Initial particle images (no.)	380,459	432222	525376
Final particle images (no.)	38756	34415	28776
Map resolution (Å)	3.5	2.8	2.9
FSC threshold	0.143	0.143	0.143
Refinement			
Model resolution (Å)	3.5	2.9	3.2
FSC threshold	0.5	0.5	0.5
Map sharpening B factor (Å2)	-103	-52	-51
Model composition			
Protein residues	2025	1986	2010
B factors (Å2)			
Protein	38.9	12.13	17.6
R.m.s. deviations			
Bond lengths (Å)	0.02	0.013	0.012
Bond angles (°)	1.9	1.31	1.26
Validation			
MolProbity score	0.71	1.07	1
Clashscore	0.65	2.83	1.35

Poor rotamers (%)	0.17	0.17	0
Ramachandran plot			
Favored (%)	98.05	98.78	97.28
Allowed (%)	100	1.22	2.57
EMRinger score	2.59	4.31	4.04

Table 2.2. X-ray crystallography data collection and refinement statistics (Adapted from Dang et al., 2019.)

	5B3 Fab (PDB 6U1T)
Data collection	
Space group	$C222_1$
Cell dimensions	
a, b, c (Å)	78.12, 95.01, 137.20
α, β, γ (°)	90, 90, 90
Resolution (Å)	68.6-1.48(1.56-1.48)
R_{sym} (%)	8.0(90.4)
I/σ (I)	10.2(1.3)
$CC_{1/2}$	0.998(0.472)
Completeness (%)	99.7(97.8)
Redundancy	5.6(3.6)
Refinement	
Resolution (Å)	68.6-1.48
No. reflections	79965
R_{work} / R_{free}	13.7/17.3
No. atoms	
Protein	3,577
Cl^- ion	1
Water	557
B factors	
Protein	21.1
Other atoms	37.9
R.m.s. deviations	
Bond lengths (Å)	0.01
Bond angles (°)	1.42
Validation	
MolProbity score	1.13
Clashscore	3.35
Poor rotamers (%)	0.92
Ramachandran plot	
Favored (%)	98.84
Allowed (%)	100

Tables S2.1. Binding kinetics of 5B3, 1F5 and 12B2 Fab fragments to NiV F, NiV F S69A mutant and HeV F ectodomains measured by BLI. Binding affinity (K_D), association (k_{on}) and dissociation (k_{off}) rate constants estimated with the ForteBio data analysis software are shown as an average of the duplicate experiments. The two biological replicates were performed with independent HeV F or NiV F ectodomain preparations. Related to **Figure 2.1**. **(Adapted from Dang et al., 2019 and Dang et al., 2021.)**

	Fab	**KD (nM)**	**kon ($M^{-1}s^{-1}$)**	**koff (s^{-1})**
NiV F	**5B3**	10.0	$3.84\text{x}10^4$	$3.88\text{x}10^{-4}$
	1F5	1.47	$8.1\text{x}10^4$	$1.19\text{x}10^{-4}$
	12B2	27.7	$1.4\text{x}10^4$	$3.85\text{x}10^{-4}$
HeV F	**5B3**	4.63	$4.97\text{x}10^4$	$2.3\text{x}10^{-5}$
	1F5	12.37	$9.5\text{x}10^4$	$1.25\ \text{x}10^{-4}$
	12B2	5.4	$3.6\text{x}10^3$	$1.92\text{x}10^{-5}$
NiV F S69A	**12B2**	4.0	$1.88\text{x}10^5$	$7.32\text{x}10^{-4}$

Table S2.2. Half-maximal inhibitory concentrations (IC50) in ug/mL of murine mAbs 5B3, 1F5, 12B2, their respective humanized versions (h5B3.1, h1F5, h12B2) and mAb cocktails of h12B2/h1F5 and h12B2/h5B3.1 against authentic HeV, NiV-M and NiV-B for as an average from two or three replicates. Data for 5B3 and h5B3.1 were performed in triplicates. Data for 1F5, h1F5, 12B2, h12B2, h12B2+h1F5, and h12B2+h5B3.1 were performed in duplicates. Related to **Figure 2.2. (Adapted from Dang et al., 2019 and Dang et al., 2021.)**

IC50 (ug/mL)	5B3	h5B3.1	1F5	h1f5	12B2	h12b2
HeV	1.4	1.32	0.59	0.47	0.15	0.15
NiV M	1.3	0.92	0.16	0.21	0.47	0.11
NiV B	0.140	0.60	0.11	0.10	0.18	3.09

Chapter 3. ANTIBODY COCKTAILS TARGETING THE HENIPAVIRUS FUSION GLYCOPROTEIN

Adapted from.

Dang, Ha V., *et al*. "(Dang et al., 2021)." *Nature Structural & Molecular Biology* 28.5 (2021): 426-434.

In Chapter 2, we isolated and characterized three monoclonal antibodies (1F5, 5B3 and 12B2) targeting the Fusion (F) protein of HNVs. We showed that each of these mAbs potently inhibited authentic HNV virions from three different strains from entering permissive cells. However, as for other RNA viruses, the high mutation rate of HNVs could yield variants able to overcome monoclonal antibody inhibition. Antibody cocktails targeting multiple "vulnerable" spots on essential viral proteins may curtail the emergence of escape mutants. In this chapter, we tested whether HNVs can escape neutralization by 1F5, 5B3 or 12B2 and explored the possibility of using these mAbs in a cocktail format to neutralize HNVs.

3.1 ISOLATION OF ESCAPE MUTANTS FROM ANTI-F NEUTRALIZING MABS

Previously we showed that passaging NiV or HeV with anti-HNV G antibodies led to the isolation of viral mutants escaping neutralization by the respective antibodies (Borisevich et al., 2016; Xu et al., 2013). To assess the possibility of generating neutralization-escape virus mutants, we passaged authentic NiV in presence of 1F5, 5B3 or 12B2 in BSL-4 containment. Plaque purified resistant viruses were isolated and viral RNA from five NiV isolates was reverse-transcribed into cDNA for sequencing of the F gene. Although we could not isolate escape mutants for 1F5 (in two independent laboratories), 12B2 selected for the S191R escape mutant which lies within the 12B2 epitope. For 5B3, all five NiV escape mutants harbored the same F K55E substitution. This finding supports our previous mutagenesis data since the NiV F K55A was completely defective in 5B3 binding. We recombinantly produced the K55E F mutant and observed it could not bind 5B3 while maintaining its ability to interact with 12B2 and to promote wild-type cell-cell fusion activity (**Chapter 2, Fig. S2.4 b**). These experiments are in full agreement with our structural and biochemical data and show that NiV could escape mAb neutralization without affecting F-mediated fusion, although the impact of the identified substitution on viral growth is not known. We therefore set out to formulate Ab cocktails combining the benefits of multiple monoclonal Abs.

3.2 1F5/12B2 OR 5B3/12B2 CAN SIMULTANEOUSLY BIND TO HNV F

We first tested whether 1F5, 5B3 and 12B2 can pairwise engage HNV F. High-resolution structures of binary complexes of F with 1F5, 5B3 or 12B2 Fab allows us to superimpose these structures and analyze potential steric clashes (Dang et al., 2019, 2021). Superimposition of the NiV F/12B2 and NiV F/5B3 structures indicates that no steric hindrance would occur between the variable domains (or the Fab fragments) as a result of binding to the same F protomer within a trimer. Superimposition of the HeV F/1F5 and NiV F/12B2 structures, however, suggests the framework of the two Fab variable domains could sterically clash upon recognition of a single F protomer within the trimer although they bind to entirely distinct epitopes (**Fig. 3.1 a-b)**

We therefore assessed if combinations of two Fabs targeting different F regions could simultaneously interact with NiV F by determining three-dimensional EM reconstructions of the following two negative-stained ternary complexes: NiV F/12B2/5B3 and NiV F/12B2/1F5. The resulting EM structures suggest F can simultaneously interact with the 12B2 and 5B3 Fabs or with the 12B2 and 1F5 Fabs, indicating these Ab cocktails should be further evaluated (**Fig. S3.1**). The ability of F to simultaneously engage 12B2 and 1F5 or 12B2 and 5B3 was further corroborated in a competitive binding experiment using BLI (**Fig. 3.1 c**). After saturation with either 1F5 or 5B3 Fab during the association phase 1, NiV F could subsequently recognize the 12B2 Fab fragment as observed during the association phase 2. The larger magnitude of the binding signal observed for 12B2 binding to the F/5B3 complex compared to the F/1F5 complex (**Fig. 3.1 c**) supports our structural data and likely resulted from steric hindrance between the 12B2 and 1F5 Fabs upon recognition of the same F protomer within the trimer.

3.3 1F5/12B2 AND 5B3/12B2 ANTIBODY COCKTAILS PREVENT MEMBRANE FUSION AND NEUTRALIZE HEV AND NIV

Using the split luciferase-reporter-based cell-cell fusion assay, we observed that Ab cocktails comprising 12B2 and either 5B3 or 1F5 have the same inhibitory effect than single mAb treatment on HNV F/G-mediated membrane fusion (**Fig. 3.2 a-b, Table S3.1; Chapter 2: Fig. 2.2, Table S2.2**).

Next, we compared the neutralization potency and breadth of the humanized mAb cocktails, h12B2/h5B3.1 and h12B2/h1F5, to the three individual Abs by plaque reduction assays. The different data points were obtained by utilizing either a given concentration of a single mAb or half the concentration of the two mAbs combined to allow side-by-side comparison. Collectively, the data show that both Ab cocktails can neutralize NiV-M, NiV-B and HeV *in vitro* **(Fig. 3.2 c and Table S3.1).** Kruskal-Walis tests show that there is no statistical difference between the potency of each mAb cocktail compared with those of each component mAb (**Table S3.1**, see **Materials & Methods**). These findings provide proof-of-concept that neutralizing Abs recognizing distinct F epitopes could be used in combination to inhibit NiV and HeV entry into host cells and are likely to prevent or limit the emergence of neutralization escape mutants.

3.4 CHAPTER DISCUSSION

Ab cocktails represent a promising strategy to combat emerging and reemerging viruses which typically exhibit high mutation rates contributing to immune evasion. Administering multiple Abs simultaneously can mimic the benefits of natural polyclonal Ab responses, such as neutralization breadth and potency as well as reduction of the frequency of emergence of escape mutants, in a fully tailored and controllable manner. REGN-EB3 is an example of an Ab cocktail providing complete *in vivo* protection of non-human primates from a lethal dose of Ebola virus (Mulangu et al., 2019) and has been shown to provide significant protection in a Phase 3 study in patients infected with Ebola virus (Bornholdt et al., 2019) and was recently approved by the FDA. MBP134^{AF} is a more recently developed Ab cocktail that provides protection of non-human primates against Ebola virus, Sudan virus and Bundibugyo virus after injection of a single dose up to several days post-infection (Logtenberg, 2007; Wec et al., 2019). Furthermore, several studies have suggested the use of well-characterized Ab cocktails as a replacement for polyclonal human or equine Abs which are currently used for post-exposure treatment of rabies (Amaya & Broder, 2020; Chao et al., 2017; Dessain, 2007).

In previous studies, we successfully generated humanized versions of 12B2 and 1F5 with equivalent neutralization potency to the parental murine versions. Our high-resolution structural data demonstrate that 12B2 and 5B3 or 12B2 and 1F5 can simultaneously interact with F, which led us to investigate the use of Ab cocktails on HNV neutralization. Using binding assays and negative staining EM, we showed that 12B2 can simultaneously engage F with either 1F5 or 5B3. We then showed that both h12B2/5B3.1 and h12B2/h1F5 humanized mAb cocktails have a neutralization potency comparable to each individual Ab component. These two-Ab cocktails could be tailored to include 3 mAbs: m102.4, to prevent receptor engagement at the host cell surface, and 12B2 with 1F5 or 5B3, to inhibit F-mediated membrane fusion. Such a trivalent cocktail would inhibit multiple viral functions involved in host cell entry, and limit further the risk of emergence of viral mutants escaping neutralization by targeting multiple different epitopes. We therefore expect that cocktail Ab therapies will emerge as promising effective countermeasures against HNVs and should be explored in future *in vivo* protection studies.

3.5 MATERIALS & METHODS

3.5.1 *Protein constructs, expression, and purification*

The protein constructs used in this study were expressed and purified as described previously in **Chapter 2** (**Sections 2.6**). These proteins include S-tagged NiV F, murine and humanized 1F5, 5B3, and 12B2 IgGs and Fabs.

3.5.2 *Escape mutant analysis*

For 5B3 IgG, neutralization-resistant NiV mutants were generated by incubating 1 x 10^5 50% Tissue culture Infective Dose ($TCID_{50}$) of each virus with a sub-neutralizing concentration of 40 µg of 5B3 IgG, in 100 µL media for 1 hour at 37°C and then inoculated onto 10^6 Vero E6 cells in the presence of IgG at the same concentration. The development of cytopathic effects was monitored over 72 hours and progeny viruses were harvested. IgG treatment was repeated two additional times with cytopathic effects developing slowly with each passage. Viruses from the third passage were plaque purified in the presence of IgG and neutralization resistant viruses were isolated. The experiment was performed in duplicate and the F and G glycoprotein genes of 5 individual plaques were sequenced. The neutralization titers between wild-type and the neutralization resistant virus were determined using a micro-neutralization assay. Briefly, the 5B3 IgG was serially diluted two-fold and incubated with 100 $TCID_{50}$ of the wild-type and neutralization-resistant NiV for 1 hour at 37ºC. Virus and antibodies were then added to a 96-well plate with 2 x 10^4 Vero E6/well in 4 wells per antibody dilution. Wells were checked for cytopathic effects 3 days post infection and the mean half-maximal inhibitory concentration was determined as the mAb concentration at which at least 50% of wells showed no cytopathic effects.

For 1F5 and 12B2 IgGs, authentic NiV-M was passaged 3 times in the presence of 100 µg of antibody at each passage. The first passage was in the presence of 50,000 PFU of NiV-M and the additional passages were against 5,000 PFU (if possible). During each passage, the virus was incubated with 100 µg of each antibody in 100 µL total volume for 1 hour at 37°C with rocking and flicking every 15 minutes. The total volume was raised to 200µL by addition of 10% FBS in DMEM and incubated on Vero 76 cells in a 35 mm well, rocking every 15 minutes for 1 hour at 37°C. After the inoculum was removed, 10% FBS in DMEM containing 100 µg of F mAb in the final inoculum and supernatants were collected 72 hpi. Supernatant from each passage was titered by plaque assay with Vero 76 cells. Briefly, increasing 10-fold dilutions of the samples were adsorbed to Vero cell monolayers in duplicate wells (200 µl); the limit of detection was 25 pfu/ml. Virus from the third passage was diluted to ~100 PFU and incubated with 100µg of each F mAb in 100µl of total volume for 1 hour at 37°C with rocking/flicking every 15 minutes. The volume of the virus-F mAb mixture was then raised to 200 µL by addition of 10% FBS DMEM and incubated on Vero 76 cells in a 35 mm well, rocking every 15 minutes for an hour at 37°C. Cells were then overlaid with 0.9% agarose EMEM and observed for plaque formation 24 to 48 hours post-overlay. 5 plaques per F mAb and per virus were picked using a P1000 pipette tip and placed into 500 µL of 10% FBS DMEM and allowed to diffuse for 10 minutes at room temperature and then placed at -80°C.

Plaque purified virus preparations were used to inoculate Vero 76 cells by rocking every 15 minutes for an hour at 37°C. After the inoculum was removed, 10% FBS DMEM was added and supernatants were collected 72 hpi and 200µl of supernatants were placed into 1ml of Trizol LS for RNA extraction following manufacturer's instructions (Life Technologies). RNA was reconstituted into 30 µL of nuclease-free dH2O.

3.5.3 *Sequential mAb binding assay with Biolayer interferometry*

Assays were performed with an Octet Red 96 instrument (ForteBio, Inc.) at 30°C while shaking at 1,000 rpm. All measurements were corrected by subtracting the background signal obtained from biosensors without immobilized S-peptide tagged NiV F in phosphate buffered saline at pH 7.4 were diluted to 20 µg/mL in 10mM acetate buffer pH 5.0 before immobilization on (NHS-EDC activated) Amine Reactive 2nd Generation (AR2G, ForteBio) biosensors for 300s. Sensors were then quenched in 1M ethanolamine (ForteBio) for 300s and incubated in kinetics buffer (KB: 1X PBS, 0.001% BSA, 0.02% Tween 20 and 0.005% NaN_3 (ForteBio)) for 300s to establish the baseline signal (nm shift).

NiV F-loaded AR2G sensors were immersed into solutions of purified 1F5 or 5B3 Fab at 600mM in association phase 1 and then into two-Fab solutions containing 600mM 1F5 + 1200nM 12B2 Fabs or 600mM 5B3 + 1200nM 12B2 in association phase 2. All Fab solutions were diluted to the desired concentrations in KB.

3.5.4 *Negative staining electron microscopy (nsEM) analysis*

S-peptide tagged NiV F ectodomain was incubated overnight at 4°C with 12B2/1F5 Fabs or 12B2/5B3 Fabs at a molar ratio of 1:6:3 NiV F:12B2:1F5 or NiV F:12B2:5B3. Each complex was diluted to a concentration of 0.01mg/mL NiV F immediately before absorption onto glow-discharged carbon-coated copper grids for 20s, followed by 2X application of 2% uranyl formate stain. Micrographs were recorded using Leginon software (Suloway et al., 2005) on a 120kV FEI Tecnai G2 Spirit with a Gatan Ultrascan 4000 4k x 4k CCD camera at 67,0000 nominal magnification at a defocus range of 1.5 – 2.5 µm and pixel size 1.6 Å. Particles were picked using DoGPicker, a reference-free picker (N. R. Voss et al., 2009). Contrast-transfer function was estimated using GCTF (K. Zhang, 2016). 2D class averages were generated in cryoSPARC (Punjani et al., 2017). Reference-free *ab initio* 3D reconstruction of selected particles from 2D class averages from each dataset was performed in cryoSPARC with 8 classes. The 3D reconstructed classes with the highest stoichiometry of Fabs bound are colored and shown in **Figure S3.1 a**.

3.5.5 *Split-luciferase assay*

The quantitative fusion inhibition assay was based on a dual-split-reporter described previously (Kondo et al., 2010; Laing et al., 2019). Receptor negative CHO745 cells (7 × 10^5 in a 6-well plate) were transfected with 0.75 µg each of the indicated HNV F and G glycoprotein expression plasmids and 0.5 µg of an expression plasmid for one half of a split-luciferase reporter protein (DSP1–7, a kind gift of Z. Matsuda). GeneJuice reagent (Millipore Sigma) was used for transfections according to manufacturer's instructions. Concurrently, CHO745-ephrin-B2 cells (1 × 10^4 cells in a clear-bottom, black wall 96-well plate) were transfected with 100 ng of the expression plasmid for other half of the split-luciferase reporter protein (DSP8-11). 24 hours post-transfection, Versene (0.48 mM EDTA in PBS) (ThermoFisher Scientific) was used to gently detach the CHO745 cells from the 6-well plate and 2.5 × 10^4 cells were incubated for 15 minutes at room temperature with the indicated mAb dilutions prior to been over-laid on the receptor-expressing CHO745-ephrin-B2 cells in the 96-well plate. Single mAbs (1F5, 5B3, and 12B2) were used at 100, 10, 1 and 0.1 ng/mL. Cocktail mAbs (12B2/1F5 and 12B2/5B3) were used at 50, 5, 0.5, 0.25 and 0.125ng/mL of each mAb. Negative control mAb D40 (HIV-gp41-specific mAb) was tested at 100 and 1ng/uL. EnduRen (Promega; WI, USA) was added as the substrate to the culture medium (DMEM, 10%. FBS) according to the manufacturer's instructions. Reconstitution of luciferase function as a result of content mixing driven by cell-cell fusion between the glycoprotein expressing CHO745 cells and the receptor-bearing CHO745-ephrin-B2 cells was measured using an Infinite M200 Pro microplate reader (Tecan; Switzerland). Each data point is comprised of at least 2 technical repeats. The luciferase signal in the sample where there was no mAb added was used to define "100% fusion" and calculate membrane fusion percentage for each mAb treatment.

3.5.6 *Neutralization assay*

The virus infectivity neutralization concentrations of a control antibody c13G8 IgG specific to the GP38 protein of Crimean-Congo hemorrhagic fever virus (CCHFV) (Mishra et al., 2020), murine 1F5 IgG, humanized h1F5 IgG, murine 12B2 IgG, humanized h12B2 IgG, and antibodies cocktail (h12B2/h1F5, h12B2/h5B3.1) were determined for NiV-M, NiV-B and HeV using a plaque reduction assay. Briefly, antibodies were serially diluted fivefold from 100 µg/ml to 6.4 ng/ml and incubated with a target of ~ 100 PFU of NiV-M, NiV-B or HeV for 45 minutes at 37°C. In the case of antibody cocktails, each mAb component in the cocktail was present at half of the indicated concentrations. The control mAb c13G8 was tested only at the highest concentration (100µg/mL). Virus and antibody mixtures were then added to individual wells of 6-well plates of VeroE6 cells. Plates were stained with neutral red 2 days after infection and plaques were counted 24 h after staining. Neutralization potency was calculated based on PFU for each virus in the well without antibody. The experiments were performed in duplicate with independent virus preparations and duplicate readings for each replicate. Mean half-maximal inhibitory concentrations (IC50) were calculated as previously described (Ferrara & Temperton, 2018). Kruskal-Wallis tests were used in Prism to compare groups of IC50 values determined from each replicate experiment for single mAbs vs. mAb cocktails to assess whether they were statistically different.

3.6 FIGURES & TABLES

Figure 3.1. Formulation of F-targeted Abs cocktails against NiV and HeV. (Adapted from Dang et al., 2021.)

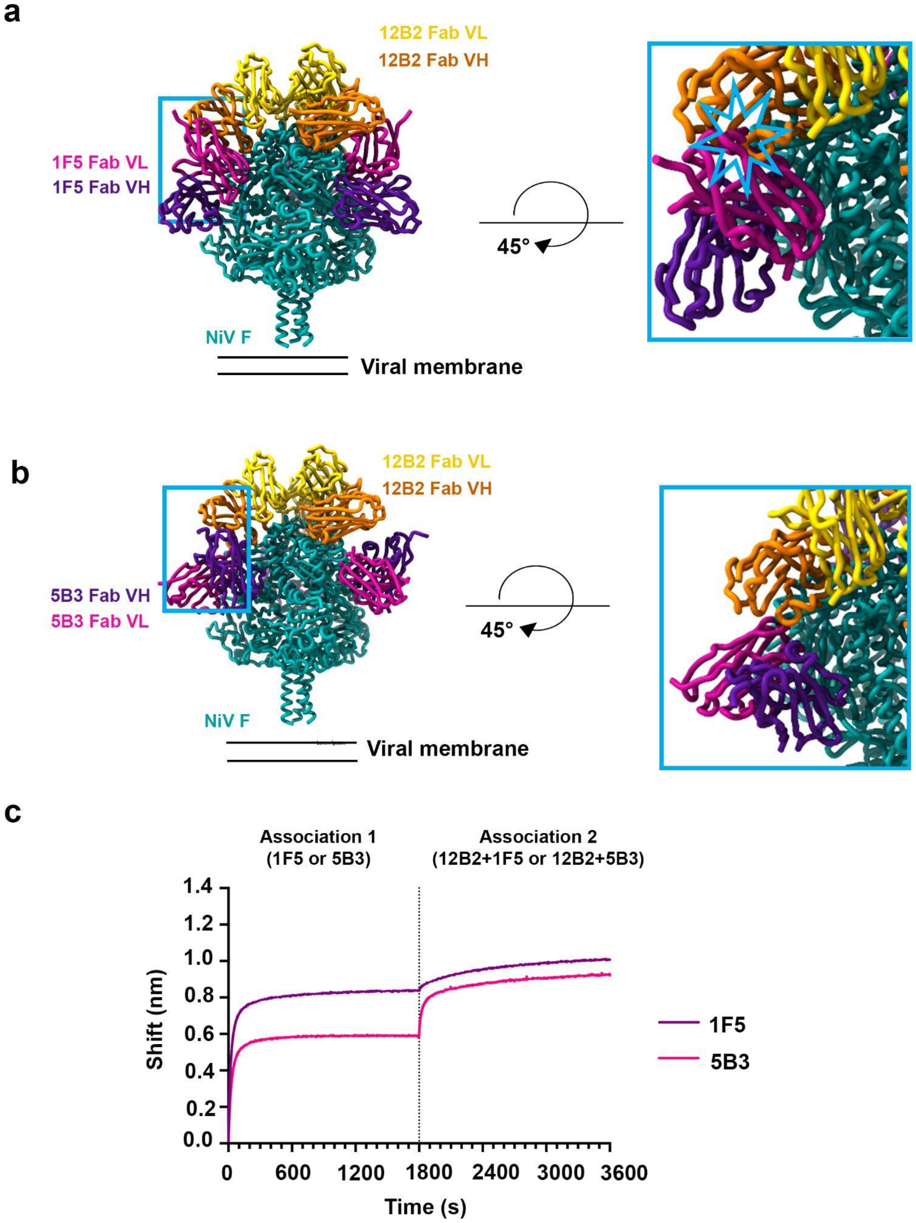

a, Superimposition of the NiV F/12B2 and HeV F/1F5 structures shows a potential clash between the framework regions of the two Fabs. **b,** Superimposition of the NiV F/12B2 and NiV F/5B3 structures (PDB: 6TYS) indicate that binding of the two Fabs is compatible without clash. **c,** Analysis of competitive binding of 12B2 Fab to pre-formed NiV F/1F5 or NiVF/5B3 complexes by BLI. Each amine-coupled NiV F biosensor probe was sequentially dipped in solution containing 600nM 1F5 or 5B3 Fab and then 1,200nM 12B2 Fab + 600nM 1F5 (purple) or 1,200nM 12B2 Fab + 600nM 5B3 Fab (pink).

Figure 3.2. Anti-F mAb cocktails prevent membrane fusion and neutralize HNVs. (Adapted from Dang et al., 2021.)

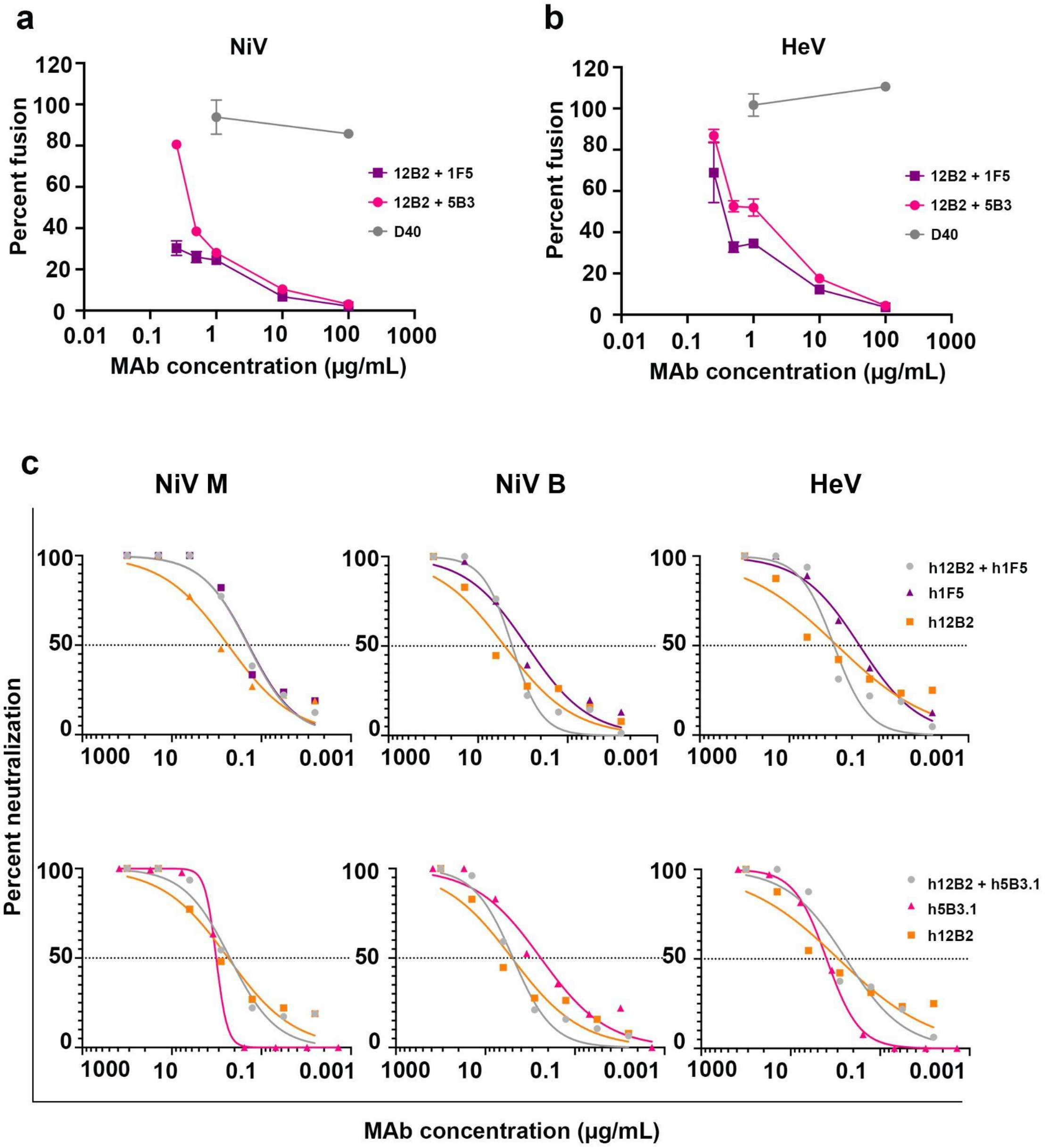

12B2/1F5 and 12B2/5B3 Ab cocktails inhibit membrane fusion mediated by NiV **(a)** and HeV **(b)** glycoproteins**.** D40 is an Ab against HIV gp-41 used as a negative control**. c,** Neutralization of authentic NiV-M, NiV-B, and HeV by h1F5, h5B3.1, h12B2, h1F5/h12B2 and h5B3.1/h12B2. Data for h12B2, h1F5, h12B2/h1F5 and h12B2/h5B3.1 shown are from one replicate of 2 independent experiments with independent virus preparations. Data for h5B3.1 are reproduced from Dang et al (Dang et al., 2019). EC50 values are reported in **Table S3.1** and **Chapter 2, Table S2.2**.

Figure S3.1. EM characterization of the negatively stained ternary complex of NiV F/12B2/5B3 and NiV F/12B2/1F5. (Adapted from Dang et al., 2021.)

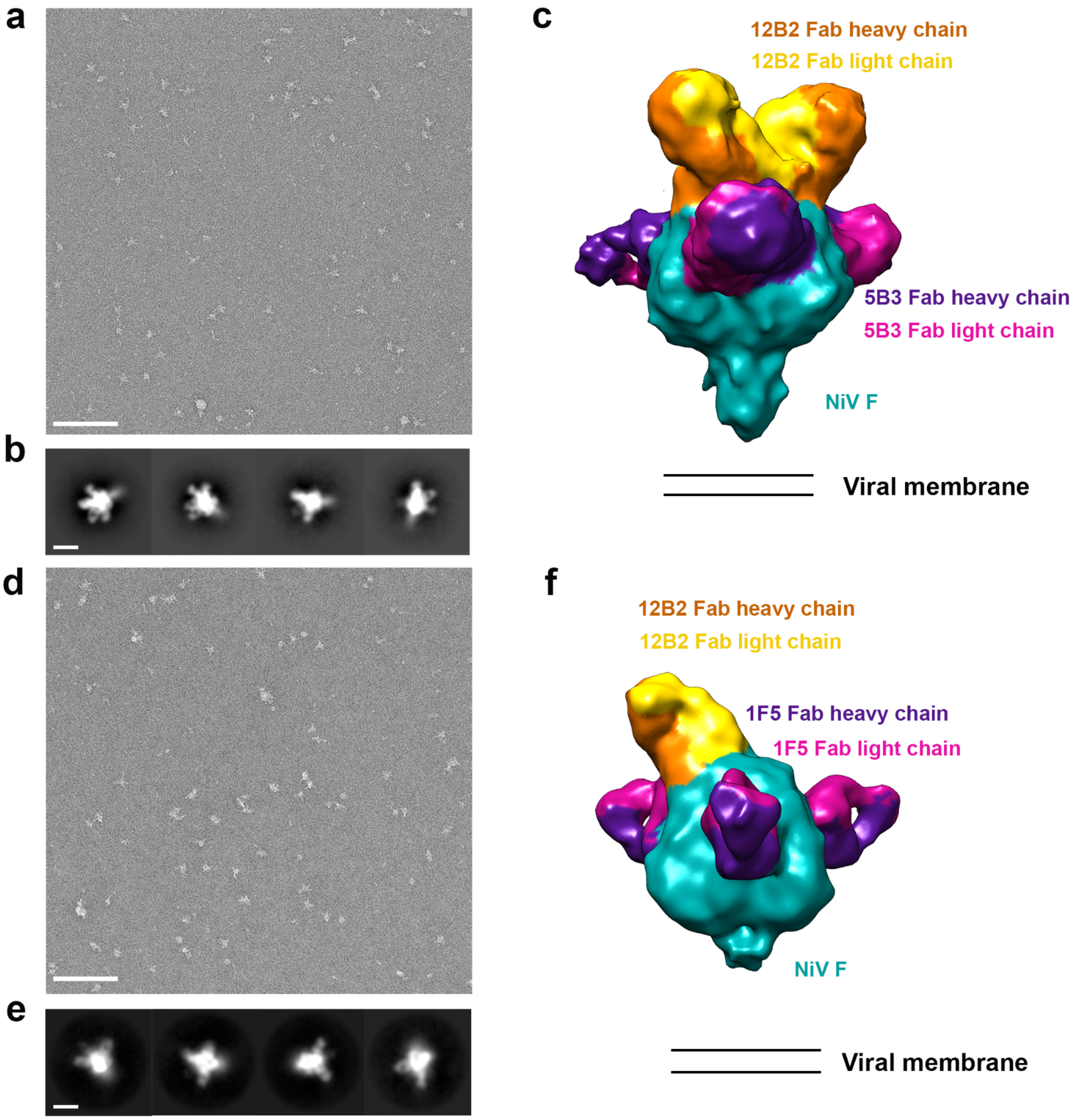

NiV F/12B2/5B3 (**a**) and NiV F/12B2/1F5 complex (**c**) from the corresponding negative staining dataset of NiV F incubated with excess of 12B2/1F5 Fabs or 12B2/5B3 Fabs (See **Materials & Methods**). Micrograph scale bar: 100 nm; 2D class average scale bar: 100Å. **b**,**d**, Three-dimensional reconstructions of the ternary complex of NiV F/12B2/5B3 (**b**) and NiV F/12B2/1F5 (**d**), representing a complex with the highest stoichiometry of Fabs:NiV F from the corresponding negative staining dataset.

Table S3.1 Half-maximal inhibitory concentrations (IC50) in ug/mL of humanized mAb cocktails of h12B2/h1F5 and h12B2/h5B3.1 against authentic HeV, NiV-M and NiV-B. Data were performed in duplicates. **(Adapted from Dang et al., 2021.)**

IC50 (ug/mL)	h12B2+h1F5	h12B2+h5B3.1
HeV	1.08	0.78
NiV M	0.277	0.59
NiV B	1.87	2.96

Chapter 4. A DNA-APTAMER TARGETING THE SPIKE PROTEIN FOR SARS-COV-2 DETECTION

Adapted from

Kacherovsky, Nataly, *et al*. "(Kacherovsky et al., 2021)." *Angewandte Chemie* (2021) .

Effective disease control of the COVID-19 pandemic, caused by severe acute respiratory syndrome coronavirus 2 (SARS-CoV-2) includes early detection of SARS-CoV-2 infections. Despite the deployment of COVID-19 vaccines, SARS-CoV-2 diagnostic tools remain critical for reducing virus spread. Furthermore, advances in rapid diagnostics enable better preparation for future pandemics.

COVID-19 diagnostic tests for active infections include molecular tests that detect viral RNA by nucleic acid amplification, and rapid antigen tests that detect viral proteins. While molecular tests are extremely sensitive and specific, rapid antigen tests are simpler to administer, provide point-of-care results, and are less expensive than molecular tests. Rapid antigen testing reduces COVID-19 prevalence by an estimated 70^% compared to unmitigated growth (Pavelka et al., 2021).

A major SARS-CoV-2 antigen detected by COVID-19 diagnostics is the spike (S) protein, a transmembrane glycoprotein that protrudes from the viral envelope (Walls, Park, et al., 2020; Wrapp et al., 2020). Antibodies against SARS-CoV-2 S protein have been isolated (McCallum et al., 2021; Piccoli et al., 2020; Pinto et al., 2020; Starr et al., 2021; Tortorici et al., 2020, 2021), and mRNA encoding the S protein is the basis of FDA-authorized mRNA vaccines (Baden et al., 2021; Jackson et al., 2020). SARS-CoV-2, a betacoronavirus, is closely related to SARS-CoV, which caused the 2002--2003 Severe Acute Respiratory Syndrome epidemic, and more distantly related to the MERS-CoV responsible for the 2012 Middle East Respiratory Syndrome outbreak, sharing 72% and 35% sequence similarity, respectively, with the S proteins of these viruses (Y.-Z. Zhang & Holmes, 2020). The SARS-CoV-2 S protein is composed of three identical monomers with two distinct subunits (Li, 2016; Tortorici & Veesler, 2019). Subunit 1 (S1) contains a receptor binding domain (RBD), which binds to human angiotensin-converting enzyme 2 (ACE2) and mediates host cell recognition, and an N-terminal domain (NTD) (Li, 2016; Walls, Park, et al., 2020). Recently, an antigenic supersite on the NTD was found to be frequently targeted by NTD-binding antibodies (McCallum et al., 2021), indicating that binders to this site may play a role in specific recognition of and immunity to SARS-CoV-2.

Aptamers are short nucleic acid sequences that bind target molecules. Aptamers not only achieve specific binding with affinities on par with antibodies, but also are cheaper and easier to produce (Bunka & Stockley, 2006; Zhou & Rossi, 2017; Q. Zhu et al., 2015). Novel aptamers are discovered through a library selection method coined systematic evolution of ligands by exponential enrichment (SELEX) (Ellington & Szostak, 1990; Gotrik et al., 2016; J. Liu et al., 2011; Robertson & Joyce, 1990; Sefah et al., 2010;

Tuerk & Gold, 1990). For detection of intact SARS-CoV-2 virus, aptamers that bind to accessible surface proteins such as S are needed.

In this study, we characterized two DNA aptamers that we previously identified that bind SARS-CoV-2 S protein with high affinity and specificity (Kacherovsky et al., 2021). We identified the aptamers' binding epitope as the NTD of the SARS-CoV-2 S protein by biolayer interferometry (BLI) and cryo-EM. We therefore designated these aptamers as SNAP1 and SNAP3 for SARS-CoV-2 spike protein N-terminal domain-binding aptamer 1 and 3. Currently, there are reports of aptamers binding to RBD of SARS-CoV-2 (Song et al., 2020; Sun et al., 2021a). To our knowledge, the aptamers reported here are the first to bind the NTD of SARS-CoV-2 S. In addition, we present the first cryo-EM map of SARS-CoV-2 S in complex with SNAP1. We then used SNAP1 to detect both S protein and UV-inactivated SARS-CoV-2 by lateral flow assay (LFA) and by ELISA.

4.1 BIOLAYER INTERFEROMETRY REVEALS THE BINDING SITE OF DNA APTAMERS ON SARS-COV-2 S PROTEIN

We used biolayer interferometry (BLI) to monitor protein association to immobilized aptamers. NS aptamer did not bind to SARS-CoV-2 S1 (**Figure S4.1**). We observed that SNAP1 and SNAP3 bind SARS-CoV-2 S1 and determined that the K_D of S1 binding to SNAP1 (39.32 ± 0.12 nM) was about 2-fold lower than that of SNAP3 (76.59 ± 0.45 nM) (**Figure 4.1 a,c, Table S4.1**). In addition, SNAP1 did not bind to SARS-CoV S1 or MERS-CoV S1 even at 200 nM protein (**Figure S4.1**). The negative control (NS) aptamer did not bind to SARS-CoV-2 S1 (**Figure S4.1**). Thus, both aptamers target SARS-CoV-2 S1 with high specificity and affinity.

We investigated whether SNAP1 and SNAP3 bind the receptor binding motif (RBM) by ACE2 competition studies but observed no change in binding constants between SARS-CoV-2 S1 and ACE2 in the presence of large excesses of aptamer by BLI (**Figure S4.2**). Therefore, SNAP1 and 3 do not bind at the receptor binding site on SARS-CoV-2 S1.

We then tested whether SNAP1 and SNAP3 interact with the SARS-CoV-2 S1 NTD. Using Streptavidin (SA) sensors where an aptamer (SNAP1, SNAP3, and NS) is immobilized, we measured the equilibrium constants of aptamers binding to S1 NTD (SNAP1 $K_D = 60.35 \pm 1.61$ nM, and SNAP3 $K_D = 53.25 \pm 2.49$ nM for NTD binding) (**Figure 4.2 b,d**), indicating that aptamer binding is localized to the NTD on SARS-CoV-2 S1 protein.

4.2 SNAP1 CONTACTS AN ANTIGENIC SUPERSITE ON SARS-COV-2 S N-TERMINAL DOMAIN

To further investigate the binding site of SNAPs on SARS-CoV-2 S NTD, we used cryo-EM to obtain a density map of SARS-CoV-2 S bound to SNAP1 in the presence of the S2M11 neutralizing antibody. Without S2M11, the S2 S/ SNAP1 complex suffered from preferred orientation in vitreous ice (**Figure S4.3**). The addition of S2M11 Fabs improved the specimen orientation distribution in vitreous ice and at the same time limited then conformational variability in the S protein receptor binding domain (Tortorici et al., 2020) (**Figure S4.4 a-d**), enabling us to use a C3 symmetry reconstruction. We obtained a cryo-EM map at an overall 3.3 Å resolution applying three-fold symmetry (**Figure 4.2, Figure S4.4**). The map was best resolved at the SARS-CoV-2 S core, whereas SNAP1 showed a high degree of flexibility outside of its binding contact region with SARS-CoV-2 S (**Figure S4.4 d)**. SNAP1 adopted an overall double-stranded helical shape, extending outwards from the SARS-CoV-2 S trimer. Our map unambiguously identifies that SNAP1 interacts exclusively with the NTD of SARS-CoV-2 S (**Figure 4.2**), in agreement with the results from BLI.

We obtained a 3.6 Å reconstruction for the region encompassing SNAP1 and part of SARS-CoV-2 S NTD (**Figure S4.4 d inset**) through focused 3D classification and local refinement (**Figure S4.4 e**). SNAP1 contacts residues 68-70, the NTD hairpin formed by residues 140-158, and a loop containing residues 253-257. These latter two regions are part of an antigenic supersite recognized by neutralizing NTD mAbs (McCallum et al., 2021; W. N. Voss et al., 2021). Comparison of the structures of NTD in complex with S2L28, S2M28 or S2X333 Fabs (PDB: 7LXZ, 7LY2, 7LXY) and with SNAP1 shows that these regions on SARS-CoV-2 S NTD are highly dynamic and adopt different conformations upon binding to different molecules (McCallum et al., 2021), (**Figure S4.5**). We likely discovered two NTD-binding aptamers because the NTD antigenic supersite is exposed and differs the most compared to SARS-CoV and MERS-CoV S1. Our SELEX runs and immune systems of multiple individuals selected for binders to the

NTD supersite, which highlights the importance of the NTD in immunity, vaccine design, and diagnostics applications.

4.3 APTAMER-BASED DETECTION OF SARS-COV-2

Aptamer truncation has, in some cases, improved binding affinity while reducing synthesis cost (Kacherovsky et al., 2019; Schmitz et al., 2021). Deleting 10 or 18 nucleotides (nt) of the constant region from each end of SNAP1 did not perturb predicted structures of the random region (**Figure S4.6 A**). The truncated SNAP1.66 (20 nt deletion, 66 nt total length) and SNAP1.50 (50 nt total length) aptamers have similar equilibrium binding constants as untruncated SNAP1 to both SARS-CoV-2 S1 and NTD (**Figure S4.6, Table S4.1).**

We applied SNAP1 in LFA and ELISA for aptamer-based detection of SARS-CoV-2 S protein and UV-inactivated SARS-CoV-2. Capitalizing on the trimeric nature of the S protein, we used SNAP1.50 as both the capture and detection agent in the HybriDetect LFA (**Figure 4.3 a**). We also performed a modified ELISA using SNAP1 to capture SARS-CoV-2 S protein (**Figure 4.3 b**). We were able to detect as low as 250pM of SARS-CoV-2 S with LFA (**Figure S4.7 a**) and 10pM S protein with ELISA (**Figure S4.7 b**). The LFA detected UV-inactivated SARS-CoV-2 virus but not lentivirus at 2.5×10^7 copies/mL1 (**Figure 4.3 c**). The ELISA detected UV-inactivated SARS-CoV-2 at concentrations as low as 5×10^5 copies/mL (**Figure 4.3 d**). The concentration of SARS-CoV-2 RNA detected in saliva and nasopharyngeal samples from COVID-19 positive patients by RT-qPCR in the first two weeks after onset of symptoms ranged from 10^4 to 10^{10} copies/mL (Wyllie et al., 2020). Therefore, SNAP1 can potentially detect SARS-CoV-2 in patient samples in a clinically relevant scenario. Potential approaches for further improving sensitivity in future diagnostic designs using SNAP1 include multimerizing the aptamer, including an amplification step, or using alternative detection modalities (Dauphin-Ducharme et al., 2019; Deng et al., 2021; Dinnes et al., 2020; Kuai et al., 2017; Singh et al., 2021).

4.4 CHAPTER DISCUSSION

Rapid response to any pandemic is key to containing the spread of diseases. DNA aptamers that bind pathogens with high affinity and specificity can be used in the development of biosensors, viral isolation/removal systems, and even therapeutics (Dunn et al., 2017; Zhou & Rossi, 2017) and can be uniquely discovered and manufactured in a relatively short time frame and at lower cost than antibodies. We previously designed a comprehensive protein SELEX strategy that after 12 rounds of selection yielded two aptamers specific for NTD of SARS-CoV-2 S. Currently, there are several reports of aptamers capable of binding to the SARS-CoV-2 virus (Schmitz et al., n.d.), including those specific for the nucleocapsid protein (Z. Chen et al., 2020; R. Liu et al., 2020; L. Zhang et al., 2020) and the RBD (Song et al., 2020; Sun et al., 2021b). To our knowledge, SNAP1 and SNAP3 reported here are the first aptamers to bind the NTD of SARS-CoV-2 S.

By testing the interactions of SNAP1 and 3 with different domains of SARS-CoV-2 S with BLI, we step-by-step narrowed down the binding location of SNAP1 as the N-terminal Domain (NTD) on the S protein. In order to further pinpoint the binding location of SNAP1 on the NTD, we used cryo-EM to obtain a 3.3Å resolution map of SNAP1 in complex with SARS-CoV-2 S protein. SNAP1 interacts exclusively with the NTD on an epitope recently identified as part of an antigenic supersite on SARS-CoV-2 S, which is recognized by several monoclonal antibodies isolated from convalescent patients (Tortorici et al., 2020; W. N. Voss et al., 2021). We observed that this antigenic supersite in the S protein is highly "adaptive", adopting different conformations when binding to different molecules such as monoclonal antibodies or aptamers.

The unique advantages that nucleic acid aptamers offer over protein antibodies, including longer shelf-life and more lenient storage requirements, make aptamers very suitable as recognition agents for diagnostic applications (Bunka & Stockley, 2006; Hernandez et al., 2015; Zhou & Rossi, 2017). Rapid antigen tests allow for rapid screening, but its sensitivity is lower than that of molecular diagnostics, such as RT-qPCR-based assays. Antigen tests with published independent testing have reported sensitivities of 30-50%, 11-45%, 70%, and 22-100% for the commercially available Respi-Strip, Biocredit, SD-Biosensor, and Roche antigen tests, respectively, compared to PCR (Cerutti et al., 2020; Krüttgen et al., 2021; Lambert-Niclot et al., 2020; Mak et al., 2020; Porte et al., 2020; Scohy et al., 2020). However, sensitivity levels can be greater than 80% for samples with very high viral loads, suggesting that rapid antigen testing can be used to identify highly infectious people (Kohmer et al., 2021). Due to the advantages of aptamers and rapid antigen tests, aptamer-based diagnosis of COVID-19 is under investigation, but no commercial tests have been developed (Rao, 2020).

We used SNAP1 as capture and detection agents in lateral flow assays and ELISAs, achieving a limit of detection of 5 nM and 10 pM SARS-CoV-2 S protein, respectively. Other novel SARS-CoV-2 antigen tests have similar limits of detection for SARS-CoV-2 protein (20 pM (L. Zhang et al., 2020), 15 pM (Quijano-Rubio et al., 2021)). However, SARS-CoV-2 antigen tests require even higher sensitivity for detection in patient samples. The concentration of SARS-CoV-2 RNA detected in saliva and nasopharyngeal samples from COVID-19 positive patients by RT-qPCR in the first two weeks after onset of symptoms ranged from 10^4 to 10^{10} copies/mL (Wyllie et al., 2020). Assuming a target of ~10^6 copies/mL sensitivity for a rapid antigen test and ~24 spike trimers per virus as determined by cryo-EM of intact SARS-CoV-2 virions (Ke et al., 2020), we estimate a goal of 40 fM detection limit. Potential approaches for improving sensitivity in future diagnostic designs using SNAP1 include multimerizing the aptamer to increase affinity, including an amplification step, or applying to electrochemical detection (Dauphin-Ducharme et al., 2019; Joung et al., 2020; Kuai et al., 2017; Singh et al., 2021).

In summary, we discovered novel SARS-CoV-2 spike-binding aptamers, characterized binding through real-time kinetics measurements and high resolution cryo-EM, and detected spike protein in lateral flow assays and ELISAs. Due to the relatively short time frame required for selection, aptamer SELEX can be a first response platform for creating diagnostic agents for emerging diseases.

4.5 MATERIALS & METHODS

4.5.1 *Buffers*

The composition of SELEX wash buffer (SELEX WB) is 4.5 g/L glucose, 0.1 g/L $CaCl_2$, 0.2 g/L KCl, 0.2 g/L KH_2PO_4, 0.1 g/L $MgCl_2$ $6H_2O$, 8 g/L NaCl, 2.1716 g/L Na_2HPO_4, and 5mM $MgCl_2$. 2.25g glucose (Sigma) and 2.5 mL 1M $MgCl_2$ is added to 497.5 mL Dulbecco's phosphate-buffered saline (DPBS) with $CaCl_2$ and $MgCl_2$ (Corning). The buffer is filtered through a 0.22μm sterile filter and stored at 4^{o}C.

For binding buffers, yeast tRNA (Invitrogen) (tRNA) and salmon sperm DNA (Invitrogen) DNA are added to a final concentration of 0.1 mg/mL. Additionally, MACS BSA 10% stock solution (Miltenyi Biotec) is added to 0.1-5% final concentration depending on the assay.

4.5.2 *Oligonucleotides*

All oligonucleotides were synthesized by Integrated DNA Technologies. All aptamer pools and aptamers were annealed before use in SELEX, binding, characterization, and other studies by diluting to 1 μM in SELEX WB (see buffers below), heating at 95^{o}C for 5 min, and snap-cooling on ice.

4.5.3 *Recombinant proteins*

SARS-CoV-2 S protein S1 domain (ACROBiosystems S1N-C5255), SARS-CoV-2 S protein monomer (ACROBiosystems SPN-C52H4), SARS-CoV-2 S protein trimer (ACROBiosystems SPN-C52H8), SARS-CoV-2 S protein S1 NTD (ACROBiosystems S1D-C52H6), SARS-CoV-2 S protein RBD (ACROBiosystems SPD-C5255) were purchased in lyophilized form and reconstituted, aliquoted, and stored according to manufacturer's recommendations.

SARS-CoV S protein S1 domain (ACROBiosystems S1N-S52H5) and MERS-CoV S protein S1 domain (Sino Biologics 40069-V08H) were purchased in lyophilized form and reconstituted, aliquoted, and stored according to manufacturer's recommendations.

SARS-CoV-2 S protein trimer "S-2P" was kindly provided by the Institute of Protein Design (IPD) at the University of Washington.

4.5.4 *Biolayer interferometry (BLI)*

Studies were performed with an Octet Red96 machine (Sartorius) at 25^{o}C and 1,000 rpm sample agitation. Pre-soaked streptavidin (SA) sensors were rinsed in 1% BSA, 0.1 mg/mL tRNA, 0.1 mg/mL SS DNA, 0.01% Tween-20 SELEX WB ("diluent") for 100s. Next, tips were loaded with 50 nM biotinylated aptamer until reaching a 0.5 nm signal threshold. Subsequently, tips were rinsed in diluent for 100s then baselined in diluent for another 100s. After association with protein of interest diluted to the desired concentration, sensor tips were returned to the baseline diluent well for dissociation. Data was analyzed with Octet Data Analysis 9.0 (Sartorius). Kinetic values were determined from a global fit of several curves generated from serial dilutions of the protein in a 1:1 binding model. The quality of the fit was calculated with R^2 and χ^2 values. See **Table S4.1** for the estimated kinetics parameters from these assays.

4.5.5 *Cryo-EM specimen preparation and data collection*

SARS-CoV-2 S protein (Acro Biosystems: SPN-C52H8) was reconstituted according to manufacturer's protocol and concentrated and buffer-exchanged into TBS pH 8.0 using a 30 kDa MWCO Amicon Ultra centrifugal filter (EMD Millipore). SARS-CoV-2 S protein was incubated with annealed SNAP1 with or without S2M11 Fab fragment at 1:3:2 molar ratio of Spike protomer:SNAP1:S2M11 Fab for 1 hour at room temperature. For the Spike:SNAP1 complex without S2M11, 3 µL of the complex at a concentration of 0.3 mg/mL SARS-CoV-2 S was applied onto glow-discharged C-flat, Cu 200 mesh, CF-1.2/1.3 grids. For the Spike:SNAP1:S2M11 complex, 3 µL of the complex at a concentration of 0.3 mg/mL SARS-CoV-2 S was mixed with 0.3 µL 1% octyl-glucoside (OG) immediately before application onto glow-discharged C-flat, Cu 200 mesh, CF-1.2/1.3 grids. The grids were plunge-frozen frozen in liquid ethane and cooled with liquid nitrogen, using an FEI MK4 Vitrobot with a 6.5 or 7 s blot time. The chamber was kept at 20°C and 100% humidity during the blotting process.

Data acquisition was carried out with the Leginon data collection software (Suloway et al., 2005) on a 200 kV FEI Glacios electron microscope and equipped with a Gatan BioQuantum energy filter (slit width of 20 eV) and a Gatan K2 Summit camera. The nominal magnification was 36,000x and the pixel size was 1.16 Å. The dose rate was adjusted to 8 counts/pixel/s and each movie was acquired in super-resolution mode fractionated in 50 frames of 200 ms each.

4.5.6 *Cryo-EM data processing*

For the dataset of Spike in complex with SNAP1 without S2M11, Warp [80] was used to perform motion correction, CTF estimation, particle picking and particle extraction. 25,758 extracted particles with a box size of 400 pixels were exported to cryoSPARC (Punjani et al., 2017) for reference-free 2D classification.

For the Spike:SNAP1:S2M11 dataset, movies were motion-corrected using Warp and exported to cryoSPARC for CTF estimation using CTFFIND4. A set of manually picked particles were used to generate 2D class averages that were subsequently low pass-filtered to 20 Å for Template Picker in cryoSPARC on the whole dataset. All particles from the whole dataset were extracted with a box size of 400 pixels and underwent 2 rounds of reference-free 2D classification in cryoSPARC. 41,071 particles were selected for *ab initio* reconstruction (no symmetry) and non-uniform refinement (NUR) (C3 symmetry) (Punjani et al., 2020), followed by CTF refinement and another round of NUR in cryoSPARC. The particles were exported to RELION v3.0 (Zivanov et al., 2018) for Bayesian polishing and then uploaded to cryoSPARC for NUR. To improve the density around the SARS-CoV-2 S NTD/SNAP1 interface, the particles were C3-symmetryexpanded and subjected to focus 3D classification without refining angles and shifts using a soft mask encompassing SNAP1 and part of the NTD in RELION. 55,369 particles belonging to the best-resolved classes with the aptamer bound were selected and underwent local refinement in cryoSPARC. Local resolution estimation, local filtering and map sharpening were performed in cryoSPARC. Reported resolutions are based on the gold-standard Fourier shell correlation (GS-FSC) at 0.143 criterion and FSC curve was corrected for the effects of soft masking by high-resolution noise substitution (S. Chen et al., 2013). See **Fig. S4.4 c** for detailed data processing workflow.

4.5.7 *Lateral flow assay (HybriDetect)*

HybriDetect universal lateral flow dipsticks (Milenia Biotec) were used in combination with biotinylated and FITC labeled SNAP1 aptamers. 100µL of 50 nM of both aptamers were incubated with 50 nM of S protein variants in binding buffer or 50% saliva solution for 20 min at room temperature. Then, the lateral flow strip is dipped in the solution and results are interpreted in 15 minutes.

4.5.8 *ELISA*

Wells of a white streptavidin-coated 96-well plate (Thermo Fisher Scientific) were washed and blotted three times with SELEX WB then incubated with 50 nM biotinylated SNAP1 aptamer at 4^{o}C for 30 min. After three washes with wash buffer (0.1% Tween-20 2% BSA SELEX), wells were incubated with blocking buffer (5% BSA, 1:100 biotin blocking solution (Vector Laboratories), 0.1 mg/mL tRNA, 0.1 mg/mL SS DNA, 0.1% Tween-20 SELEX WB) for 1.5 hr at room temperature. Subsequently, the wells were incubated with samples in the binding buffer for 30 min at room temperature.Wells were then washed four times before incubation with anti-SARS-CoV-2 antibody with HRP (Novus Biologicals cat. no. NBP2-90980H). Lastly, wells were washed six times. All steps use 100 µL of solution, except washing (200 µL of solution.) For wash steps, the plate is flicked over a sink then blotted dry. Ice-cold ELISA Femto Substrate (Thermo Fisher Scientific) was added and the plate luminescence was immediately measured by Infinite 200 PRO plate reader (Tecan) with 250 nm integration time and automatic attenuation. Measurements were normalized to wells without samples and plotted on logarithmic scale.

4.6 FIGURES & TABLES

Figure 4.1. SNAP1 and SNAP3 aptamers bind to the NTD of SARS-CoV-2 S protein. (Adapted from Kacherovsky et al., 2021.)

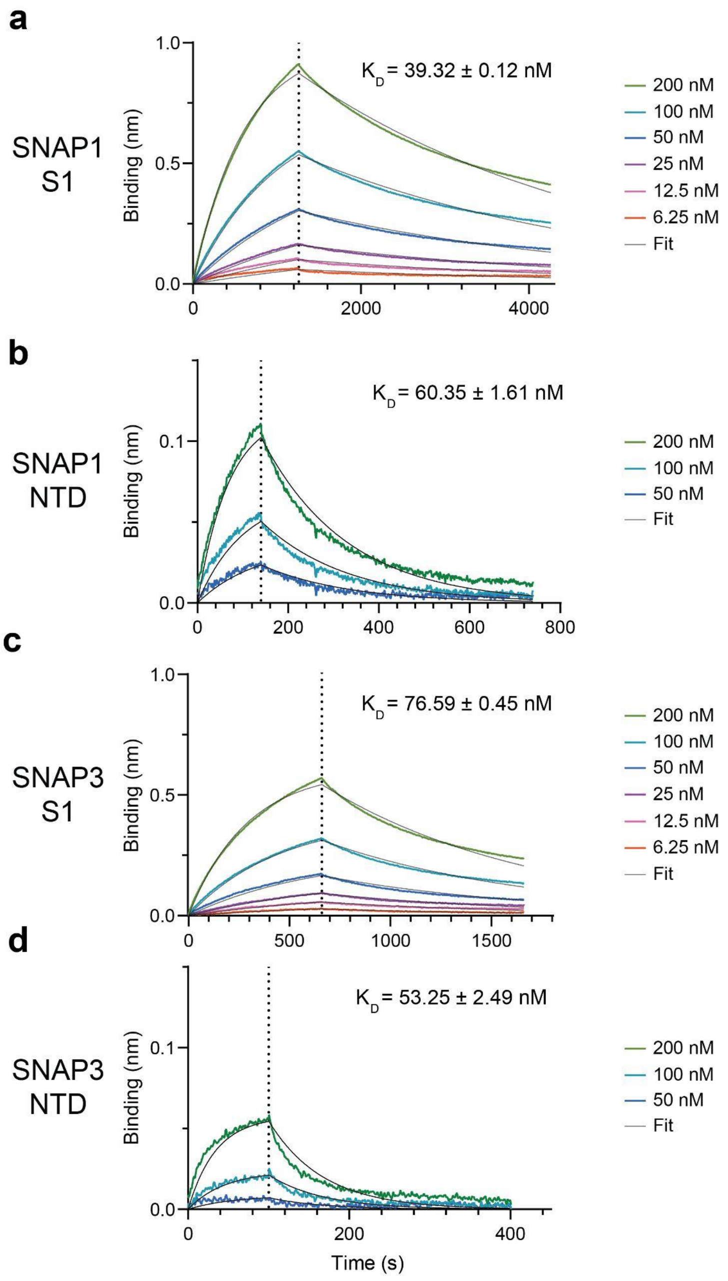

Kinetics and binding equilibrium constants were measured by BLI. Biotinylated SNAP1 or SNAP3 loaded on streptavidin (SA) biosensors was associated with SARS-CoV-2 S1 (**a**,**c**) or NTD (**b**,**d**). Dotted lines indicate switch from analyte association to dissociation. KD values (mean±s.d., n=5--6) were determined from a global fit of the kinetic data for a 1:1 binding model.

Figure 4.2. Two views of the S/SNAP1/S2M11 complex cryo-EM unsharpened map. (Adapted from Kacherovsky et al., 2021.)

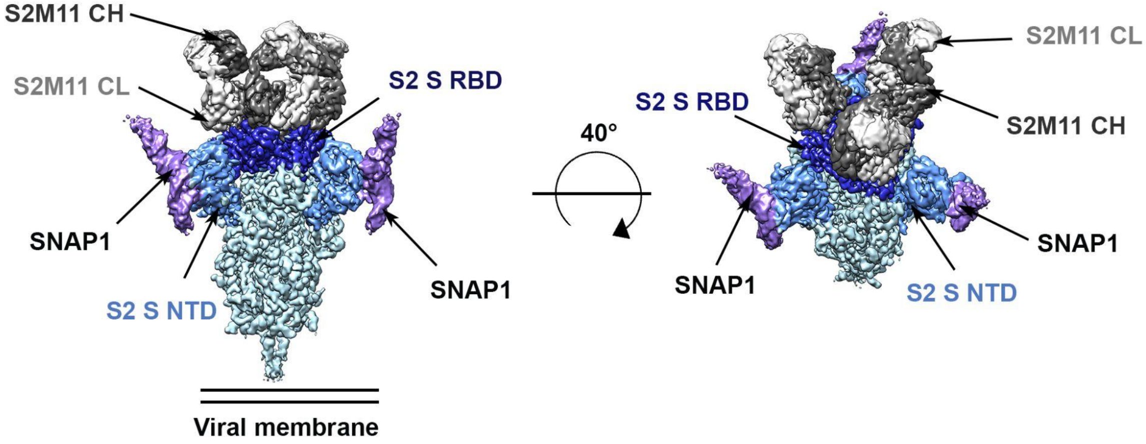

SNAP1: purple, NTD: light blue, RBD: dark blue, rest of SARS-CoV-2 S: cyan, S2M11 CH (Fab fragment heavy chain): dark gray, S2M11 CL (Fab fragment light chain): light gray.

Figure 4.3. Aptamer-based detection of UV-inactivated SARS-CoV-2 virus. (Adapted from Kacherovsky et al., 2021.)

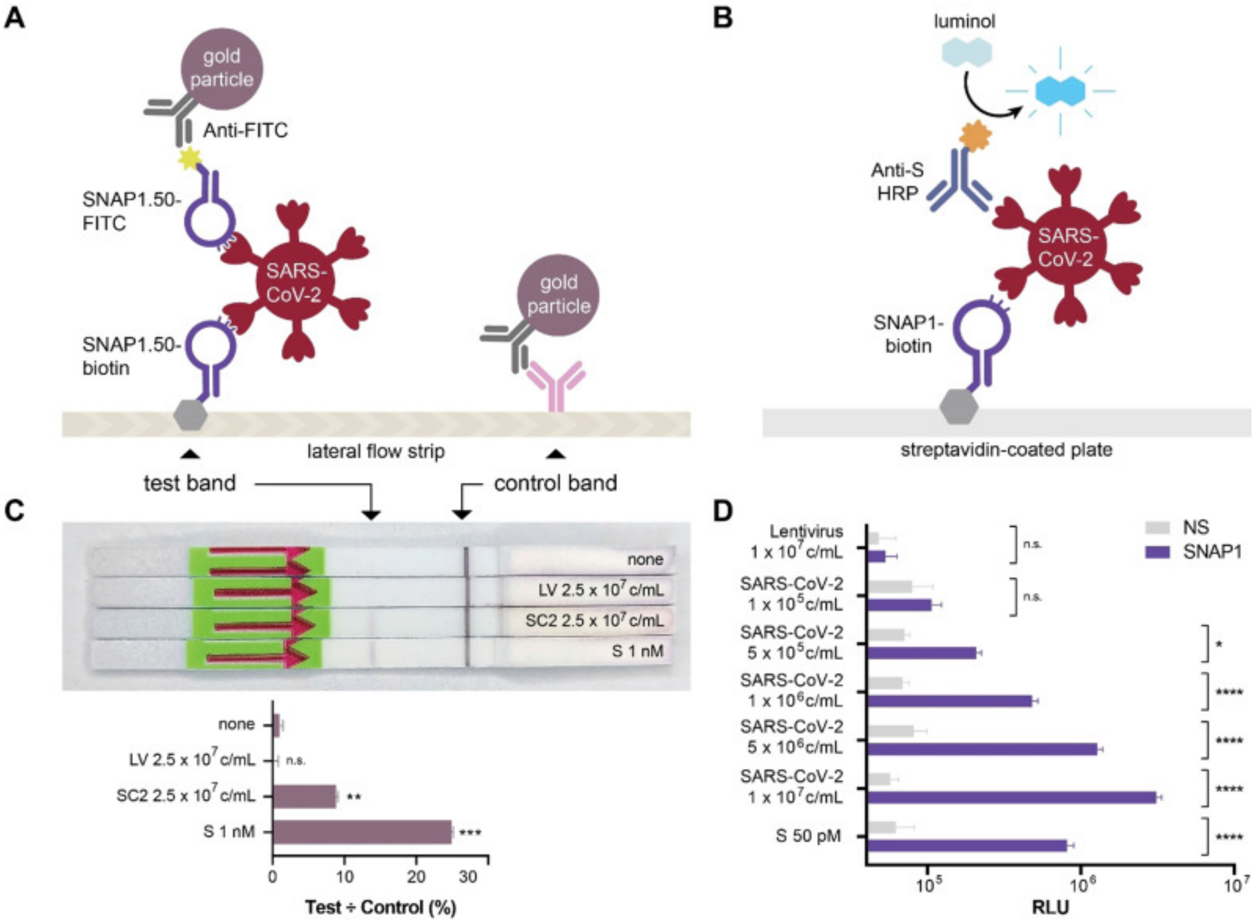

a) Schematic of HybriDetect LFA. **b**) Schematic of aptamer-antibody sandwich ELISA. **c**, **d**) c/m = copies per mL of virus. **c**) HybriDetect LFA strips were dipped in solutions of S protein (S), control lentivirus (LV), or UV-inactivated SARS-CoV-2 virus (SC2) incubated with SNAP1.50. Top: representative image of developed strips. Bottom: quantification of band intensity. Bar graph shows the mean and standard deviation of three replicates. Statistical comparison of LV, SC2, and S to none was determined by one-way ANOVA with Bonferroni correction, *** denotes $p<0.001$, ** denotes $p<0.01$, and n.s. denotes no significance. **d**) ELISA using NS-biotin or SNAP1-biotin as capture agents to detect UV-inactivated SARS-CoV-2 using anti-S HRP antibody for detection. Bar graph shows the mean and standard deviation of three replicates. Statistical comparison of NS to SNAP1 was determined by two-way ANOVA with Fisher's LSD test, **** denotes $p<0.0001$, * denotes $p<0.05$, and n.s. denotes no significance.

Figure S4.1. Aptamers SNAP1 and SNAP3 do not bind to SARS-CoV S1 or MERS-CoV S1. (Adapted from Kacherovsky et al., 2021.)

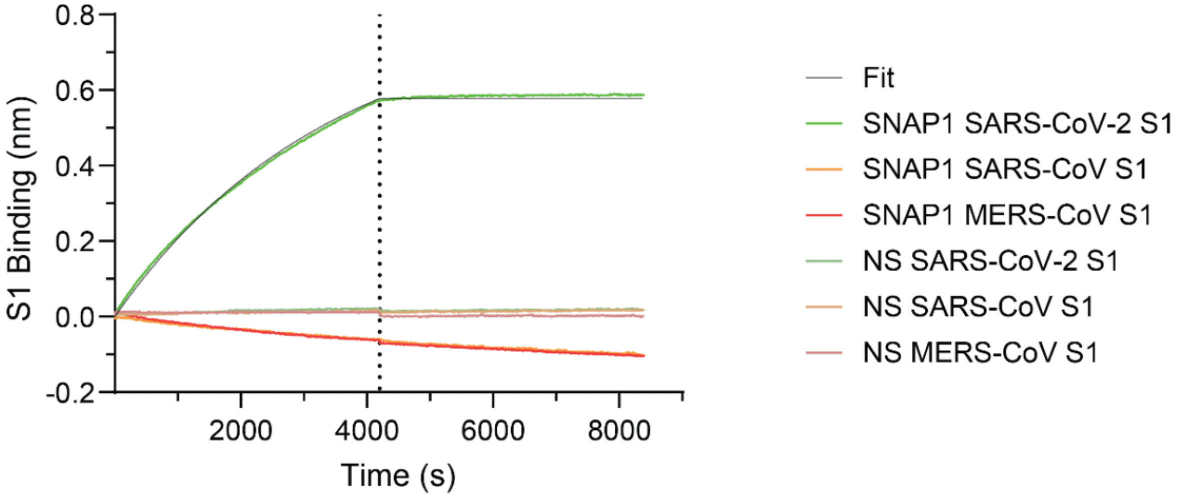

Kinetic parameters were measured through BLI. Biotinylated NS or SNAP1 aptamer were loaded on streptavidin biosensors, associated with 200 nM S1 of MERS-CoV (red), SARS-CoV (orange), or SARS-CoV-2 (light green) between 0-4200s, and then dissociation occurred between 4,200 - 8,400s.

Figure S4.2. Aptamers SNAP1 and SNAP3 do not compete with ACE2 for binding to SARS CoV-2 S1. (Adapted from Kacherovsky et al., 2021.)

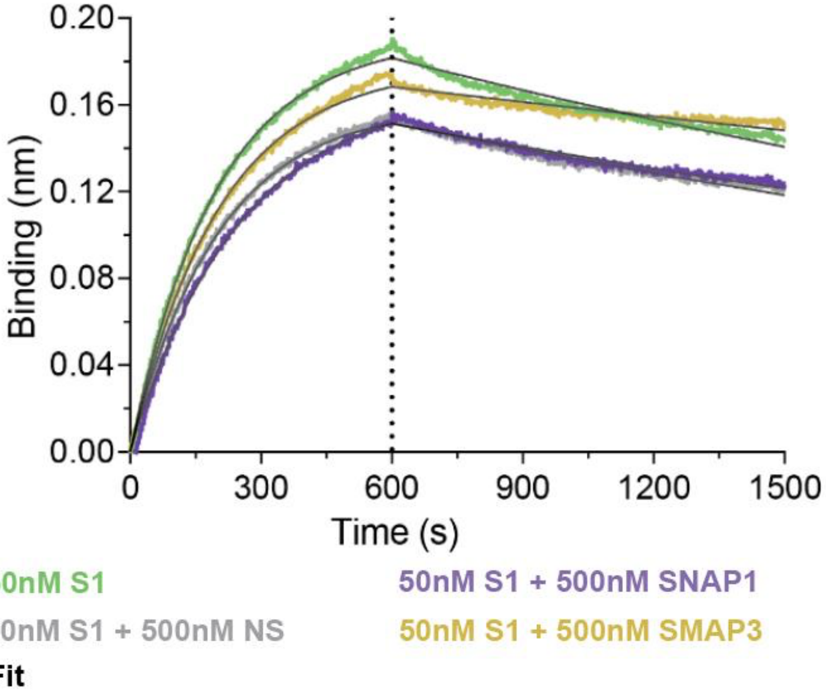

BLI experiment was conducted by loading His-tagged ACE2 onto Ni-NTA biosensors and testing association with 50 nM SARS-CoV-2 S1 alone and in the presence of 500 nM NS, SNAP1, or SNAP3 aptamer. Dotted line indicates switch from aptamer association (0-600s) to dissociation (600-1500s). Black lines indicate global fit of the kinetic data for a 1:1 binding model.

Figure S4.3. SARS-CoV-2 S/SNAP1 shows a preferred orientation for the top view in vitreous ice. (Adapted from Kacherovsky et al., 2021.)

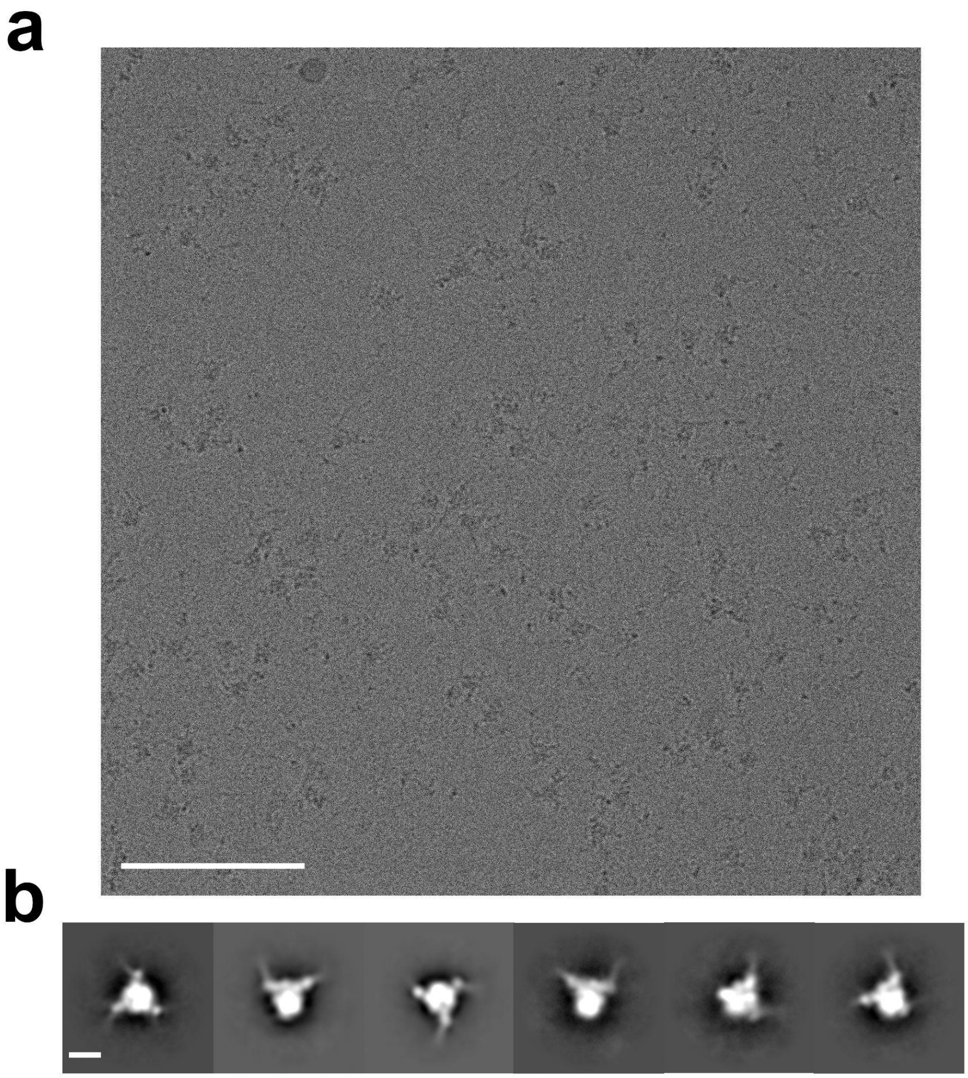

a) Representative micrograph. Scale bar, 100 nm. **b**) Reference-free 2D class averages. Scale bar, 100 Å.

Figure S4.4. Cryo-EM characterization of the SNAP1/S/S2M11 complex. (Adapted from Kacherovsky et al., 2021.)

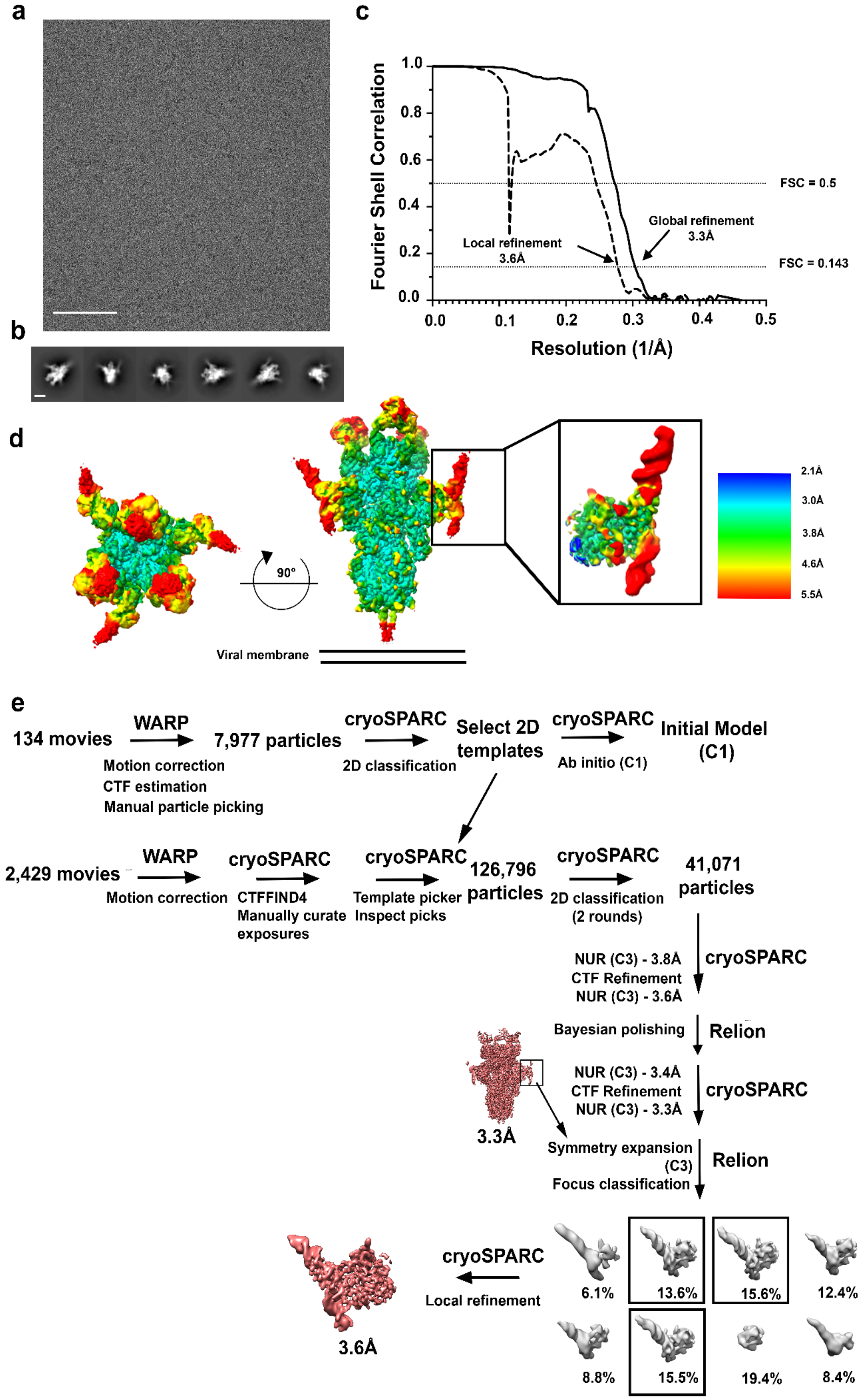

a) Representative micrograph. Scale bar, 100 nm. **b**) Reference-free 2D class averages. Scale bar, 100 Å. **c**) Gold-standard Fourier shell correlation (GSFSC) curves of the global map and the locally refined map of the NTD-bound aptamer. **d**) Unsharpened maps colored by local resolution in cryoSPARC of the SNAP1/S/S2M11 complex, as well as the locally-filtered map of the locally refined reconstruction of NTD and SNAP1 (inset). **e**) Cryo-EM data processing flow chart. Selected groups of particles at a given step are boxed.

Figure S4.5. SARS-CoV-2 NTD antigenic supersite adopts different conformation upon binding to different molecules.

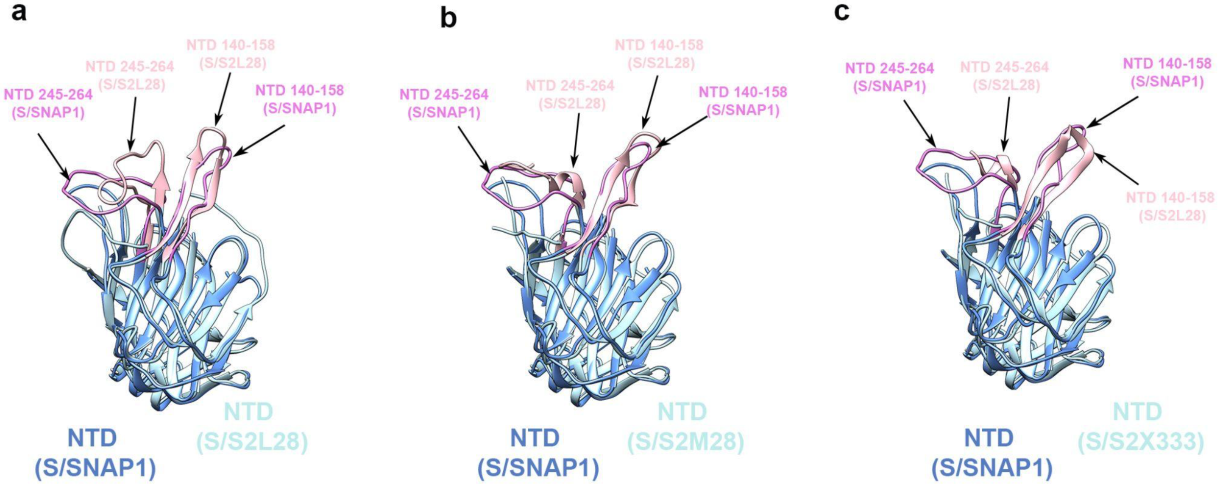

Superimposition of the NTD from S2 S/SNAP1/S2M11 structure (this study) on the NTD from (**a**) S2 S/ S2L28 (PDB: 7LXZ), (**b**) S2 S/S2M28 (PDB: 7LY2), and (**c**) S2 S/S2X333 (PDB: 7LXY) (McCallum et al., 2021).

Figure S4.6. Truncations of SNAP1 have similar binding affinities as whole SNAP1. (Adapted from Kacherovsky et al., 2021.)

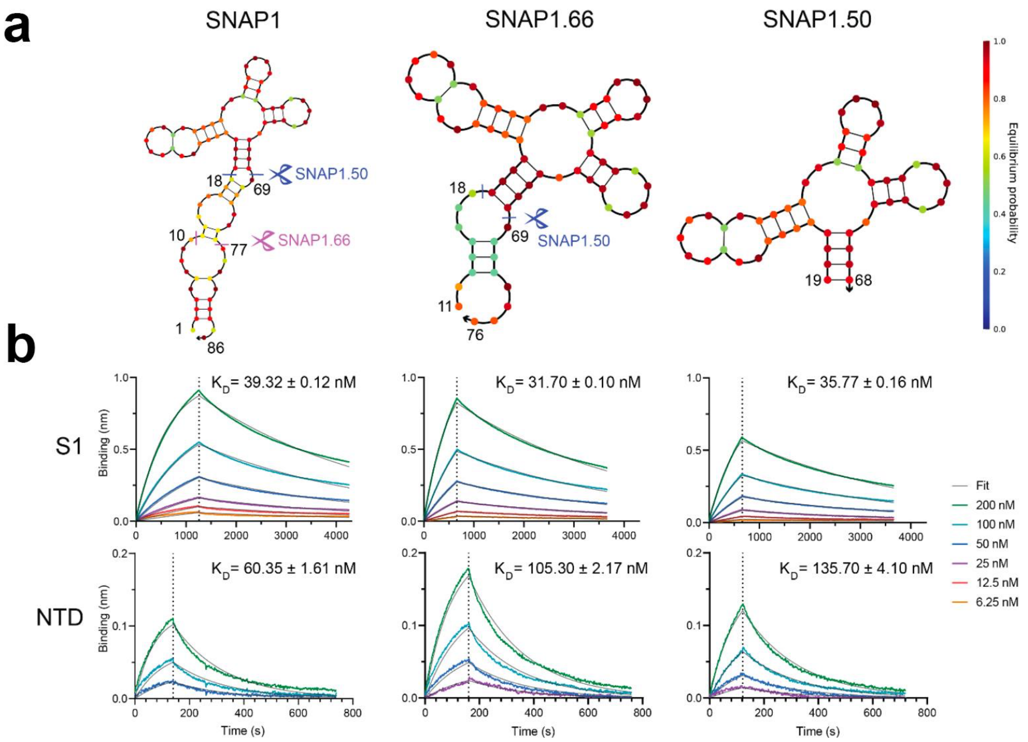

a) Secondary structure was predicted using NUPACK (http://www.nupack.org/) for SNAP1 (left), SNAP1.66 (center), and SNAP1.50 (right) with the following conditions: 4oC, 0.137 M Na+, 0.0055 M Mg++. Arrows represent the 3' end of the aptamer. Nucleotides are color-coded by their equilibrium probability (see legend on right). **b**)Kinetic and binding equilibrium constants were measured by BLI. Biotinylated SNAP1 (left), SNAP1.66 (center) or SNAP1.50 (right) was loaded on streptavidin biosensors and associated with SARS-CoV-2 S1 domain (upper row) or NTD (lower row). Each graph contains different concentrations of proteins as denoted in the legend (right). Dotted lines indicate switch from analyte association to dissociation. KD values (mean±s.d., n=6) were determined from a global fit (dark gray line) of the kinetic data at various concentrations of proteins for a 1:1 binding model.

Figure S4.7. Aptamer-based detection of SARS-CoV-2 S protein. (Adapted from Kacherovsky et al., 2021.)

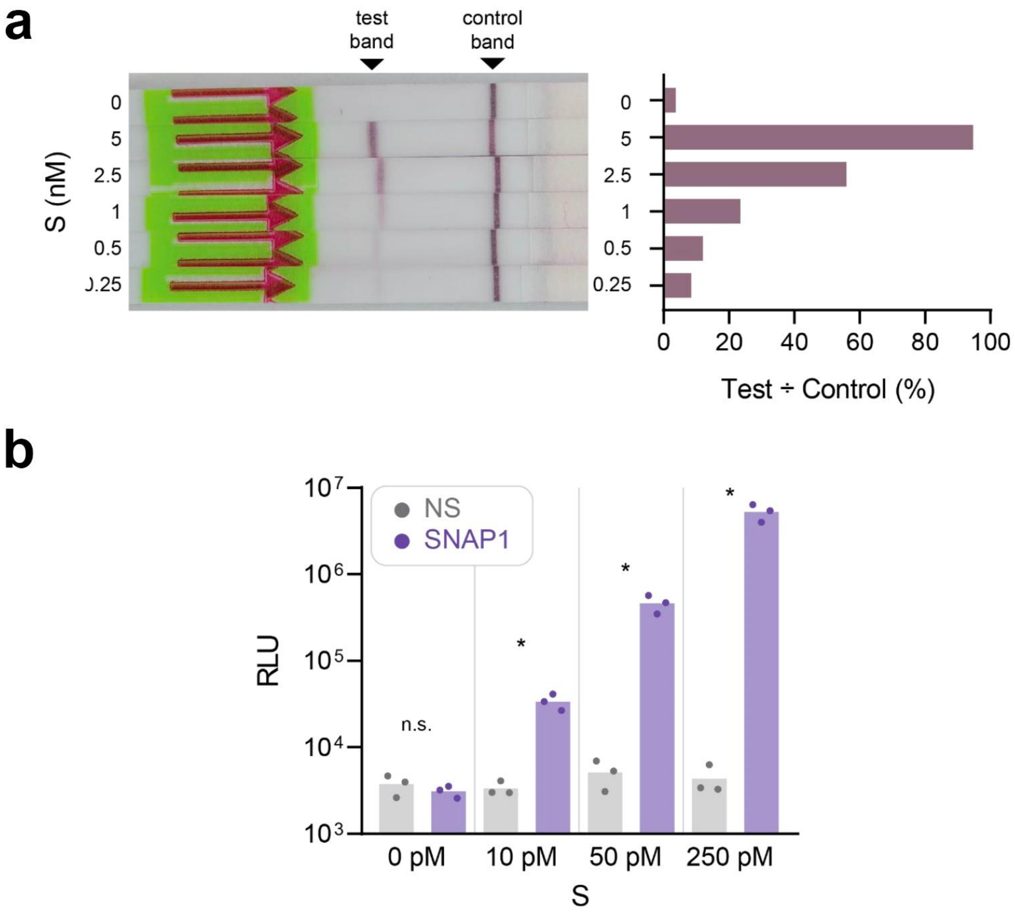

a) HybriDetect LFA strips were dipped in solutions of S protein incubated with SNAP1.50. Left: image of developed HybriDetect LFA test strips. Right: quantification of band intensity. **b**) ELISA assay using NS-biotin or SNAP1-biotin as capture agents to detect various concentrations of SARS-CoV-2 using anti-S HRP antibody for detection. Bar graph shows the mean (bar) of three replicates. Statistical comparison of NS to SNAP1 was determined by two-way ANOVA,* denotes $p < 0.05$ and n.s. denotes no significance.

Table S4.1. SNAP1 and SNAP3 binding kinetic values and fit parameters. (Adapted from Kacherovsky et al., 2021.)

Aptamer	SARS-CoV-2 protein	k on (1/nM.s.10^-5)	k off (1/s.10^-5)	KD (nM)	χ2	R^2
SNAP1	S1-His	0.71 ± 0.00	27.88 ± 0.03	39.32 ± 0.12	2.58	0.9978
SNAP1	NTD-His	8.64 ± 0.22	52.13 ± 3.20	60.35 ± 1.61	0.03	0.974
SNAP1	S	19.53 ± 0.01	-	-	5.66	0.9981
SNAP1	S-2P	0.16 ± 0.00	-	-	5.42	0.9914
SNAP3	S1-His	1.26 ± 0.01	96.77 ± 0.17	76.59 ± 0.45	0.53	0.9969
SNAP3	NTD-His	24.44 ± 1.09	1302.00 ± 18.00	53.25 ± 2.49	0.01	0.9509
SNAP1.66	S1-His	0.90 ± 0.00	28.53 ± 0.02	31.70 ± 0.10	0.86	0.999
SNAP1.66	NTD-His	5.01 ± 0.10	527.20 ± 1.90	105.30 ±. 2.17	0.05	0.9888
SNAP1.50	S1-His	0.80 ± 0.00	28.63 ± 0.02	35.77 ± 0.16	0.57	0.9986
SNAP1.50	NTD-His	3.74 ± 0.11	508.10 ± 1.70	135.70 ± 4.10	0.18	0.9903

CONCLUDING REMARKS

The general theme of my dissertation is to utilize structural information about viral glycoproteins to combat viral outbreaks by enabling strategies either for detection/ surveillance or for therapeutics. Glycoproteins are difficult subjects for crystallography, one of the major structural biology techniques, as the glycans are mobile and thus not conducive to crystal formation. In most cases, the glycans must be trimmed or removed with glycosidases before crystallization set-up. However, for several proteins, especially viral glycoproteins, removing glycans is not feasible as they are crucial to the proper folding and functions of the proteins (Helenius and Aebi 2004). Cryo-EM emerges as a powerful structural biology technique and is much more amenable to glycosylated proteins. Cryo-EM plays a huge role in my dissertation, enabling the visualization of HNV and SARS-CoV-2 fusion proteins in a more native state than being deglycosylated.

The Spike-Aptamer project is a collaboration with Suzie Pun Lab at UW Bioengineering. One of the most exciting moments of this project was when we overcame the preferred orientation issue with Spike/SNAP1 complex with the help from a monoclonal antibody called S2M11 and a surfactant called OG (abbreviation for “octylglucoside”). S2M11 is a potent neutralizing antibody against SARS-CoV-2 isolated and characterized by our lab in collaboration with Vir Biotechnology (Tortorici et al., 2020). The cryo-EM structure of S2M11 in complex with SARS-CoV-2 S reveals that this antibody keeps the flexible receptor-binding domain (RBD) of the Spike in a “closed” state, which probably helps prevents the Spike protein from adopting its preferred orientation for the top view in vitreous ice. This is an example of how monoclonal antibodies can serve as a useful structural biology tool. The result of the Spike-Aptamer project to me offered even more questions to investigate. Can we identify aptamers that distinguish Spike proteins from different SARS-CoV-2 strains, or on the other hand, aptamers that broadly recognize Spike proteins from several different strains? Can we identify aptamers recognizing glycoproteins from other viruses? Do glycans, which are normally negatively charged, interfere with aptamer recognition given the aptamers' phosphate backbones?

As for the Henipavirus project, at the beginning of my thesis study on HNVs in the Veesler lab 5 years ago, m102.4 was the only mAb that was extensively characterized biophysically and structurally, and shown to have therapeutic efficacy in a ferret model of HNV infection (Xu et al., 2013; Z. Zhu et al., 2008). Several neutralizing anti-HNV-G mAbs have also been reported but there was no information on the epitopes of these mAbs or their protection efficacy against HNVs (Q. Liu et al., 2013). During this time, there have been two additional incidents of HNVs: 08/2018 and 09/2021, both took place in Kerala, India (https://www.who.int/emergencies/disease-outbreak-news/). In both cases the virus was successfully contained and neither incident persisted for a long time. However, the survival rate was dismal. In the 08/2018 NiV outbreak, 17 out of 19 patients died. In the 09/2021 NiV outbreak, the single patient, a 12-year-old child, passed away after a week since he was first hospitalized. In addition, a new variant of Hendra virus, termed HeVvar or HeV-g2, was recently isolated in South Australia independently from two samples: one from a horse displaying canonical symptoms of HNV diseases (Annand et al., 2021) and the other from an Australian flying fox (J. Wang et al., 2021). Taken together, there is an obvious need for more prophylactic or therapeutic preparedness for the next HNV outbreak. Examples include: more neutralizing antibodies, and tools for a continuous surveillance of these dangerous viruses within domestic animals and bat populations.

5B3 was one of the mAbs that came from a mouse immunization campaign with a soluble NiV F protein stabilized with a C-terminal GCNt trimerization domain. This campaign was led by our collaborator, Christopher Broder and his team at Uniformed Services University (Chan et al., 2012). Prior to this, there had not been any work on anti-HNV F glycoprotein. In collaboration with the Broder lab and scientists from Galveston National Lab, UTMB, Mayo Clinic, and Mapp Biopharmaceutical, we thoroughly examined 5B3 and two other mAbs from this immunization campaign, 1F5 and 12B2: we delineated the atomic interaction networks of each of these mAbs with the HNV F protein, humanized these murine mAbs, showed that they had excellent binding profiles to HNV F and that these mAbs can neutralize authentic HNV virions. Our collaborators from Galveston took one step further to demonstrate that humanized 5B3 (h5B3.1) protects ferrets in a stringent therapeutics settings up to 5 days post infection with HNVs at lethal doses (Mire et al., 2020), indicating that h5B3.1 has a favorable profile and can potentially be used for individuals exposed to HNVs.

I confronted several technical hurdles while working on HNV F proteins, which ultimately turn out to inspire new and exciting directions for the HNV project. The first challenge I encountered was how to stabilize HNV F proteins, as they are, like other class I viral fusion proteins, metastable. I tested two disulfide pairs, N97C/A119C or Y96C/G131C, described by (Wong et al., 2016), and observed that they successfully stabilized both HeV F and NiV F in the prefusion conformation. We can now use HeV and NiV F mutants with both disulfides introduced (called “2DS”, for “two disulfides”) to immunize mice equipped with human antibody-making machineries (for example: Kymouse from KyMab (E.-C. Lee et al., 2014)), to readily elicit and isolate neutralizing human mAbs against HNV F. In another application, we can imagine using HNV F 2DS to interrogate the antibody profiles of bats harboring HNVs. Given their stability, these 2DS constructs are also promising vaccine candidates.

The second major hurdle was, once again, the preferred orientation problem in cryo-EM. The NiV F/ 5B3 complex’s preferred orientation was recalcitrant to many methods including surfactants, tilted-stage data collection and ultra-fast sample plunging with an equipment used to be called Spotiton (Dandey et al., 2018; Jain et al., 2012), now known as Chameleon (SPT Lab tech (Darrow et al., 2019)). At this point in time, around 2018, thin carbon used to have a bad rap in the field for deteriorating high-resolution data. We vindicated thin-carbon from this bad notion by obtaining the NiV F/ 5B3 cryo-EM map at 3.5 Å, HeV F/1F5 at 2.8 Å and NiV F/12B2 at 2.9 Å, all with data collected on grids coated with thin carbon.

The HNV project is still ongoing with many remaining questions regarding the HNV F and G proteins. Can we extend the 2DS mutations to F proteins in other viruses in the

HNV genus or HNV-related viruses such as MojV, CedV, GhV or the recently identified Daeryong virus (DAR-V) and Gamak virus (GAK-V) (S.-H. Lee et al., 2021), or even to more distant paramyxoviruses such as Measles virus or Canine distempervirus? Our atomic models of F in complex with mAbs 5B3, 1F5 and 12B2 reveal the vulnerable spots on F. Can we target these spots with non-mAb molecules, for example: mini-binders, i.e: *in silico* designed small proteins that neutralize viruses such as SARS-CoV-2 (Cao et al., 2020)? In some cases, mAbs that trigger fusion proteins to transition from prefusion to postfusion have been isolated, for example, in SARS-CoV (Walls, Xiong, et al., 2020) or SARS-CoV-2 (Lempp et al., 2021; Park et al., 2021). mAbs that trigger G or F to induce membrane fusion would illuminate the molecular basis of how G and F coordinate to induce cell entry. Other outstanding questions are: why are HNVs so lethal in humans and other mammals but not in bats? What aspects of bat immunity provide protection against HNVs? How potent are the antibody responses against HNVs of bats immunized with F or G immunogens?

In addition to the work in our lab, there have since been many more studies on HNV-G mAbs (Dong et al., 2020; Doyle et al., 2021), HNV-F mAbs (Avanzato et al., 2019), and also other potential subunit vaccine candidates for HNVs (Loomis et al., 2020). Overall, advances in cryo-EM, protein engineering and antibody identification and isolation techniques will all together provide potential powerful countermeasures against HNVs and pathogenic viruses in general.

BIBLIOGRAPHY

Agirre, Jon, Javier Iglesias-Fernández, Carme Rovira, Gideon J. Davies, Keith S. Wilson, and Kevin D. Cowtan. 2015. “Privateer: Software for the Conformational Validation of Carbohydrate Structures.” *Nature Structural & Molecular Biology* 22 (11): 833–34.

Aguilar, Hector C., and Ronald M. Iorio. 2012. “Henipavirus Membrane Fusion and Viral Entry.” *Current Topics in Microbiology and Immunology* 359: 79–94.

Aguilar, Hector C., Kenneth A. Matreyek, Claire Marie Filone, Sara T. Hashimi, Ernest L. Levroney, Oscar A. Negrete, Andrea Bertolotti-Ciarlet, et al. 2006. “N-Glycans on Nipah Virus Fusion Protein Protect against Neutralization but Reduce Membrane Fusion and Viral Entry.” *Journal of Virology* 80 (10): 4878–89.

Alfego, David, Adam Sullivan, Brian Poirier, Jonathan Williams, Dorothy Adcock, and Stanley Letovsky. 2021. “A Population-Based Analysis of the Longevity of SARS-CoV-2 Antibody Seropositivity in the United States.” *EClinicalMedicine* 36 (June): 100902.

Amaya, Moushimi, and Christopher C. Broder. 2020. “Vaccines to Emerging Viruses: Nipah and Hendra.” *Annual Review of Virology* 7 (1): 447–73.

Annand, Edward J., Bethany A. Horsburgh, Kai Xu, Peter A. Reid, Ben Poole, Maximillian C. de Kantzow, Nicole Brown, et al. 2021. “Novel Hendra Virus Variant Detected by Sentinel Surveillance of Australian Horses.” *bioRxiv*. https://doi.org/10.1101/2021.07.16.452724.

Arunkumar, Govindakarnavar, Radhakrishnan Chandni, Devendra T. Mourya, Sujeet K. Singh, Rajeev Sadanandan, Preeti Sudan, Balram Bhargava, and Nipah Investigators People and Health Study Group. 2019. “Outbreak Investigation of Nipah Virus Disease in Kerala, India, 2018.” *The Journal of Infectious Diseases* 219 (12): 1867–78.

Avanzato, Victoria A., Kasopefoluwa Y. Oguntuyo, Marina Escalera-Zamudio, Bernardo Gutierrez, Michael Golden, Sergei L. Kosakovsky Pond, Rhys Pryce, et al. 2019. “A Structural Basis for Antibody-Mediated Neutralization of Nipah Virus Reveals a Site of Vulnerability at the Fusion Glycoprotein Apex.” *Proceedings of the National Academy of Sciences of the United States of America* 116 (50): 25057–67.

Baden, Lindsey R., Hana M. El Sahly, Brandon Essink, Karen Kotloff, Sharon Frey, Rick Novak, David Diemert, et al. 2021. “Efficacy and Safety of the mRNA-1273 SARS-CoV-2 Vaccine.” *The New England Journal of Medicine* 384 (5): 403–16.

Barad, Benjamin A., Nathaniel Echols, Ray Yu-Ruei Wang, Yifan Cheng, Frank DiMaio, Paul D. Adams, and James S. Fraser. 2015. “EMRinger: Side Chain–directed Model and Map Validation for 3D Cryo-Electron Microscopy.” *Nature Methods* 12 (10): 943–46.

Barton, Erik S., Douglas W. White, Jason S. Cathelyn, Kelly A. Brett-McClellan, Michael Engle, Michael S. Diamond, Virginia L. Miller, and Herbert W. Virgin 4th. 2007. “Herpesvirus Latency Confers Symbiotic Protection from Bacterial Infection.” *Nature* 447 (7142): 326–29.

Battles, Michael B., Vicente Más, Eduardo Olmedillas, Olga Cano, Mónica Vázquez, Laura Rodríguez, José A. Melero, and Jason S. McLellan. 2017. “Structure and Immunogenicity of Pre-Fusion-Stabilized Human Metapneumovirus F Glycoprotein.” *Nature Communications* 8 (1): 1528.

Blanc, E., P. Roversi, C. Vonrhein, C. Flensburg, S. M. Lea, and G. Bricogne. 2004. “Refinement of Severely Incomplete Structures with Maximum Likelihood in BUSTER–TNT.” *Acta Crystallographica. Section D, Biological Crystallography* 60 (ARRAY(0xaae0084)): 2210–21.

Bonaparte, Matthew I., Antony S. Dimitrov, Katharine N. Bossart, Gary Crameri, Bruce A. Mungall, Kimberly A. Bishop, Vidita Choudhry, et al. 2005. “Ephrin-B2 Ligand Is a Functional Receptor for Hendra Virus and Nipah Virus.” *Proceedings of the National Academy of Sciences of the United States of America* 102 (30): 10652–57.

Borisevich, Viktoriya, Benhur Lee, Andrew Hickey, Blair DeBuysscher, Christopher C. Broder, Heinz Feldmann, and Barry Rockx. 2016. “Escape From Monoclonal Antibody Neutralization Affects Henipavirus Fitness In Vitro and In Vivo.” *The Journal of Infectious Diseases* 213 (3): 448–55.

Bornholdt, Zachary A., Andrew S. Herbert, Chad E. Mire, Shihua He, Robert W. Cross, Anna Z. Wec, Dafna M. Abelson, et al. 2019. “A Two-Antibody Pan-Ebolavirus Cocktail Confers Broad Therapeutic Protection in Ferrets and Nonhuman Primates.” *Cell Host & Microbe* 25 (1): 49–58.e5.

Borst, Andrew J., Connor E. Weidle, Matthew D. Gray, Brandon Frenz, Joost Snijder, M.

Gordon Joyce, Ivelin S. Georgiev, et al. 2018. “Germline VRC01 Antibody Recognition of a Modified Clade C HIV-1 Envelope Trimer and a Glycosylated HIV-1 gp120 Core.” *eLife* 7 (November). https://doi.org/10.7554/eLife.37688.

Bossart, Katharine N., and Christopher C. Broder. 2004. “Viral Glycoprotein-Mediated Cell Fusion Assays Using Vaccinia Virus Vectors.” *Methods in Molecular Biology* 269: 309–32.

Bossart, Katharine N., Deborah L. Fusco, and Christopher C. Broder. 2013. “Paramyxovirus Entry.” *Advances in Experimental Medicine and Biology* 790: 95–127.

Bossart, Katharine N., Bruce A. Mungall, Gary Crameri, Lin-Fa Wang, Bryan T. Eaton, and Christopher C. Broder. 2005. “Inhibition of Henipavirus Fusion and Infection by Heptad-Derived Peptides of the Nipah Virus Fusion Glycoprotein.” *Virology Journal* 2 (July): 57.

Bossart, Katharine N., Barry Rockx, Friederike Feldmann, Doug Brining, Dana Scott, Rachel LaCasse, Joan B. Geisbert, et al. 2012. “A Hendra Virus G Glycoprotein Subunit Vaccine Protects African Green Monkeys from Nipah Virus Challenge.” *Science Translational Medicine* 4 (146): 146ra107.

Bossart, Katharine N., Lin-Fa Wang, Michael N. Flora, Kaw Bing Chua, Sai Kit Lam, Bryan T. Eaton, and Christopher C. Broder. 2002. “Membrane Fusion Tropism and Heterotypic Functional Activities of the Nipah Virus and Hendra Virus Envelope Glycoproteins.” *Journal of Virology* 76 (22): 11186–98.

Bossart, Katharine N., Zhongyu Zhu, Deborah Middleton, Jessica Klippel, Gary Crameri, John Bingham, Jennifer A. McEachern, et al. 2009. “A Neutralizing Human Monoclonal Antibody Protects against Lethal Disease in a New Ferret Model of Acute Nipah Virus Infection.” *PLoS Pathogens* 5 (10): e1000642.

Broder, C. C., P. L. Earl, D. Long, S. T. Abedon, B. Moss, and R. W. Doms. 1994. “Antigenic Implications of Human Immunodeficiency Virus Type 1 Envelope Quaternary Structure: Oligomer-Specific and -Sensitive Monoclonal Antibodies.” *Proceedings of the National Academy of Sciences of the United States of America* 91 (24): 11699–703.

Broder, Christopher C., Dawn L. Weir, and Peter A. Reid. 2016. “Hendra Virus and Nipah Virus Animal Vaccines.” *Vaccine* 34 (30): 3525–34.

Brown, Alan, Fei Long, Robert A. Nicholls, Jaan Toots, Paul Emsley, and Garib Murshudov. 2015. “Tools for Macromolecular Model Building and Refinement into Electron Cryo-Microscopy Reconstructions.” *Acta Crystallographica. Section D, Biological Crystallography* 71 (Pt 1): 136–53.

Bullough, P. A., F. M. Hughson, J. J. Skehel, and D. C. Wiley. 1994. “Structure of Influenza Haemagglutinin at the pH of Membrane Fusion.” *Nature* 371 (6492): 37–43.

Bunka, David H. J., and Peter G. Stockley. 2006. “Aptamers Come of Age - at Last.” *Nature Reviews. Microbiology* 4 (8): 588–96.

Cao, Longxing, Inna Goreshnik, Brian Coventry, James Brett Case, Lauren Miller, Lisa Kozodoy, Rita E. Chen, et al. 2020. “De Novo Design of Picomolar SARS-CoV-2 Miniprotein Inhibitors.” *Science* 370 (6515): 426–31.

Carter, James Richard, Cara Theresia Pager, Stephen Derrick Fowler, and Rebecca Ellis Dutch. 2005. “Role of N-Linked Glycosylation of the Hendra Virus Fusion Protein.” *Journal of Virology* 79 (12): 7922–25.

Cathcart, Andrea L., Colin Havenar-Daughton, Florian A. Lempp, Daphne Ma, Michael A. Schmid, Maria L. Agostini, Barbara Guarino, et al. 2021. “The Dual Function Monoclonal Antibodies VIR-7831 and VIR-7832 Demonstrate Potent in Vitro and in Vivo Activity against SARS-CoV-2.” *bioRxiv*. https://doi.org/10.1101/2021.03.09.434607.

Cerutti, Francesco, Elisa Burdino, Maria Grazia Milia, Tiziano Allice, Gabriella Gregori, Bianca Bruzzone, and Valeria Ghisetti. 2020. “Urgent Need of Rapid Tests for SARS CoV-2 Antigen Detection: Evaluation of the SD-Biosensor Antigen Test for SARS-CoV-2.” *Journal of Clinical Virology: The Official Publication of the Pan American Society for Clinical Virology* 132 (November): 104654.

Chan, Yee-Peng, Min Lu, Somnath Dutta, Lianying Yan, Jennifer Barr, Michael Flora, Yan-Ru Feng, et al. 2012. “Biochemical, Conformational, and Immunogenic Analysis of Soluble Trimeric Forms of Henipavirus Fusion Glycoproteins.” *Journal of Virology* 86 (21): 11457–71.

Chan, Yee-Peng, Lianying Yan, Yan-Ru Feng, and Christopher C. Broder. 2009.

“Preparation of Recombinant Viral Glycoproteins for Novel and Therapeutic Antibody Discovery.” *Methods in Molecular Biology* 525: 31–58, xiii.

Chao, Tzu-Yuan, Shiqi Ren, Enyun Shen, Susan Moore, Shou-Feng Zhang, Li Chen, Charles E. Rupprecht, and Eric Tsao. 2017. “SYN023, a Novel Humanized Monoclonal Antibody Cocktail, for Post-Exposure Prophylaxis of Rabies.” *PLoS Neglected Tropical Diseases* 11 (12): e0006133.

Chen, Shaoxia, Greg McMullan, Abdul R. Faruqi, Garib N. Murshudov, Judith M. Short, Sjors H. W. Scheres, and Richard Henderson. 2013. “High-Resolution Noise Substitution to Measure Overfitting and Validate Resolution in 3D Structure Determination by Single Particle Electron Cryomicroscopy.” *Ultramicroscopy* 135 (December): 24–35.

Chen, Vincent B., W. Bryan Arendall 3rd, Jeffrey J. Headd, Daniel A. Keedy, Robert M. Immormino, Gary J. Kapral, Laura W. Murray, Jane S. Richardson, and David C. Richardson. 2010. “MolProbity: All-Atom Structure Validation for Macromolecular Crystallography.” *Acta Crystallographica. Section D, Biological Crystallography* 66 (Pt 1): 12–21.

Chen, Zhiqiang, Qihan Wu, Jing Chen, Xiaohua Ni, and Jianfeng Dai. 2020. “A DNA Aptamer Based Method for Detection of SARS-CoV-2 Nucleocapsid Protein.” *Virologica Sinica*. https://doi.org/10.1007/s12250-020-00236-z.

Connolly, Sarah A., George P. Leser, Hsien-Shen Yin, Theodore S. Jardetzky, and Robert A. Lamb. 2006. “Refolding of a Paramyxovirus F Protein from Prefusion to

Postfusion Conformations Observed by Liposome Binding and Electron Microscopy.” *Proceedings of the National Academy of Sciences of the United States of America* 103 (47): 17903–8.

Corti, Davide, Lisa A. Purcell, Gyorgy Snell, and David Veesler. 2021. “Tackling COVID-19 with Neutralizing Monoclonal Antibodies.” *Cell* 184 (17): 4593–95.

Cowtan, K., P. Emsley, B. Lohkamp, and W. G. Scott. 2010. “Features and Development of Coot.” *Acta Crystallographica Section D-Biological Crystallography2010*, 486–501.

Cowtan, Kevin. 2006. “The Buccaneer Software for Automated Model Building. 1. Tracing Protein Chains.” *Acta Crystallographica. Section D, Biological Crystallography* 62 (Pt 9): 1002–11.

Dandey, Venkata P., Hui Wei, Zhening Zhang, Yong Zi Tan, Priyamvada Acharya, Edward T. Eng, William J. Rice, Peter A. Kahn, Clinton S. Potter, and Bridget Carragher. 2018. “Spotiton: New Features and Applications.” *Journal of Structural Biology* 202 (2): 161–69.

Dang, Ha V., Yee-Peng Chan, Young-Jun Park, Joost Snijder, Sofia Cheliout Da Silva, Bang Vu, Lianying Yan, et al. 2019. “An Antibody against the F Glycoprotein Inhibits Nipah and Hendra Virus Infections.” *Nature Structural & Molecular Biology* 26 (10): 980–87.

Dang, Ha V., Robert W. Cross, Viktoriya Borisevich, Zachary A. Bornholdt, Brandyn R.

West, Yee-Peng Chan, Chad E. Mire, et al. 2021. “Broadly Neutralizing Antibody Cocktails Targeting Nipah Virus and Hendra Virus Fusion Glycoproteins.” *Nature Structural & Molecular Biology* 28 (5): 426–34.

Darrow, Michele C., John P. Moore, R. John Walker, Klaus Doering, and Russell S. King. 2019. “Chameleon: Next Generation Sample Preparation for CryoEM Based on Spotiton.” *Microscopy and Microanalysis: The Official Journal of Microscopy Society of America, Microbeam Analysis Society, Microscopical Society of Canada* 25 (S2): 994–95.

Dauphin-Ducharme, Philippe, Kyungae Yang, Netzahualcóyotl Arroyo-Currás, Kyle L. Ploense, Yameng Zhang, Julian Gerson, Martin Kurnik, Tod E. Kippin, Milan N. Stojanovic, and Kevin W. Plaxco. 2019. “Electrochemical Aptamer-Based Sensors for Improved Therapeutic Drug Monitoring and High-Precision, Feedback-Controlled Drug Delivery.” *ACS Sensors* 4 (10): 2832–37.

Debat, H., B. Avalle, O. Chose, C. O. Sarde, A. Friboulet, and D. Thomas. 2001. “Overpassing an Aberrant V(kappa) Gene to Sequence an Anti-Idiotypic Abzyme with (beta)-Lactamase-like Activity That Could Have a Linkage with Autoimmune Diseases.” *FASEB Journal: Official Publication of the Federation of American Societies for Experimental Biology* 15 (3): 815–22.

Deng, Jinqi, Fei Tian, Chao Liu, Yuan Liu, Shuai Zhao, Ting Fu, Jiashu Sun, and Weihong Tan. 2021. “Rapid One-Step Detection of Viral Particles Using an Aptamer-Based Thermophoretic Assay.” *Journal of the American Chemical Society*

143 (19): 7261–66.

Dessain, Scott K. 2007. *Human Antibody Therapeutics For Viral Disease*. Springer Science & Business Media.

DiMaio, Frank, Andrew Leaver-Fay, Phil Bradley, David Baker, and Ingemar André. 2011. “Modeling Symmetric Macromolecular Structures in Rosetta3.” *PloS One* 6 (6): e20450.

DiMaio, Frank, Yifan Song, Xueming Li, Matthias J. Brunner, Chunfu Xu, Vincent Conticello, Edward Egelman, Thomas C. Marlovits, Yifan Cheng, and David Baker. 2015. “Atomic-Accuracy Models from 4.5-Å Cryo-Electron Microscopy Data with Density-Guided Iterative Local Refinement.” *Nature Methods*. https://doi.org/10.1038/nmeth.3286.

Dimitrova, Dimana, Vidita Choudhry, and Christopher C. Broder. 2009. “Antibody Fragment Expression and Purification.” *Methods in Molecular Biology* 525: 491–98, xiii.

Dinnes, Jacqueline, Jonathan J. Deeks, Ada Adriano, Sarah Berhane, Clare Davenport, Sabine Dittrich, Devy Emperador, et al. 2020. “Rapid, Point-of-Care Antigen and Molecular-Based Tests for Diagnosis of SARS-CoV-2 Infection.” *Cochrane Database of Systematic Reviews* 8 (August): CD013705.

Dong, Jinhui, Robert W. Cross, Michael P. Doyle, Nurgun Kose, Jarrod J. Mousa, Edward J. Annand, Viktoriya Borisevich, et al. 2020. “Potent Henipavirus

Neutralization by Antibodies Recognizing Diverse Sites on Hendra and Nipah Virus Receptor Binding Protein.” *Cell* 183 (6): 1536–50.e17.

Dougan, Michael, Ajay Nirula, Masoud Azizad, Bharat Mocherla, Robert L. Gottlieb, Peter Chen, Corey Hebert, et al. 2021. “Bamlanivimab plus Etesevimab in Mild or Moderate Covid-19.” *The New England Journal of Medicine* 385 (15): 1382–92.

Doyle, Michael P., Nurgun Kose, Viktoriya Borisevich, Elad Binshtein, Moushimi Amaya, Marcus Nagel, Edward J. Annand, et al. 2021. “Cooperativity Mediated by Rationally Selected Combinations of Human Monoclonal Antibodies Targeting the Henipavirus Receptor Binding Protein.” *Cell Reports* 36 (9): 109628.

Drexler, Jan Felix, Victor Max Corman, Marcel Alexander Müller, Gael Darren Maganga, Peter Vallo, Tabea Binger, Florian Gloza-Rausch, et al. 2012. “Bats Host Major Mammalian Paramyxoviruses.” *Nature Communications* 3 (April): 796.

Dunn, Matthew R., Randi M. Jimenez, and John C. Chaput. 2017. “Analysis of Aptamer Discovery and Technology.” *Nature Reviews Chemistry* 1 (10): 1–16.

Eaton, Bryan T., Christopher C. Broder, Deborah Middleton, and Lin-Fa Wang. 2006. “Hendra and Nipah Viruses: Different and Dangerous.” *Nature Reviews. Microbiology* 4 (1): 23–35.

Ellington, A. D., and J. W. Szostak. 1990. “In Vitro Selection of RNA Molecules That Bind Specific Ligands.” *Nature* 346 (6287): 818–22.

Evans, Philip R., and Garib N. Murshudov. 2013. “How Good Are My Data and What Is the Resolution?” *Acta Crystallographica. Section D, Biological Crystallography* 69 (Pt 7): 1204–14.

Feng, Yang, and Dimiter S. Dimitrov. 2009. “Scaling-up and Production of Therapeutic Antibodies for Preclinical Studies.” *Methods in Molecular Biology* 525: 499–508, xiii.

Ferrara, Francesca, and Nigel Temperton. 2018. “Pseudotype Neutralization Assays: From Laboratory Bench to Data Analysis.” *Methods and Protocols* 1 (1). https://doi.org/10.3390/mps1010008.

Frenz, Brandon, Sebastian Rämisch, Andrew J. Borst, Alexandra C. Walls, Jared Adolf-Bryfogle, William R. Schief, David Veesler, and Frank DiMaio. 2019. “Automatically Fixing Errors in Glycoprotein Structures with Rosetta.” *Structure* 27 (1): 134–39.e3.

Geisbert, T. W., C. E. Mire, J. B. Geisbert, Y-P Chan, K. N. Agans, F. Feldmann, K. A. Fenton, et al. 2014. “Therapeutic Treatment of Nipah Virus Infection in Nonhuman Primates with a Neutralizing Human Monoclonal Antibody.” *Science Translational Medicine*. https://doi.org/10.1126/scitranslmed.3008929.

Goddard, Thomas D., Conrad C. Huang, and Thomas E. Ferrin. 2007. “Visualizing Density Maps with UCSF Chimera.” *Journal of Structural Biology* 157 (1): 281–87.

Goddard, Thomas D., Conrad C. Huang, Elaine C. Meng, Eric F. Pettersen, Gregory S. Couch, John H. Morris, and Thomas E. Ferrin. 2018. “UCSF ChimeraX: Meeting Modern Challenges in Visualization and Analysis.” *Protein Science: A Publication of* *the Protein Society* 27 (1): 14–25.

Gotrik, Michael R., Trevor A. Feagin, Andrew T. Csordas, Margaret A. Nakamoto, and H. Tom Soh. 2016. “Advancements in Aptamer Discovery Technologies.” *Accounts of Chemical Research* 49 (9): 1903–10.

Harrison, Stephen C. 2015. “Viral Membrane Fusion.” *Virology* 479-480 (May): 498–507.

Hashiguchi, T., Kajikawa, M., Maita, N., Takeda, M., Kuroki, K., Sasaki, K., Kohda, D., Yanagi, Y., & Maenaka, K. (2007). Crystal structure of measles virus hemagglutinin provides insight into effective vaccines. In Proceedings of the National Academy of Sciences (Vol. 104, Issue 49, pp. 19535–19540). https://doi.org/10.1073/pnas.0707830104

Hashiguchi, Takao, Yoshinari Fukuda, Rei Matsuoka, Daisuke Kuroda, Marie Kubota, Yuta Shirogane, Shumpei Watanabe, et al. 2018. “Structures of the Prefusion Form of Measles Virus Fusion Protein in Complex with Inhibitors.” *Proceedings of the National Academy of Sciences of the United States of America* 115 (10): 2496–2501.

Helenius, Ari, and Markus Aebi. 2004. “Roles of N-Linked Glycans in the Endoplasmic Reticulum.” *Annual Review of Biochemistry* 73: 1019–49.

Hernandez, Luiza I., Isabel Machado, Thomas Schafer, and Frank J. Hernandez. 2015. “Aptamers Overview: Selection, Features and Applications.” *Current Topics in*

Medicinal Chemistry 15 (12): 1066–81.

Huynh-Do, Uyen, Cécile Vindis, Hua Liu, Douglas Pat Cerretti, Jeffrey T. McGrew, Miriam Enriquez, Jin Chen, and Thomas O. Daniel. 2002. “Ephrin-B1 Transduces Signals to Activate Integrin-Mediated Migration, Attachment and Angiogenesis.” *Journal of Cell Science* 115 (Pt 15): 3073–81.

Jackson, Lisa A., Evan J. Anderson, Nadine G. Rouphael, Paul C. Roberts, Mamodikoe Makhene, Rhea N. Coler, Michele P. McCullough, et al. 2020. “An mRNA Vaccine against SARS-CoV-2 - Preliminary Report.” *The New England Journal of Medicine* 383 (20): 1920–31.

Jain, Tilak, Patrick Sheehan, John Crum, Bridget Carragher, and Clinton S. Potter. 2012. “Spotiton: A Prototype for an Integrated Inkjet Dispense and Vitrification System for Cryo-TEM.” *Journal of Structural Biology* 179 (1): 68–75.

Joung, Julia, Alim Ladha, Makoto Saito, Nam-Gyun Kim, Ann E. Woolley, Michael Segel, Robert P. J. Barretto, et al. 2020. “Detection of SARS-CoV-2 with SHERLOCK One-Pot Testing.” *The New England Journal of Medicine* 383 (15): 1492–94.

Kabsch, Wolfgang. 2010. “XDS.” *Acta Crystallographica. Section D, Biological Crystallography* 66 (Pt 2): 125–32.

Kacherovsky, Nataly, Ian I. Cardle, Emmeline L. Cheng, Jonathan L. Yu, Michael L. Baldwin, Stephen J. Salipante, Michael C. Jensen, and Suzie H. Pun. 2019.

"Traceless Aptamer-Mediated Isolation of CD8+ T Cells for Chimeric Antigen Receptor T-Cell Therapy." *Nature Biomedical Engineering* 3 (10): 783–95.

Kacherovsky, Nataly, Lucy F. Yang, Ha V. Dang, Emmeline L. Cheng, Ian I. Cardle, Alexandra C. Walls, Matthew McCallum, et al. 2021. "Discovery and Characterization of Spike N-terminal Domain-binding Aptamers for Rapid SARS-CoV-2 Detection." *Angewandte Chemie* 133 (39): 21381–85.

Kalbermatter, David, Neeta Shrestha, Flavio M. Gall, Marianne Wyss, Rainer Riedl, Philippe Plattet, and Dimitrios Fotiadis. 2020. "Cryo-EM Structure of the Prefusion State of Canine Distemper Virus Fusion Protein Ectodomain." *Journal of Structural Biology: X* 4 (February): 100021.

Ke, Zunlong, Joaquin Oton, Kun Qu, Mirko Cortese, Vojtech Zila, Lesley McKeane, Takanori Nakane, et al. 2020. "Structures and Distributions of SARS-CoV-2 Spike Proteins on Intact Virions." *Nature* 588 (7838): 498–502.

Kohmer, Niko, Tuna Toptan, Christiane Pallas, Onur Karaca, Annika Pfeiffer, Sandra Westhaus, Marek Widera, et al. 2021. "The Comparative Clinical Performance of Four SARS-CoV-2 Rapid Antigen Tests and Their Correlation to Infectivity In Vitro." *Journal of Clinical Medicine Research* 10 (2). https://doi.org/10.3390/jcm10020328.

Kondo, Naoyuki, Kosuke Miyauchi, Fanxia Meng, Aikichi Iwamoto, and Zene Matsuda. 2010. "Conformational Changes of the HIV-1 Envelope Protein during Membrane Fusion Are Inhibited by the Replacement of Its Membrane-Spanning Domain." *The Journal of Biological Chemistry* 285 (19): 14681–88.

Krarup, Anders, Daphné Truan, Polina Furmanova-Hollenstein, Lies Bogaert, Pascale Bouchier, Ilona J. M. Bisschop, Myra N. Widjojoatmodjo, et al. 2015. “A Highly Stable Prefusion RSV F Vaccine Derived from Structural Analysis of the Fusion Mechanism.” *Nature Communications*. https://doi.org/10.1038/ncomms9143.

Krüttgen, Alexander, Christian G. Cornelissen, Michael Dreher, Mathias W. Hornef, Matthias Imöhl, and Michael Kleines. 2021. “Comparison of the SARS-CoV-2 Rapid Antigen Test to the Real Star Sars-CoV-2 RT PCR Kit.” *Journal of Virological Methods* 288 (February): 114024.

Kuai, Hailan, Zilong Zhao, Liuting Mo, Hui Liu, Xiaoxiao Hu, Ting Fu, Xiaobing Zhang, and Weihong Tan. 2017. “Circular Bivalent Aptamers Enable in Vivo Stability and Recognition.” *Journal of the American Chemical Society* 139 (27): 9128–31.

Laing, Eric D., Moushimi Amaya, Chanakha K. Navaratnarajah, Yan-Ru Feng, Roberto Cattaneo, Lin-Fa Wang, and Christopher C. Broder. 2018. “Rescue and Characterization of Recombinant Cedar Virus, a Non-Pathogenic Henipavirus Species.” *Virology Journal* 15 (1): 56.

Laing, Eric D., Chanakha K. Navaratnarajah, Sofia Cheliout Da Silva, Stephanie R. Petzing, Yan Xu, Spencer L. Sterling, Glenn A. Marsh, et al. 2019. “Structural and Functional Analyses Reveal Promiscuous and Species Specific Use of Ephrin Receptors by Cedar Virus.” *Proceedings of the National Academy of Sciences of the United States of America* 116 (41): 20707–15.

Lambert-Niclot, Sidonie, Alexis Cuffel, Samuel Le Pape, Christelle Vauloup-Fellous, Laurence Morand-Joubert, Anne-Marie Roque-Afonso, Jérôme Le Goff, and Constance Delaugerre. 2020. “Evaluation of a Rapid Diagnostic Assay for Detection of SARS-CoV-2 Antigen in Nasopharyngeal Swabs.” *Journal of Clinical Microbiology* 58 (8). https://doi.org/10.1128/JCM.00977-20.

Lander, Gabriel C., Scott M. Stagg, Neil R. Voss, Anchi Cheng, Denis Fellmann, James Pulokas, Craig Yoshioka, et al. 2009. “Appion: An Integrated, Database-Driven Pipeline to Facilitate EM Image Processing.” *Journal of Structural Biology* 166 (1): 95–102.

Lawrence, Michael C., Natalie A. Borg, Victor A. Streltsov, Patricia A. Pilling, V. Chandana Epa, Joseph N. Varghese, Jennifer L. McKimm-Breschkin, and Peter M. Colman. 2004. “Structure of the Haemagglutinin-Neuraminidase from Human Parainfluenza Virus Type III.” *Journal of Molecular Biology* 335 (5): 1343–57.

Lee, Benhur, and Zeynep Akyol Ataman. 2011. “Modes of Paramyxovirus Fusion: A Henipavirus Perspective.” *Trends in Microbiology* 19 (8): 389–99.

Lee, E-Chiang, Qi Liang, Hanif Ali, Luke Bayliss, Alastair Beasley, Tara Bloomfield-Gerdes, Laura Bonoli, et al. 2014. “Complete Humanization of the Mouse Immunoglobulin Loci Enables Efficient Therapeutic Antibody Discovery.” *Nature Biotechnology* 32 (4): 356–63.

Lee, Jin K., Andrew Prussia, James P. Snyder, and Richard K. Plemper. 2007. “Reversible Inhibition of the Fusion Activity of Measles Virus F Protein by an Engineered Intersubunit Disulfide Bridge.” *Journal of Virology* 81 (16): 8821–26.

Lee, Seung-Ho, Kijin Kim, Jongwoo Kim, Jin Sun No, Kyungmin Park, Shailesh Budhathoki, Seung Ho Lee, et al. 2021. “Discovery and Genetic Characterization of Novel Paramyxoviruses Related to the Genus Henipavirus in Crocidura Species in the Republic of Korea.” *Viruses* 13 (10): 2020.

Lempp, Florian A., Leah B. Soriaga, Martin Montiel-Ruiz, Fabio Benigni, Julia Noack, Young-Jun Park, Siro Bianchi, et al. 2021. “Lectins Enhance SARS-CoV-2 Infection and Influence Neutralizing Antibodies.” *Nature* 598 (7880): 342–47.

Li, Fang. 2016. “Structure, Function, and Evolution of Coronavirus Spike Proteins.” *Annual Review of Virology* 3 (1): 237–61.

Liu, Jun, Mingxu You, Ying Pu, Huixia Liu, Mao Ye, and Weihong Tan. 2011. “Recent Developments in Protein and Cell-Targeted Aptamer Selection and Applications.” *Current Medicinal Chemistry* 18 (27): 4117–25.

Liu, Qian, Jacquelyn A. Stone, Birgit Bradel-Tretheway, Jeffrey Dabundo, Javier A. Benavides Montano, Jennifer Santos-Montanez, Scott B. Biering, et al. 2013. “Unraveling a Three-Step Spatiotemporal Mechanism of Triggering of Receptor-Induced Nipah Virus Fusion and Cell Entry.” *PLoS Pathogens* 9 (11): e1003770.

Liu, Ran, Lei He, Yuansheng Hu, Zhaofeng Luo, and Jingjing Zhang. 2020. “A Serological Aptamer-Assisted Proximity Ligation Assay for COVID-19 Diagnosis and Seeking Neutralizing Aptamers.” *Chemical Science* 11 (44): 12157–64.

Logtenberg, Ton. 2007. “Antibody Cocktails: Next-Generation Biopharmaceuticals with

Improved Potency." *Trends in Biotechnology* 25 (9): 390–94.

Loomis, Rebecca J., Guillaume B. E. Stewart-Jones, Yaroslav Tsybovsky, Ria T. Caringal, Kaitlyn M. Morabito, Jason S. McLellan, Amy L. Chamberlain, et al. 2020. "Structure-Based Design of Nipah Virus Vaccines: A Generalizable Approach to Paramyxovirus Immunogen Development." *Frontiers in Immunology* 11 (June): 842.

Luby, Stephen P., and Christopher C. Broder. 2014. "Paramyxoviruses: Henipaviruses." In *Viral Infections of Humans: Epidemiology and Control*, edited by Richard A. Kaslow, Lawrence R. Stanberry, and James W. Le Duc, 519–36. Boston, MA: Springer US.

Luby, Stephen P., and Emily S. Gurley. 2012. "Epidemiology of Henipavirus Disease in Humans." *Current Topics in Microbiology and Immunology* 359: 25–40.

Mak, Gannon Ck, Peter Kc Cheng, Stephen Sy Lau, Kitty Ky Wong, C. S. Lau, Edman Tk Lam, Rickjason Cw Chan, and Dominic Nc Tsang. 2020. "Evaluation of Rapid Antigen Test for Detection of SARS-CoV-2 Virus." *Journal of Clinical Virology: The Official Publication of the Pan American Society for Clinical Virology* 129 (August): 104500.

Marcandalli, Jessica, Brooke Fiala, Sebastian Ols, Michela Perotti, Willem de van der Schueren, Joost Snijder, Edgar Hodge, et al. 2019. "Induction of Potent Neutralizing Antibody Responses by a Designed Protein Nanoparticle Vaccine for Respiratory Syncytial Virus." *Cell* 176 (6): 1420–31.e17.

McCallum, Matthew, Anna De Marco, Florian A. Lempp, M. Alejandra Tortorici, Dora Pinto, Alexandra C. Walls, Martina Beltramello, et al. 2021. “N-Terminal Domain Antigenic Mapping Reveals a Site of Vulnerability for SARS-CoV-2.” *Cell* 184 (9): 2332–47.e16.

McCoy, Airlie J., Ralf W. Grosse-Kunstleve, Paul D. Adams, Martyn D. Winn, Laurent C. Storoni, and Randy J. Read. 2007. “Phaser Crystallographic Software.” *Journal of Applied Crystallography* 40 (Pt 4): 658–74.

McLellan, Jason S., Man Chen, M. Gordon Joyce, Mallika Sastry, Guillaume B. E. Stewart-Jones, Yongping Yang, Baoshan Zhang, et al. 2013. “Structure-Based Design of a Fusion Glycoprotein Vaccine for Respiratory Syncytial Virus.” *Science* 342 (6158): 592–98.

McLellan, Jason S., Man Chen, Sherman Leung, Kevin W. Graepel, Xiulian Du, Yongping Yang, Tongqing Zhou, et al. 2013. “Structure of RSV Fusion Glycoprotein Trimer Bound to a Prefusion-Specific Neutralizing Antibody.” *Science*, May. https://science.sciencemag.org/content/340/6136/1113.abstract.

McLellan, Jason S., Yongping Yang, Barney S. Graham, and Peter D. Kwong. 2011. “Structure of Respiratory Syncytial Virus Fusion Glycoprotein in the Postfusion Conformation Reveals Preservation of Neutralizing Epitopes.” *Journal of Virology* 85 (15): 7788–96.

Mire, Chad E., Yee-Peng Chan, Viktoriya Borisevich, Robert W. Cross, Lianying Yan, Krystle N. Agans, Ha V. Dang, et al. 2020. “A Cross-Reactive Humanized

Monoclonal Antibody Targeting Fusion Glycoprotein Function Protects Ferrets Against Lethal Nipah Virus and Hendra Virus Infection." *The Journal of Infectious Diseases* 221 (Suppl 4): S471–79.

Mishra, Akaash K., Crystal L. Moyer, Dafna M. Abelson, Daniel J. Deer, Kamel El Omari, Ramona Duman, Leslie Lobel, et al. 2020. "Structure and Characterization of Crimean-Congo Hemorrhagic Fever Virus GP38." *Journal of Virology* 94 (8). https://doi.org/10.1128/JVI.02005-19.

Moll Markus, Kaufmann Andreas, and Maisner Andrea. 2004. "Influence of N-Glycans on Processing and Biological Activity of the Nipah Virus Fusion Protein." *Journal of Virology* 78 (13): 7274–78.

Mulangu, Sabue, Lori E. Dodd, Richard T. Davey Jr, Olivier Tshiani Mbaya, Michael Proschan, Daniel Mukadi, Mariano Lusakibanza Manzo, et al. 2019. "A Randomized, Controlled Trial of Ebola Virus Disease Therapeutics." *The New England Journal of Medicine* 381 (24): 2293–2303.

Pager, Cara Theresia, Willie Warren Craft Jr, Jared Patch, and Rebecca Ellis Dutch. 2006. "A Mature and Fusogenic Form of the Nipah Virus Fusion Protein Requires Proteolytic Processing by Cathepsin L." *Virology* 346 (2): 251–57.

Pager, Cara Theresia, and Rebecca Ellis Dutch. 2005. "Cathepsin L Is Involved in Proteolytic Processing of the Hendra Virus Fusion Protein." *Journal of Virology* 79 (20): 12714–20.

Park, Young-Jun, Anna De Marco, Tyler N. Starr, Zhuoming Liu, Dora Pinto, Alexandra C. Walls, Fabrizia Zatta, et al. 2021. “Antibody-Mediated Broad Sarbecovirus Neutralization through ACE2 Molecular Mimicry.” *bioRxiv*. https://doi.org/10.1101/2021.10.13.464254.

Pavelka, Martin, Kevin Van-Zandvoort, Sam Abbott, Katharine Sherratt, Marek Majdan, CMMID COVID-19 working group, Inštitút Zdravotných Analýz, et al. 2021. “The Impact of Population-Wide Rapid Antigen Testing on SARS-CoV-2 Prevalence in Slovakia.” *Science* 372 (6542): 635–41.

Pernet, Olivier, Bradley S. Schneider, Shannon M. Beaty, Matthew LeBreton, Tatyana E. Yun, Arnold Park, Trevor T. Zachariah, et al. 2014. “Evidence for Henipavirus Spillover into Human Populations in Africa.” *Nature Communications* 5 (November): 5342.

Piccoli, Luca, Young-Jun Park, M. Alejandra Tortorici, Nadine Czudnochowski, Alexandra C. Walls, Martina Beltramello, Chiara Silacci-Fregni, et al. 2020. “Mapping Neutralizing and Immunodominant Sites on the SARS-CoV-2 Spike Receptor-Binding Domain by Structure-Guided High-Resolution Serology.” *Cell* 183 (4): 1024–42.e21.

Pinto, Dora, Young-Jun Park, Martina Beltramello, Alexandra C. Walls, M. Alejandra Tortorici, Siro Bianchi, Stefano Jaconi, et al. 2020. “Cross-Neutralization of SARS-CoV-2 by a Human Monoclonal SARS-CoV Antibody.” *Nature* 583 (7815): 290–95.

Playford, Elliott Geoffrey, Trent Munro, Stephen M. Mahler, Suzanne Elliott, Michael

Gerometta, Kym L. Hoger, Martina L. Jones, et al. 2020. “Safety, Tolerability, Pharmacokinetics, and Immunogenicity of a Human Monoclonal Antibody Targeting the G Glycoprotein of Henipaviruses in Healthy Adults: A First-in-Human, Randomised, Controlled, Phase 1 Study.” *The Lancet Infectious Diseases* 20 (4): 445–54.

Porte, Lorena, Paulette Legarraga, Valeska Vollrath, Ximena Aguilera, José M. Munita, Rafael Araos, Gabriel Pizarro, et al. 2020. “Evaluation of a Novel Antigen-Based Rapid Detection Test for the Diagnosis of SARS-CoV-2 in Respiratory Samples.” *International Journal of Infectious Diseases: IJID: Official Publication of the International Society for Infectious Diseases* 99 (October): 328–33.

Punjani, Ali, John L. Rubinstein, David J. Fleet, and Marcus A. Brubaker. 2017. “cryoSPARC: Algorithms for Rapid Unsupervised Cryo-EM Structure Determination.” *Nature Methods* 14 (3): 290–96.

Punjani, Ali, Haowei Zhang, and David J. Fleet. 2020. “Non-Uniform Refinement: Adaptive Regularization Improves Single-Particle Cryo-EM Reconstruction.” *Nature Methods* 17 (12): 1214–21.

Qiu, Xiangguo, Gary Wong, Jonathan Audet, Alexander Bello, Lisa Fernando, Judie B. Alimonti, Hugues Fausther-Bovendo, et al. 2014. “Reversion of Advanced Ebola Virus Disease in Nonhuman Primates with ZMapp.” *Nature* 514 (7520): 47–53.

Quijano-Rubio, Alfredo, Hsien-Wei Yeh, Jooyoung Park, Hansol Lee, Robert A. Langan, Scott E. Boyken, Marc J. Lajoie, et al. 2021. “De Novo Design of Modular and

Tunable Protein Biosensors.” *Nature* 591 (7850): 482–87.

Rao, Vamkudoth Koteswara. 2020. “Point of Care Diagnostic Devices for Rapid Detection of Novel Coronavirus (SARS-nCoV19) Pandemic: A Review.” *Frontiers in Nanotechnology* 2: 22.

Rey, Felix A., and Shee-Mei Lok. 2018. “Common Features of Enveloped Viruses and Implications for Immunogen Design for Next-Generation Vaccines.” *Cell* 172 (6): 1319–34.

Robertson, D. L., and G. F. Joyce. 1990. “Selection in Vitro of an RNA Enzyme That Specifically Cleaves Single-Stranded DNA.” *Nature* 344 (6265): 467–68.

Rockx, Barry, Eric Donaldson, Matthew Frieman, Timothy Sheahan, Davide Corti, Antonio Lanzavecchia, and Ralph S. Baric. 2010. “Escape from Human Monoclonal Antibody Neutralization Affects in Vitro and in Vivo Fitness of Severe Acute Respiratory Syndrome Coronavirus.” *The Journal of Infectious Diseases* 201 (6): 946–55.

Roossinck, Marilyn J. 2011. “The Good Viruses: Viral Mutualistic Symbioses.” *Nature Reviews. Microbiology* 9 (2): 99–108.

Rosenthal, Peter B., and Richard Henderson. 2003. “Optimal Determination of Particle Orientation, Absolute Hand, and Contrast Loss in Single-Particle Electron Cryomicroscopy.” *Journal of Molecular Biology* 333 (4): 721–45.

Sastre, Patricia, José A. Melero, Blanca García-Barreno, and Concepción Palomo.

2005. “Comparison of Affinity Chromatography and Adsorption to Vaccinia Virus Recombinant Infected Cells for Depletion of Antibodies Directed against Respiratory Syncytial Virus Glycoproteins Present in a Human Immunoglobulin Preparation.” *Journal of Medical Virology* 76 (2): 248–55.

Scheres, Sjors H. W., and Shaoxia Chen. 2012. “Prevention of Overfitting in Cryo-EM Structure Determination.” *Nature Methods* 9 (9): 853–54.

Schmitz, Anton, Anna Weber, Mehtap Bayin, Stefan Breuers, Volkmar Fieberg, Michael Famulok, and Günter Mayer. 2021. “A SARS-CoV-2 Spike Binding DNA Aptamer That Inhibits Pseudovirus Infection by an RBD-Independent Mechanism*.” *Angewandte Chemie* 60 (18): 10279–85.

———. n.d. “A SARS-CoV-2 Spike Binding DNA Aptamer That Inhibits Pseudovirus Infection in Vitro by an RBD Independent Mechanism.” https://doi.org/10.1101/2020.12.23.424171.

Scohy, Anaïs, Ahalieyah Anantharajah, Monique Bodéus, Benoît Kabamba-Mukadi, Alexia Verroken, and Hector Rodriguez-Villalobos. 2020. “Low Performance of Rapid Antigen Detection Test as Frontline Testing for COVID-19 Diagnosis.” *Journal of Clinical Virology: The Official Publication of the Pan American Society for Clinical Virology* 129 (August): 104455.

Sefah, Kwame, Dihua Shangguan, Xiangling Xiong, Meghan B. O’Donoghue, and Weihong Tan. 2010. “Development of DNA Aptamers Using Cell-SELEX.” *Nature Protocols* 5 (6): 1169–85.

Singh, Naveen K., Partha Ray, Aaron F. Carlin, Celestine Magallanes, Sydney C. Morgan, Louise C. Laurent, Eliah S. Aronoff-Spencer, and Drew A. Hall. 2021. “Hitting the Diagnostic Sweet Spot: Point-of-Care SARS-CoV-2 Salivary Antigen Testing with an off-the-Shelf Glucometer.” *Biosensors & Bioelectronics* 180 (May): 113111.

Song, Yanling, Jia Song, Xinyu Wei, Mengjiao Huang, Miao Sun, Lin Zhu, Bingqian Lin, Haicong Shen, Zhi Zhu, and Chaoyong Yang. 2020. “Discovery of Aptamers Targeting the Receptor-Binding Domain of the SARS-CoV-2 Spike Glycoprotein.” *Analytical Chemistry* 92 (14): 9895–9900.

Starr, Tyler N., Nadine Czudnochowski, Zhuoming Liu, Fabrizia Zatta, Young-Jun Park, Amin Addetia, Dora Pinto, et al. 2021. “SARS-CoV-2 RBD Antibodies That Maximize Breadth and Resistance to Escape.” *Nature* 597 (7874): 97–102.

Stewart-Jones, Guillaume B. E., Gwo-Yu Chuang, Kai Xu, Tongqing Zhou, Priyamvada Acharya, Yaroslav Tsybovsky, Li Ou, et al. 2018. “Structure-Based Design of a Quadrivalent Fusion Glycoprotein Vaccine for Human Parainfluenza Virus Types 1–4.” *Proceedings of the National Academy of Sciences of the United States of America* 115 (48): 12265–70.

Stewart-Jones, Guillaume B. E., Cinque Soto, Thomas Lemmin, Gwo-Yu Chuang, Aliaksandr Druz, Rui Kong, Paul V. Thomas, et al. 2016. “Trimeric HIV-1-Env Structures Define Glycan Shields from Clades A, B, and G.” *Cell* 165 (4): 813–26.

Suloway, Christian, James Pulokas, Denis Fellmann, Anchi Cheng, Francisco Guerra, Joel Quispe, Scott Stagg, Clinton S. Potter, and Bridget Carragher. 2005. “Automated Molecular Microscopy: The New Leginon System.” *Journal of Structural Biology* 151 (1): 41–60.

Sun, Miao, Siwen Liu, Xinyu Wei, Shuang Wan, Mengjiao Huang, Ting Song, Yao Lu, et al. 2021a. “Aptamer Blocking Strategy Inhibits SARS-CoV-2 Virus Infection.” *Angewandte Chemie* 60 (18): 10266–72.

———. 2021b. “Aptamer Blocking Strategy Inhibits SARS-CoV-2 Virus Infection.” *Angewandte Chemie* 133 (18): 10354–60.

Swanson, Kurt A., Ethan C. Settembre, Christine A. Shaw, Antu K. Dey, Rino Rappuoli, Christian W. Mandl, Philip R. Dormitzer, and Andrea Carfi. 2011. “Structural Basis for Immunization with Postfusion Respiratory Syncytial Virus Fusion F Glycoprotein (RSV F) to Elicit High Neutralizing Antibody Titers.” *Proceedings of the National Academy of Sciences of the United States of America* 108 (23): 9619–24.

Tortorici, M. Alejandra, Martina Beltramello, Florian A. Lempp, Dora Pinto, Ha V. Dang, Laura E. Rosen, Matthew McCallum, et al. 2020. “Ultrapotent Human Antibodies Protect against SARS-CoV-2 Challenge via Multiple Mechanisms.” *Science* 370 (6519): 950–57.

Tortorici, M. Alejandra, Nadine Czudnochowski, Tyler N. Starr, Roberta Marzi, Alexandra C. Walls, Fabrizia Zatta, John E. Bowen, et al. 2021. “Broad Sarbecovirus Neutralization by a Human Monoclonal Antibody.” *Nature* 597 (7874): 103–8.

Tortorici, M. Alejandra, and David Veesler. 2019. “Chapter Four - Structural Insights into Coronavirus Entry.” In *Advances in Virus Research*, edited by Félix A. Rey, 105:93–116. Academic Press.

Tuerk, C., and L. Gold. 1990. “Systematic Evolution of Ligands by Exponential Enrichment: RNA Ligands to Bacteriophage T4 DNA Polymerase.” *Science* 249 (4968): 505–10.

Vagin, Alexei A., Roberto A. Steiner, Andrey A. Lebedev, Liz Potterton, Stuart McNicholas, Fei Long, and Garib N. Murshudov. 2004. “REFMAC5 Dictionary: Organization of Prior Chemical Knowledge and Guidelines for Its Use.” *Acta Crystallographica. Section D, Biological Crystallography* 60 (Pt 12 Pt 1): 2184–95.

Voss, N. R., C. K. Yoshioka, M. Radermacher, C. S. Potter, and B. Carragher. 2009. “DoG Picker and TiltPicker: Software Tools to Facilitate Particle Selection in Single Particle Electron Microscopy.” *Journal of Structural Biology* 166 (2): 205–13.

Voss, William N., Yixuan J. Hou, Nicole V. Johnson, George Delidakis, Jin Eyun Kim, Kamyab Javanmardi, Andrew P. Horton, et al. 2021. “Prevalent, Protective, and Convergent IgG Recognition of SARS-CoV-2 Non-RBD Spike Epitopes.” *Science* 372 (6546): 1108–12.

Walls, Alexandra C., Young-Jun Park, M. Alejandra Tortorici, Abigail Wall, Andrew T. McGuire, and David Veesler. 2020. “Structure, Function, and Antigenicity of the SARS-CoV-2 Spike Glycoprotein.” *Cell* 183 (6): 1735.

Walls, Alexandra C., Xiaoli Xiong, Young-Jun Park, M. Alejandra Tortorici, Joost Snijder, Joel Quispe, Elisabetta Cameroni, et al. 2020. “Unexpected Receptor Functional Mimicry Elucidates Activation of Coronavirus Fusion.” *Cell* 183 (6): 1732.

Wang, Jianning, Danielle E. Anderson, Kim Halpin, Xiao Hong, Honglei Chen, Som Walker, Stacey Valdeter, et al. 2021. “A New Hendra Virus Genotype Found in Australian Flying Foxes.” *Virology Journal* 18 (1): 197.

Wang, Ray Yu-Ruei, Yifan Song, Benjamin A. Barad, Yifan Cheng, James S. Fraser, and Frank DiMaio. 2016. “Automated Structure Refinement of Macromolecular Assemblies from Cryo-EM Maps Using Rosetta.” *eLife* 5 (September). https://doi.org/10.7554/eLife.17219.

Wang, Zhongde, Murisiku Raifu, Meredith Howard, Laurie Smith, David Hansen, Richard Goldsby, and David Ratner. 2000. “Universal PCR Amplification of Mouse Immunoglobulin Gene Variable Regions: The Design of Degenerate Primers and an Assessment of the Effect of DNA Polymerase 3′ to 5′ Exonuclease Activity.” *Journal of Immunological Methods* 233 (1): 167–77.

Wec, Anna Z., Zachary A. Bornholdt, Shihua He, Andrew S. Herbert, Eileen Goodwin, Ariel S. Wirchnianski, Bronwyn M. Gunn, et al. 2019. “Development of a Human Antibody Cocktail That Deploys Multiple Functions to Confer Pan-Ebolavirus Protection.” *Cell Host & Microbe* 25 (1): 39–48.e5.

Weinreich, David M., Sumathi Sivapalasingam, Thomas Norton, Shazia Ali, Haitao Gao, Rafia Bhore, Bret J. Musser, et al. 2021. “REGN-COV2, a Neutralizing Antibody

Cocktail, in Outpatients with Covid-19.” *The New England Journal of Medicine* 384 (3): 238–51.

West, Brandyn R., Crystal L. Moyer, Liam B. King, Marnie L. Fusco, Jacob C. Milligan, Sean Hui, and Erica Ollmann Saphire. 2018. “Structural Basis of Pan-Ebolavirus Neutralization by a Human Antibody against a Conserved, yet Cryptic Epitope.” *mBio* 9 (5). https://doi.org/10.1128/mBio.01674-18.

Wilson, I. A., J. J. Skehel, and D. C. Wiley. 1981. “Structure of the Haemagglutinin Membrane Glycoprotein of Influenza Virus at 3 A Resolution.” *Nature* 289 (5796): 366–73.

Wong, Joyce J. W., Reay G. Paterson, Robert A. Lamb, and Theodore S. Jardetzky. 2016. “Structure and Stabilization of the Hendra Virus F Glycoprotein in Its Prefusion Form.” *Proceedings of the National Academy of Sciences of the United States of America* 113 (4): 1056–61.

Wrapp, Daniel, Nianshuang Wang, Kizzmekia S. Corbett, Jory A. Goldsmith, Ching-Lin Hsieh, Olubukola Abiona, Barney S. Graham, and Jason S. McLellan. 2020. “Cryo-EM Structure of the 2019-nCoV Spike in the Prefusion Conformation.” *bioRxiv : The Preprint Server for Biology*, February. https://doi.org/10.1101/2020.02.11.944462.

Wyllie, Anne L., John Fournier, Arnau Casanovas-Massana, Melissa Campbell, Maria Tokuyama, Pavithra Vijayakumar, Joshua L. Warren, et al. 2020. “Saliva or Nasopharyngeal Swab Specimens for Detection of SARS-CoV-2.” *The New England Journal of Medicine* 383 (13): 1283–86.

Xu, Kai, Yee-Peng Chan, Birgit Bradel-Tretheway, Zeynep Akyol-Ataman, Yongqun Zhu, Somnath Dutta, Lianying Yan, et al. 2015. “Crystal Structure of the Pre-Fusion Nipah Virus Fusion Glycoprotein Reveals a Novel Hexamer-of-Trimers Assembly.” *PLoS Pathogens* 11 (12): e1005322.

Xu, Kai, Barry Rockx, Yihu Xie, Blair L. DeBuysscher, Deborah L. Fusco, Zhongyu Zhu, Yee-Peng Chan, et al. 2013. “Crystal Structure of the Hendra Virus Attachment G Glycoprotein Bound to a Potent Cross-Reactive Neutralizing Human Monoclonal Antibody.” *PLoS Pathogens* 9 (10): e1003684.

Yin, Hsien-Sheng, Reay G. Paterson, Xiaolin Wen, Robert A. Lamb, and Theodore S. Jardetzky. 2005. “Structure of the Uncleaved Ectodomain of the Paramyxovirus (hPIV3) Fusion Protein.” *Proceedings of the National Academy of Sciences of the United States of America* 102 (26): 9288–93.

Yin, Hsien-Sheng, Xiaolin Wen, Reay G. Paterson, Robert A. Lamb, and Theodore S. Jardetzky. 2006. “Structure of the Parainfluenza Virus 5 F Protein in Its Metastable, Prefusion Conformation.” *Nature* 439 (7072): 38–44.

Zhang, Kai. 2016. “Gctf: Real-Time CTF Determination and Correction.” *Journal of Structural Biology* 193 (1): 1–12.

Zhang, Liyun, Xiaona Fang, Xingbo Liu, Huichao Ou, Haiyan Zhang, Jinjun Wang, Qian Li, Huanyi Cheng, Wenyi Zhang, and Zhaofeng Luo. 2020. “Discovery of Sandwich Type COVID-19 Nucleocapsid Protein DNA Aptamers.” *Chemical Communications* 56 (70): 10235–38.

Zhang, Yong-Zhen, and Edward C. Holmes. 2020. “A Genomic Perspective on the Origin and Emergence of SARS-CoV-2.” *Cell* 181 (2): 223–27.

Zheng, Shawn Q., Eugene Palovcak, Jean-Paul Armache, Kliment A. Verba, Yifan Cheng, and David A. Agard. 2017. “MotionCor2: Anisotropic Correction of Beam-Induced Motion for Improved Cryo-Electron Microscopy.” *Nature Methods* 14 (4): 331–32.

Zhou, Jiehua, and John Rossi. 2017. “Aptamers as Targeted Therapeutics: Current Potential and Challenges.” *Nature Reviews. Drug Discovery* 16 (6): 440.

Zhu, Qinchang, Ge Liu, and Masaaki Kai. 2015. “DNA Aptamers in the Diagnosis and Treatment of Human Diseases.” *Molecules* 20 (12): 20979–97.

Zhu, Zhongyu, Katharine N. Bossart, Kimberly A. Bishop, Gary Crameri, Antony S. Dimitrov, Jennifer A. McEachern, Yang Feng, et al. 2008. “Exceptionally Potent Cross-Reactive Neutralization of Nipah and Hendra Viruses by a Human Monoclonal Antibody.” *The Journal of Infectious Diseases* 197 (6): 846–53.

Zhu, Zhongyu, Antony S. Dimitrov, Katharine N. Bossart, Gary Crameri, Kimberly A. Bishop, Vidita Choudhry, Bruce A. Mungall, et al. 2006. “Potent Neutralization of Hendra and Nipah Viruses by Human Monoclonal Antibodies.” *Journal of Virology* 80 (2): 891–99.

Zhu, Zhongyu, and Dimiter S. Dimitrov. 2009. “Construction of a Large Naïve Human Phage-Displayed Fab Library through One-Step Cloning.” *Methods in Molecular*

Biology 525: 129–42, xv.

Zivanov, Jasenko, Takanori Nakane, Björn O. Forsberg, Dari Kimanius, Wim Jh Hagen, Erik Lindahl, and Sjors Hw Scheres. 2018. “New Tools for Automated High-Resolution Cryo-EM Structure Determination in RELION-3.” *eLife* 7 (November). https://doi.org/10.7554/eLife.42166.

Zivanov, Jasenko, Takanori Nakane, and Sjors H. W. Scheres. 2019. “A Bayesian Approach to Beam-Induced Motion Correction in Cryo-EM Single-Particle Analysis.” *IUCrJ* 6 (Pt 1): 5–17.

VITA

Ha Van Dang was born and raised in Hanoi - the capital city of Vietnam, a small coastal country in Southeast Asia. In 2012, she boarded an airplane for the first time in her life to start her four-year undergraduate education at Mount Holyoke College, South Hadley - a small town in Western Massachusetts, US. The 18-hour flight and the interminable customs line in Detroit were her very first memories of the US.

At Mount Holyoke College, Ha majored in Biochemistry and minored in Physics. In her sophomore year, she was awarded the RISE scholarship from the German Academic Exchange Service (DAAD) to study liposome fusion biophysics in the lab of Dr. Rumina Dimova at the Max Planck Institute for Colloids and Surfaces in Potsdam, Germany. Since the beginning of her junior year, under the guidance of Dr. Lila Gierasch at University of Massachusetts, Amherst, Ha carried out her thesis research work on the protein homeostasis network in the bacterium *Escherichia coli* and graduated *magna cum laude* in 2016 from Mount Holyoke College.

In June 2017, after completing three lab rotations, Ha joined the lab of Dr. David Veesler in the Department of Biochemistry at University of Washington, Seattle, where she pursued her PhD research on characterizing neutralizing antibodies and antibody cocktails targeting the Fusion glycoprotein of Henipaviruses. In addition, Ha also undertook collaboration projects on structural characterization of computationally designed antibody nanocages and of DNA-aptamers used as detection agents for SARS-CoV-2. During her 5th year at UW, she completed a 5-month internship at Biogen (Cambridge, MA) Biotherapeutic and Medicinal Sciences (BTMS) department.

In the future, Ha hopes to continue to use structural biology to develop antibodies and other therapeutic platforms to combat diseases.